SCALAR-SOURCE IDENTIFICATION AND OPTIMAL SENSOR PLACEMENT IN TURBULENT CHANNEL FLOW

by

Qi Wang

A dissertation submitted to The Johns Hopkins University

in conformity with the requirements for the degree of

Doctor of Philosophy

Baltimore, Maryland

August, 2020

Abstract

The spreading of a released pollutant in a turbulent environment has severe consequences. The ability to identify the unknown source location from remote sensor data is greatly obfuscated by turbulence. This work discusses effective scalar-source localization algorithms in a turbulent channel by exploiting adjoint and ensemble methods, and by utilizing the growing power of high-fidelity simulations.

To reconstruct the spatial distribution of the source, a cost functional is defined based on the difference between the true sensor observations and their model predictions. Forward-adjoint simulations provide the gradient of the cost functional to the source distribution, and the source estimation is iteratively updated. When a single sensor is directly downstream, the reconstruction is accurate in the cross-stream directions but elongated in streamwise direction. Using more sensors improves the performance demonstrably.

We therefore seek the optimal sensor placement that improves the prediction in streamwise direction, by minimizing the condition number of the Hessian matrix of the cost functional. An iterative approach is adopted that gradually adjusts the sensor(s) while tracking the principal subspace of the Hessian. For a single sensor, the optimal location is near the edge of the scalar plume. This placement distinguishes signals for adjacent sources much more than sensor directly downstream.

For fast identification of the source location and intensity, an eigen-ensemble-variational algorithm is formulated, which relies on the left and right singular vectors, or eigen-sources and eigen-measurements of the scalar impulse-response system. The

projection of the true source onto an eigen-source is proportional to the projection of the sensor signal onto the corresponding eigen-measurement. The unknown source is identified by minimizing its deviation from this proportionality. We demonstrate effective ways to use an ensemble of trial sources to estimate the pre-requisite eigen-sources and accurately predict the source location. Furthermore, the effect of sensor noise can be evaluated when Gaussian noise is added to the measurement.

All together, the developed algorithms provide effective strategies for reconstruction of unknown scalar sources and optimization of sensor networks. The resulting data provide an important benchmark for future research on olfactory search strategies in fully turbulent environments.

Acknowledgments

Firstly and most importantly, I want to give the biggest gratitude to my Ph.D advisor, Dr. Zaki. He has guided me through all the hard work including professional communication and presentations as well as developing a rigorous, scientific way of thinking. He has also been very supportive of my new ideas generated along the way. By our fruitful discussion we shared our individual knowledge together with excitement, which makes many parts of the work truly enjoyable.

Many thanks to Professor Hesegawa and Dr. Davide from the University of Tokyo. It was such a pleasure and privilege to spend time meeting and discussing with you in Japan. Many of the discussions were so inspiring that part of the fundamental ideology of the work was nurtured during the early time of my doctorate study.

Part of the work regarding optimal sensor placement is in collaboration with Dr. Vincent Mons. However, I thank Dr. Mons not only for the collaboration, but even more for his caring, lenient and responsible personality.

As a man with too many quirks, I owe my deepest thanks to my colleagues and friends, Jiho You, Jin Lee, Mengze Wang, Yifan Du, Yue Hao, Reza Jahanbakhshi, Amir Esteghamatian for all the patience and endurance. As a humble new graduate at a special time, your friendship and support will be carved into memory.

At last, I want to thank all my family members, and my girl friend Jiaqi Zhang, for all the spiritual support during my hardest times.

Table of Contents

List of Tables

List of Figures

Nomenclature

$[r_x, r_y, r_z]$ Size of the true source in different directions

$[s_I, s_x, s_y, s_z]$ Standard deviation of the predicted source parameters when subject to measurement noise

α^n, β^n Coefficients in conjugate gradient methods at iteration step n

$\bar{\epsilon}$ Normalized cost function.

$\bar{c}, \bar{c}^*$ Temporal mean of the forward and adjoint scalar field

$\boldsymbol{\phi}^{(i)}$ Ensemble members of the trial sources

$\boldsymbol{\Phi}_n$ Leading subspace of rank q of the Hessian matrix for sensor placement at iteration step n

$\boldsymbol{\phi}_{n,l}$ Eigen vectors in the subspace $\boldsymbol{\Phi}_n$

$\Delta x^+, \Delta y^+, \Delta z^+$ grid spacing in x, y and z directions in plus units

$\delta(\mathbf{x})$ spatial delta function

$\delta(t)$ temporal delta function

$\delta_{95}, \delta_{995}$ Distance between the edge of the plume and directly downstream of the source in the cross-flow plane. The plume edge is found when the mean scalar field drops to 95% and 99.5% of the maximum value in the cross-flow plane

ϵ_I Relative error in predicted condition number

$\epsilon_j(\mathbf{x}, t)$ The error between predicted measurement and the true measurement

γ, α normalization coefficient for the true source distribution

γ_i Eigenvalues estimated by the subspace of rank q

$\hat{\phi}$ Gradient of the cost function to the source term

$\kappa_I = \lambda_1/\lambda_I$ Estimated condition number of the Hessian matrix $\mathbf{H}$

λ_i Eigenvalues of the Hessian matrix $\mathbf{H}$

λ_R Length scale evaluated from the shifting-source correlation coefficient

$\langle , \cdot , \rangle$ inner product in space and time

$\mathbf{b}$ Vector of measurement noise

$\mathbf{\Lambda}$ Estimated Hessian matrix from the subspace of rank q

$\mathbf{\Omega}$ Trust region selected by limiting the magnitude of $\tilde{\epsilon}_I$

$\mathbf{A}$ The impulse-response matrix of the source-sensor system

$\mathbf{B}$ Covariance matrix of measurement noise

$\mathbf{E}$ Ensemble of the trial sources

$\mathbf{G}$ Covariance matrix of the predicted source parameters when subject to measurement noise

$\mathbf{G}_l$ Covariance matrix of the predicted source locations when subject to measurement noise

$\mathbf{H}$ Hessian matrix of the cost function

$\mathbf{K}$ The matrix coding the relation between perturbation in the source parameters and the measurement deviation

$\mathbf{L}, \mathbf{L}^*$ advection-diffusion operator and its adjoint

$\mathbf{O}$ Observation matrix containing different measurement sequences from an ensemble of sources

$\mathbf{U}$ Subspace containing the leading eigen-measurements

$\mathbf{u}(\mathbf{x}, t)$ Forward velocity field

$\mathbf{x}_j^m = [x_j^m, y_j^m, z_j^m]$ Location of the sensors

$\mathbf{x}^s = [x^s, y^s, z^s]$ Location of the true source

ν_l, ν The molecular diffusion in the scalar variance balance equations

$\mathcal{A}_l, \mathcal{A}$ The advection of the scalar variance by the mean velocity in the scalar variance balance equations

$\mathcal{C}$ The correlation matrix with each element being the time-averaged correlation of sensor measurements from different source locations

$\mathcal{D}_l, \mathcal{D}$ The turbulent dispersion term in the scalar variance balance equations

$\mathcal{E}_l, \mathcal{E}$ The advection of the scalar variance by the mean velocity in the scalar variance balance equations

$\mathcal{L}$ Integral length scale of the plume one the $y - z$ plane

$\mathcal{N}(x, \sigma)$ Gaussian distribution centered at x with standard deviation σ

$\mathcal{T}_h$ Length of historical time horizon

$\mathcal{U}_b$ Bulk-flow speed of the channel flow

ω_i Weighting of the sensor network.

$\phi(\mathbf{x}, t)$ The source term of the scalar transport equation, spatial distribution of the source

ϕ' perturbation of the source term

$\phi^*(\mathbf{x}, t)$ Source term of the adjoint advection-diffusion equation

$\phi_T(\mathbf{x}, t)$ spatial distribution of the true source

$\tilde{\epsilon}_I$ Relative error in predicted condition number estimated using the leading subspace

$c(\mathbf{x}, t), \mathbf{c}$ The scalar field and its vector representation

$c(\mathbf{x}^m, t; \mathbf{x}^s)$ Forward scalar field at $\mathbf{x}^m$ starting from a source at $\mathbf{x}^s$

c' perturbation of the forward field

$c^*(\mathbf{x}^s, t; \mathbf{x}^m)$ Adjoint scalar field at $\mathbf{x}^s$ starting from a source at $\mathbf{x}^m$

$c^\dagger = \mathbf{V}\mathbf{c}^*$ Sensitivity of the cost functional to the control vector $\boldsymbol{\phi}$

$c', c^{*\prime}$ perturbation of the forward and adjoint scalar field

$c'_{rms}, c^{*\prime}_{rms}$ root-mean-squares of the forward and adjoint scalar perturbation field

$D_j = x_j^m - x^s$ Separation between the sensor and the true source. When only one sensor is available, D is used

H Hamiltonian

h Channel half height

H' perturbation of the Hamiltonian

I The index to compute the condition number

J Cost function

J' perturbation of the cost function

$L_{x,y,z}$ Domain size of the channel in x, y and z directions

$M_j(t)$ Measurement sequence at the j-th sensor location

N, N_{iter}, N_{total} Number of iterations in the search algorithm

N_t Number of time steps in the measurement sequence

N_{ens} Number of ensemble members

nx, ny, nz Number of grid points in x, y and z directions

p Forward pressure field

$Pe = ReSc = RePr$ Péclet number

Pr Prantl number for thermal diffusion

q Size of the subspace

$R^m_{MM}(\Delta x^m, \Delta t; D)$ Shift-sensor correlation coefficient

$R^s_{MM}(\Delta x^s, \Delta t^m; D)$ Shift-source correlation coefficient

$R_{cc}^{\langle yz \rangle}$ Correlation coefficient between the reconstructed and the true scalar field as a function of x, averaged in y and z directions

$R_{\phi\phi}^{x,y,z}$ Correlation coefficient between the reconstructed and the true source in x, y and z directions

r_i distance of the optimal sensor from the channel center. The optimal sensor is found by minimizing the condition number κ_i

$R_{\phi\phi}$ Correlation coefficient between the reconstructed and the true source

$R_{cM}(\Delta y, \Delta z)$ Correlation coefficient between the scalar signal at the sensor and other sensor locations

$R_{u'u'}(\Delta x, \Delta t)$ The correlation coefficients of the streamwise velocity perturbation

Re Reynolds number

s_0 Standard deviation of the relative measurement noise

Sc Schmidt number for scalar diffusion

T Length of the time horizon for data assimilation

$t, \tau = t^* = T - t$ Forward and backward time

t^m measurement time

$U_t(y), U_t^+(y)$ Transport velocity of the scalar field, normalized by outer and inner scales

$u_\tau = \sqrt{\nu \frac{\partial U}{\partial y}\big|_{y=0}}$ friction velocity

$V_{(i,j,k)}, \mathbf{V}$ Cell volume for the computational cell (i,j,k), and the diagonal matrix with all cell volumes

x_B, x_E Beginning and ending x location of the search domain

x^s_{opt}, I^s_{opt} Optimal location and intensity of the source

$y^+ = y\nu/u_\tau$ Wall normal distance in plus units

Chapter 1

Introduction

1.1 Olfactory search in turbulent environments

From the lethal release of cyanide, heavy metals and acid into the Alamosa River to air pollution that has contributed to more than 3.2 million deaths globally per year [1, 2], detrimental events of natural or artificial contaminations have required our preparedness when faced with short-term as well as long-term pollution release in the environment. Being able to identify the source of pollution and its strength with a certain level of accuracy is more than important for evaluation and mitigation of its impact. However, in most natural scenarios, the effect of fluid turbulence enhances the mixing and spreading of pollutant far away from the source. Therefore, utilizing remote sensors to give information and trace back to the source location becomes a challenging, most of times ill-posed inverse problem. Popular methods to solve such inverse problems problems include probabilistic frameworks exploiting Bayes' Theorem [3, 4], variational techniques [5–8] and ensemble-based variational methods [9–11].

In current study, our primary goal is the spatial information of a passive scalar source, as written in chapter 2. The investigation of optimal sensor placement would be in chapter 3. A quick and effective ensemble algorithm that directly determines the source location and intensity is presented in chapter 4, together with an uncertainty quantification that reveals the fundamental difficulty of source localization using re-

mote sensor signals.

1.2 Passive scalar pollution search algorithm

Olfactory search in turbulent environment aims at obtaining the spatial or temporal information of the source of a pollution release from remote measurement. In applications where the source location is known, for example the Deep Water Horizon Oil Spill [12], estimating the time history of the oil leak's flow rate is of vital importance to assess the impact of the disaster and prepare accordingly. In other applications, we have full knowledge of the temporal signature of the source and aim at reconstructing the spatial information. Traditional efforts to estimate the scalar source can be summarized into different categories: forward, backward and probability methods [13]. While the forward methods rely on a trial-and-error process using forward solver only [14–18], the backward methods aim to, and struggle to solve the advection-diffusion equation backwards in time efficiently with an extra stabilizing term [19, 20]. Probability methods are developed to exploit the Bayes' Theorem [21–23]. With the availability of high-fidelity simulation, variational approaches utilizing both the forward and adjoint solutions of the scalar transport equation become a promising option. Huang *et al.* [24] used adjoint optimization to reconstruct the spatial distribution as well as the time-varying intensity of a scalar source in a steady ground water environment. Cerizza *et al.* [5] reconstructed the temporal signal of a source release at a known location in a turbulent channel flow by the method of steepest descent. In currently study, our primary focus in chapters 2 and 3 is to develop, implement and evaluate adjoint variational methods for identifying the source distribution as a function of space for a temporally steady pollution release in a canonical turbulent channel flow with $Re_\tau = 180$.

1.3 Optimal sensor placement

The next question is the optimal sensor placement that enhances the performance of data assimilation. The formulation of optimal sensors varies depending on the method to solve the inverse problem. In terms of velocity state reconstruction, optimal sensor placement is normally chosen to be the local maxima of the leading modes from proper orthogonal decomposition (POD) [25–27]. In terms of flow control, where Karman filter is widely used, the linear feedback laws, especially the spatial ditribution of functional gains indicates the sensor locations [28].

For adjoint-variational approach, the ability to effectively invert the system depends on the adjoint sensitivity of the sensor measurements to the unknown state we want to assimilate. The sensitivity can either be first-order or second-order. Equivalently, either the gradient or the Hessian can provide information regarding the optimal sensor placement. Mons *et al.* [29] proposed an iterative algorithm to maximize the first-order sensitivity of the sensor with respect to a change in the initial and boundary conditions. In some applications, the second-order sensitivity is a better choice. This is typically true for an ill-posed problem with a large dimension of unknowns. The level of ill-posedness can be represented by the eigenvalue spectrum of the Hessian matrix. By the attempt to “equalize" different eigenvalues, the condition of the system can be improved. Mathematically, this is the same as minimizing the condition number of the system. Kang & Xu [30], for example, has done similar work to maximize the observability of the system, which is equivalent to maximizing the smallest eigenvalue of the Gramian matrix.

1.4 Uncertainty quantification

The propagation of uncertainty in large-scale applications in computational fluid dynamics (CFD) has been a very active field. Quantification of such propagation is

one of the main challenges and goals for real application. Probabilistic uncertainty quantification has been widely used to propagate noisy inputs to the distribution of outputs and has witnessed massive developments within the past several decades [31]. For data assimilation applications, uncertainty quantification is even more closely related. For example, Kalman filter methods, or the linear quadratic estimation (LQE) have always taken the covariance matrix of the observations into account to enhance fidelity of state estimation [32, 33]. In reality, observations in real, turbulent flows will inevitably be influenced by noise. A system with diffusion is difficulty to invert because a small noise in the ending state, or the output will be amplified and influence our estimate of the initial state, or the input. Therefore, for diffusive systems, the difficulty of inferring the initial state can be quantified by the ratio between the error in the reconstruction of input and that of the observation. However, such work has never been done in turbulent environment regarding scalar source reconstruction, which is of wide interest in environmental fluid mechanics and climate control. [4] focused on finding passive scalar source parameters in ground water system. Their study took into account Gaussian noise in the measurement. The impulse-response matrix was built to facilitate Monte Carlo simulation. The probability distribution function (PDF) of the predicted source parameter can then be constructed. Cerizza *et al.* [5] examined the effect of Gaussian noise in the measurement data by comparing the reconstruction results using the measurement data with and without noise. In this case performing multiple numerical experiment with different samples of measurement noise is too costly and the effect was shown qualitatively.

While uncertainty quantification is difficult in large-dimensional problems, we focus on a simple application of determining the location and intensity of passive scalar sources from remote measurement. A thorough investigation will be presented in chapter 4, where the amplification from measurement noise to errors in the predicted source location and intensity will be quantified for various scenarios.

1.5 Objectives

The main objective of this thesis is to assess the power and some fundamental limitation of data assimilation in turbulent environments. We mainly explored the adjoint-variational approach by either performing data assimilation and addressing the phyiscal interpretation of the adjoint sensitivity or optimizing Hessian matrix. The main problem setup considered here is in a canonical turbulent channel flow: the spatial reconstruction of a passive scalar source based on remote sensor measurements. To obtain perfect forward-adjoint relation satisfied to machine-zero, a discrete-then-transpose approach was used to derive the discrete adjoint, with details provided in appendix A.1. The rest of this thesis is organized in the following manner. In chapter §2 the adjoint-variational method will be adopted to perform scalar source reconstruction, with full evaluation of different sensor and source locations. The reconstruction quality is assessed and explained with flow statistics. In chapter §3 we address the follow-up question of optimal sensor placement by optimizing the spectrum of the Hessian matrix. The opimization is done with a subspace-tracking algorithm, which also involves both forward and adjoint simulations. Different sensor placements will be compared and the difference in performance will be explained. In chapter §4 we fully utilize the benefit of the linear system and evaluate the fundamental difficulty of locating the source parameterized by its location and intensity, through a limited number of forward simulations. Uncertainty quantification is done by assuming the measurements are subject to noise with a Gaussian distribution.

Chapter 2

Spatial Reconstruction of a steady scalar source in turbulent channel flow

2.1 Introduction

2.1.1 Background

Scalar sources from natural disasters and human activities can pose threats to the environment and public safety. Estimating the source distribution of such contaminants using remote sensors is crucial for management and remediation. Scalar diffusion, however, renders the prediction of the source location non-unique. In addition, in most natural scenarios, the flow is turbulent and eddies disperse the scalar, which further hinders the ability to infer the source location from remote measurements. Direct numerical simulations (DNS) can accurately capture the details of scalar transport, for given scalar sources and flow conditions, and the resulting data and knowledge provide the foundation for future reduced-order engineering models. In contrast to such forward analyses, the inverse estimation of unknown scalar sources from limited measurements is a more difficult task due to its inherent ill-posed nature. In the present work, an adjoint-based algorithm is developed that relies on high-fidelity simulations in order to reconstruct a scalar source from remote measurements in turbulent channel flow, and key factors that affect the quality of the reconstruction are

examined.

2.1.2 Scalar-source identification

Source-identification techniques were classified by Liu & Zhai [13] into three categories: forward, backward and probability methods. Forward methods apply a simple "trial-and-error" approach. Forward simulations are performed with assumed source parameters, which can be adjusted by the deviation between the simulated outcome and true measurements. Backward methods simulate with stabilizing treatments backward in time from the end state to identify the source information. Probability methods estimate the probability density function (PDF) of the source parameters or maximize a probability objective function. We further include adjoint techniques as a fourth category of inverse modelling for source identification.

In the context of forward methods, Gorelick *et al.* [14] formulated the source-identification problem in a two-dimensional steady groundwater system using a linear optimization framework. They performed separate forward simulations for impulses at different potential source locations and formed the unit impulse-response matrix, or "concentration response matrix", with each row corresponding to the measurements from one source. Linear programming and multiple regression were then used to determine the spatial source distribution. In one dimensional uniform steady flow, the impulse-response matrix can be formed using the analytical solution. The source parameters can then be determined using nonlinear least squares method with Newton-Raphson algorithm [15] or Tikhonov regularization [34]. Mahar & Datta [16] developed a forward method based on optimization of a normalized cost functional to identify source location and flux in a two-dimensional groundwater monitoring network. In their later works [17, 18], the method was used to determine the aquifer parameters together with source identification. These approaches are not, however, feasible for turbulent conditions and large search domains.

Backward methods aim to reconstruct the scalar with one simulation performed with negative time stepping. However, negative diffusivity leads to instability and stabilizing treatments are required. Skaggs & Kabala [19] proposed a quasi-reversible (QR) operator, $\frac{\partial}{\partial t} - \nabla^2 - \epsilon\nabla^4$, where the higher-order diffusion term is introduced to stabilize the solution and ϵ is a small parameter which is difficult to determine and not possible to generalize. Atmadja & Bagtzoglou [20] studied the backward beam equation (BBE) to recover the pollution evolution history in two-dimensional groundwater. Backward methods are efficient because they require only one backward simulation. However, it is generally difficult to stabilize the procedure.

Probability methods focus on the PDF of the source characteristics. They can easily take measurement error and systematic uncertainty into account. Woodbury and coworkers introduced the Minimum Relative Entropy (MRE) method to reconstruct the history of release from a source in three-dimensional steady uniform flow [21–23]. The prior PDF of the history of release is updated based on measurement data and the corresponding confidence level can be directly computed. Other efforts that focused on the use of moving sensors to approach the source location in turbulent environments also utilized entropy optimization [35–37]. Instead of following the direction of the concentration gradient, “infotaxis" approach aims to maximize information gain for every movement, by minimizing the entropy of the PDF of the source location. Note that the turbulent velocity field was not directly used in those search algorithms, but its effect was modeled by an eddy diffusivity.

2.1.3 Adjoint approach

While the scalar transport equation can predict the forward evolution of the scalar field, its adjoint can be leveraged to trace back from the sensor signal to potential source locations. Similar to the backward methods, adjoint equations are evolved backward in time, but their positive diffusion coefficient renders them numerically

more stable. Most importantly, the spatio-temporal distribution of the adjoint field has a clear interpretation as the sensor sensitivity [4].

The adjoint approach for scalar-source reconstruction has previously been adopted in conjunction with Reynolds Averaged Navier-Stokes (RANS) simulations and other reduced models. For example, it was adopted in the localization of the source of an atmospheric fugitive release [38–40]; And Houweling *et al.* [41] used “off-line" 3-D Atmospheric Transport Model 2 and its adjoint for evaluation of the sources and sink of atmospheric methane.

Using fully resolved turbulent flow data, Cerizza *et al.* [5] developed an adjoint-variational algorithm to recover the time-history of scalar release from a source at a known location in turbulent channel flow ($Re_\tau = 150, Sc = 1$). That setup is relevant, for example, when sensors can not be placed directly at the known source location due to environmental hazards. In contrast, the present work is concerned with configurations where the source is steady and its location is unknown. The distinction between Cerizza's and the present work has an important implication: When only the time-history of the source is sought, the scalar field is a linear function of the control vector in successive iterations, i.e. rescaling the amplitude of the source simply rescales the scalar field. This property is not preserved if the estimated source changes position in successive iterations.

Adjoint methods can also be applied in a probability framework. Starting from the forward-adjoint duality relation, Neupauer & Wilson [42] developed an adjoint-probability approach to determine the groundwater pollution location and travel time probabilities. The solution of the adjoint equation with an impulse source term at the sensing location was interpreted as a probability distribution. Despite the small computational cost, the adjoint-probability method needs the source turn-on time to estimate the location probability. Pudykiewicz [43] adopted this framework and solved the adjoint equations in a global range to identify the source of atmospheric

pollution. As noted by Keats *et al.* [4], however, the adjoint scalar field should be interpretted as the sensor sensitivity rather than the source location PDF.

The forward-adjoint duality relation can also be exploited to construct the impulse-response matrix as proposed by Keats *et al.* [4] to estimate the posterior distribution of pollution source parameters using Markov Chain Monte Carlo (MCMC) method. They constructed the impulse-response matrix with numerous adjoint simulations. The total number of simulations required is the product of the number of sensors and the number of time intervals sampled at those sensors, which makes it feasible only for steady flow, where different time intervals lead to the same result. For turbulent flows, iterative methods with forward and adjoint simulations are normally more feasible than constructing the response matrix directly.

The objective of the current study is to develop an algorithm that utilizes eddy-resolving simulations in order to interpret remote scalar measurements and identify the location of the source. We assume that the source is steady in order to focus on its spatial reconstruction; the temporal problem has been thoroughly investigated by Cerizza *et al.* [5]. We formulate the problem as a minimization of a cost functional using forward-adjoint iteration. The algorithm is applied in the canonical configuration of turbulent channel flow. Different elevations of the source from the walls are considered, as well as different sensor-source separations. Performance is also assessed for isolated and networks of sensors. The results are explained using the spatio-temporal correlations of the forward scalar fields and statistics of the adjoint scalar field which represents the sensor sensitivity.

The flow configuration and governing equations are described in §2.2, and the adjoint algorithm for the source reconstruction is derived in §2.2.2. Statistics of the forward and adjoint scalar fields are reported in §2.3. The source reconstructions using single and multiple-sensor arrangements are reported in §§2.4 and 2.5, respectively, and results are interpreted in terms of relevant physical processes. Conclusions are

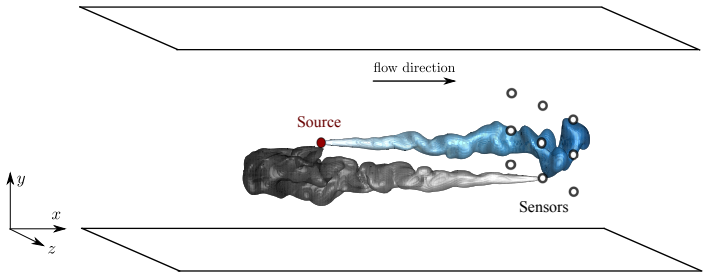

Figure 2-1. Schematic of the forward and adjoint scalar fields in the rectangular computational domain. Filled and open circles represent the scalar source and sensor group, respectively. The forward field is the instantaneous domain of influence of the source, while the adjoint field is the instantaneous domain of dependence of a sensor.

presented in §2.6.

2.2 Problem Setup and governing equations

The present study is performed in a turbulent channel flow, where an isolated or a network of sensors are placed downstream of an unknown scalar source and the measurements are used to identify the source location. A schematic of the problem configuration is shown in figure 2-1. For the velocity fields, the computational domain is periodic in the both the streamwise (x) and spanwise (z) directions, and no-slip conditions are imposed in the wall-normal (y) direction at the bottom and top walls.

2.2.1 Forward velocity and scalar equations

The velocity field satisfies the incompressible Navier-Stokes equations,

$$\frac{\partial \mathbf{u}}{\partial t} + \mathbf{u}\cdot\nabla\mathbf{u} = -\nabla p + \frac{1}{Re}\nabla^2\mathbf{u}, \qquad \nabla\cdot\mathbf{u} = 0. \tag{2.1}$$

In the above expression, lengths and velocities are scaled by the channel half height, h, and the bulk-flow speed, U_b. The equations were solved using a fractional step algorithm with a volume-flux formulation [44]. The diffusion operator is treated implicitly in time with Crank-Nicolson scheme while the nonlinear advection terms are treated explicitly using Adams-Bashforth. The elliptic pressure equation is solved using Fourier transform in the periodic streamwise and spanwise directions, and a

Domain size			Grid points			Grid resolution			
L_x/h	L_y/h	L_z/h	nx	ny	nz	Δx^+	Δz^+	Δy^+_{max}	Δy^+_{min}
4π	2	2π	384	256	320	5.89	3.53	2.95	0.20

Table 2-I. Domain size and grid resolution.

tridiagonal inversion in the wall-normal coordinate. The algorithm has been adopted for a number of direct numerical simulations of transitional [45, 46] and turbulent flows [47, 48].

A constant mass-flow rate is imposed. The corresponding mean friction Reynolds number is $Re_\tau \equiv u_\tau h/\nu = 180$, where u_τ is the friction velocity, h is the channel half height and ν is the fluid kinematic viscosity. The size of the computational domain is $(L_x, L_y, L_z) = (4\pi h, 2h, 2\pi h)$ in the streamwise (x), wall-normal (y) and spanwise (z) directions, where h is the channel half-height. These values are equal to those adopted by Kim *et al.* [49] who used a pseudo-spectral algorithm, and also by Jelly *et al.* [50] who used the same Navier-Stokes solver and performed extensive validation. We have therefore adopted a similar grid resolution to the latter study, with uniform Cartesian mesh in both the streamwise and spanwise directions and hyperbolic stretching in the wall-normal coordinate (see table 2-I). The velocity fields were stored at full spatial resolution and at a temporal resolution of $\Delta t = 0.01$ (or $\Delta t^+ = 0.116$) during a period $T = 40h/U_b$ (or $T^+ = 462.86$); these field are needed for the solution of the forward and adjoint scalar equations.

Throughout this work, the concentration c is assumed to be a passive scalar, and is therefore governed by the advection-diffusion equation,

$$\underbrace{\left(\frac{\partial}{\partial t} + \mathbf{u}\cdot\nabla - \frac{1}{Pe}\nabla^2\right)}_{\mathbf{L}} c = \phi(\mathbf{x}, t), \tag{2.2}$$

where the Péclet number is $Pe \equiv Re\,Sc$ and the Schmidt number was set to $Sc = 0.7$ which is relevant to gas diffusion in air $(Sc \sim O(1))$. In the case of a thermal source, the definition of the Péclet number is $Pe \equiv Re\,Pr$, where Pr is the Prandtl number

($Pr \approx 0.7$ for air). With information of the velocity fields available, the scalar transport equation decouples from Navier-Stokes equations. Periodic boundary conditions are enforced in the span; homogeneous Neumann boundary conditions $\partial c/\partial y = 0$ are imposed at both walls, which physically corresponds to zero scalar flux across the top and bottom surfaces. Note that none of the forward or adjoint scalar plumes spread sufficiently to occupy the full spanwise extent of the domain. At the inlet of the channel we impose $c = 0$, while at the outflow $\frac{\partial c}{\partial t} + U_b \frac{\partial c}{\partial x} = 0$. The discretization adopted a flux formulation, similar to that of the flow equations, with Adams-Bashforth and Crank-Nicolson adopted for the temporal discretization of the advection and diffusion terms; the source term (ϕ) was treated explicitly.

In order to generate sensor signals, scalar sources were placed at $(x^s, z^s) = (2, \pi)$, and at four different wall-normal heights within the channel, $y^+ = \{180, 40, 15, 5\}$. These heights correspond to the channel centre, and locations within the log layer, the buffer layer and the viscous sublayer. The true source, $\phi(\mathbf{x}, t) = \phi_T(\mathbf{x})$, is assumed to be steady with spatial distribution set to be a cut-off cosine function,

$$\phi_T(\mathbf{x}) = \gamma \left[\cos(r\pi) + 1\right] \left[\text{sign}(1 - r) + 1\right], \tag{2.3}$$

$$\gamma = \frac{3}{2\left(\pi - 6/\pi\right) r_x r_y r_z}, \qquad r = \sqrt{\left(\frac{x - x^s}{r_x}\right)^2 + \left(\frac{y - y^s}{r_y}\right)^2 + \left(\frac{z - z^s}{r_z}\right)^2}, \tag{2.4}$$

where $\mathbf{x}^s \equiv (x^s, y^s, z^s)$ is the location of the centre of the source, and $(r_x.r_y, r_z)$ are the radii of the source in different directions. This form is a well-resolved kernel that represents a concentrated source which vanishes outside a short range. Due to the presence of the wall, the size of the source was adjusted such that $r_y = 3\Delta y$, while $r_x = r_z = 0.1$. Irrespective of the size of the source, the definition of γ ensures that the volume integral of ϕ_T is unity, which is also ensured numerically. Measurements were performed by placing sensors downstream of the sources at $\mathbf{x}_j^m$, where the subscript identifies the j^{th} sensor. The streamwise source-sensor separation is denoted $D_j \equiv$

$x_j^m - x^s$, and the measurement time-series is denoted $M_j(t) = c\left(x_j^m, t\right)$.

In the present study, when a single sensor is considered, focus is placed on its performance when aligned downstream of the source. In reality, the source location is unknown and, therefore, selecting the relative position of the sensor is not possible. However, the present study is intended to assess the feasibility and performance of the algorithm. We will also consider the case of multiple sensors (§2.5), which is more akin to practical applications.

2.2.2 Adjoint scalar equations and the search algorithm

The adjoint scalar field c^* will be used to formulate a search algorithm that identifies the unknown scalar source from remote measurements. For generality, the derivations are presented using the continuous adjoint variables, i.e. the adjoint of the continuous forward equations. The implementation, however, uses the discrete adjoint, or the adjoint of the discrete forward equations, in order to ensure that the duality relation is satisfied to machine precision. Details of the discrete form are provided to Appendix A.1. It is worth noticing that for the numerical scheme we adopted here to discretize the forward problem, if the forward-adjoint relation were not perfectly satisfied, the conjugate gradient method would result in negative step sizes. As a result, the cost function cannot be further reduced after several iterations.

The adjoint scalar equation is derived starting from the identity,

$$\langle \mathbf{L}c, c^* \rangle = \langle c, \mathbf{L}^* c^* \rangle, \tag{2.5}$$

where $*$ denotes the adjoint, and $\langle f, g \rangle \equiv \int_0^T \int_V f g dV dt$. Using integration by parts and eliminating the concomitant terms, we obtain,

$$\mathbf{L}^* = \frac{\partial}{\partial t^*} - \mathbf{u} \cdot \nabla - \frac{1}{Pe}\nabla^2, \qquad t^* = T - t. \tag{2.6}$$

Note that the velocity field and time are reversed in the adjoint equation,

$$\left(\frac{\partial}{\partial t^*} - \mathbf{u} \cdot \nabla - \frac{1}{Pe}\nabla^2\right) c^* = \phi^*(\mathbf{x}, t), \tag{2.7}$$

The boundary conditions are periodicity in the spanwise z-direction, $c^* = 0$ at the inlet and outlet of the channel, and zero adjoint scalar flux $\partial c^*/\partial y = 0$ on both walls.

The duality relation between the forward and adjoint fields provides a physical interpretation of the latter [4]: Consider the forward scalar field due to a source term $\phi = \delta(\mathbf{x}-\mathbf{x}^s)\delta(t-t^s)$ and the adjoint field due to a source term $\phi^* = \delta(\mathbf{x}-\mathbf{x}^m)\delta(t-t^m)$; the two can be related according to,

$$\begin{aligned} c^*(\mathbf{x}^s, t^s) &= \langle \delta(\mathbf{x}-\mathbf{x}^s)\delta(t-t^s), c^* \rangle \\ &= \langle \mathbf{L}c, c^* \rangle = \langle c, \mathbf{L}^* c^* \rangle = \langle c, \delta(\mathbf{x}-\mathbf{x}^m)\delta(t-t^m) \rangle = c(\mathbf{x}^m, t^m). \end{aligned} \tag{2.8}$$

The expression demonstrates that the sensor measurements at $(\mathbf{x}^m, t^m)$ due to a scalar impulse at $(\mathbf{x}^s, t^s)$ are identical to the adjoint signal at $(\mathbf{x}^s, t^s)$ due to an adjoint impulse at $(\mathbf{x}^m, t^m)$. In the context of the search algorithm, should a sensor at $\mathbf{x}^m$ receive a signal at t^m, the scalar source must be within the region where the adjoint field at t^s is finite. Conversely, absent a signal at the sensor at t^m, any sources must be outside the instantaneous adjoint plume at t^s. We will refer to the region where the forward field is appreciable in magnitude as the domain of influence of the source; and the region where the adjoint field has a finite value as the domain of dependence of the sensor. Figure 2-1 shows a schematic for these two regions in a cases of steady forward and adjoint sources. Similar duality relations between certain forward and adjoint scalar statistics can be derived, and will be introduced as the associated terms are evaluated.

The search algorithm for a steady scalar source $\phi_T(\mathbf{x})$ is herein formulated as a constrained optimization. Assuming we have an estimate $\phi(\mathbf{x})$ of the source, we can compare its associated scalar fields at the locations of all sensors with the true measurements. When the estimated and measured signals are identical, we have confidence in our estimate of the source distribution.

In this formulation, the cost functional is defined in terms of the difference between the estimated measurements $c(\mathbf{x}_j^m, t)$ and the true signals $M_j(t)$, where j is the sensor

identifier. The difference is squared, integrated over the time horizon $[0, T]$ and summed for all sensors,

$$J = \frac{1}{2} \sum_j \int_0^T \left(c(\mathbf{x}_j^m, t) - M_j(t) \right)^2 dt. \tag{2.9}$$

The constraint is that the scalar field from any estimated source satisfies the advection-diffusion equation (2.2). We can therefore define the Hamiltonian,

$$\begin{aligned} H =& J - \int_0^T \int_V \left(\frac{\partial c}{\partial t} + \mathbf{u} \cdot \nabla c - \frac{1}{Pe} \nabla^2 c - \phi(\mathbf{x}) \right) c^* \, dt dV \\ =& J - \langle \mathbf{L}c - \phi(\mathbf{x}), c^* \rangle . \\ =& J - \langle c, \mathbf{L}^* c^* \rangle + \langle \phi(\mathbf{x}),\, c^* \rangle, \end{aligned} \tag{2.10}$$

where the last equality is obtained using the Lagrangian identity. The variation of the Hamiltonian (2.10) is,

$$H' = J' - \langle c', \mathbf{L}^* c^* \rangle + \langle \phi'(\mathbf{x}),\, c^* \rangle, \tag{2.11}$$

$$\begin{aligned} J' &= \sum_j \int_0^T c'(\mathbf{x}_j^m, t) \left(c(\mathbf{x}_j^m, t) - M_j(t) \right) dt \\ &= \langle c',\, \sum_j \epsilon_j(t) \delta(\mathbf{x} - \mathbf{x}_j^m) \rangle, \end{aligned} \tag{2.12}$$

where prime denotes a change in the variable and $\epsilon_j(t) \equiv c(\mathbf{x}_j^m, t) - M_j(t)$ is the error between the estimated and true measurements at sensor j.

Introducing (2.12) in (2.11) and grouping terms, we obtain

$$H' = -\langle c',\, \underbrace{\mathbf{L}^* c^* - \sum_j \epsilon_j(t) \delta(\mathbf{x} - \mathbf{x}_j^m)}_{\equiv 0,\, \text{adjoint equation}} \rangle + \langle \phi'(\mathbf{x}),\, c^* \rangle. \tag{2.13}$$

where $\epsilon_j(t)$ acts as the source term in the adjoint equation, $\mathbf{L}^* c^* = \sum_j \epsilon_j(t) \delta(\mathbf{x} - \mathbf{x}_j^m)$. With the definition of the adjoint equation, the variation of the Hamiltonian reduces to,

$$H' = \langle \phi'(\mathbf{x}),\, c^* \rangle = \int_V \phi'(\mathbf{x}) \int_0^T c^*(\mathbf{x}, t) dt \, dV. \tag{2.14}$$

In the discrete form, the above expression becomes,

$$H' = \boldsymbol{\phi}'^T \, \mathbf{V} \int_0^T \mathbf{c}^*(t) dt = \sum_{i,j,k} \phi'_{(i,j,k)} \, V_{(i,j,k)} \int_0^T c^*_{(i,j,k)}(t) dt, \tag{2.15}$$

where $\boldsymbol{\phi}$' is the control column vector, $\mathbf{V}$ is a diagonal matrix with the volume of the computational cells (i,j,k) as its elements, and $\mathbf{c}^*$ is a column vector of the adjoint field. Therefore the gradient of the Hamiltonian, $\hat{\phi}$, can be evaluated as,

$$\hat{\phi}_{(i,j,k)} = \frac{\partial H}{\partial \phi_{(i,j,k)}} = \int_0^T \underbrace{V_{(i,j,k)} c^*_{(i,j,k)}}_{\equiv \mathbf{c}^\dagger_{(i,j,k)}} dt = \int_0^T \mathbf{c}^\dagger(\mathbf{x},t)dt, \tag{2.16}$$

where $\mathbf{c}^\dagger \equiv \mathbf{V}\mathbf{c}^*$ is the sensitivity of the cost functional to the control vector $\boldsymbol{\phi}$. In order to minimize the Hamiltonian using the method of steepest descent, $\boldsymbol{\phi}$' can be given by

$$\boldsymbol{\phi}' = -\alpha \hat{\boldsymbol{\phi}}(\mathbf{x}) = -\alpha \int_0^T \mathbf{c}^\dagger(\mathbf{x},t)dt. \tag{2.17}$$

where α is a positive step size, and its optimal value can be evaluated [5]. In the present work, we adopt conjugate gradient method because it is better suited for ill-conditioned systems [24]. The update of the estimated source from iteration (n) to $(n+1)$ is therefore given by,

$$\boldsymbol{\phi}^{n+1}(\mathbf{x}) = \boldsymbol{\phi}^n(\mathbf{x}) - \alpha^n \tilde{\boldsymbol{\phi}}^n(\mathbf{x}), \qquad \tilde{\boldsymbol{\phi}}^{n+1} = \beta^n \tilde{\boldsymbol{\phi}}^n + \hat{\boldsymbol{\phi}}^{n+1}. \tag{2.18}$$

The new search direction $\tilde{\boldsymbol{\phi}}^{n+1}$ is updated as a conjugation of the new gradient direction $\hat{\boldsymbol{\phi}}^{n+1}$ and the old one $\tilde{\boldsymbol{\phi}}^n$ (in the first iteration, $\tilde{\boldsymbol{\phi}}^{n=1} = \hat{\boldsymbol{\phi}}^{n=1}$). The coefficients are derived from the Fletcher-Reeves formula [51],

$$\alpha^n = \frac{\|\hat{\boldsymbol{\phi}}^n\|^2}{\sum_j \int_0^T \left(\hat{\mathbf{c}}^n\left(\mathbf{x}_j^m, t\right)\right)^2 dt}, \qquad \beta^n = \frac{\|\hat{\boldsymbol{\phi}}^{n+1}\|^2}{\|\hat{\boldsymbol{\phi}}^n\|^2}, \tag{2.19}$$

where $\mathbf{L}\hat{\mathbf{c}}^n = \hat{\boldsymbol{\phi}}^n(\mathbf{x})$. The coefficient β^n ensures that each new search direction $\tilde{\boldsymbol{\phi}}^{n+1}$ is conjugate to earlier ones.

The procedure is summarized in algorithm 1. An auxiliary variable $\tilde{\mathbf{c}}$ is introduced for convenience, and is simply the scalar field due to the $\tilde{\boldsymbol{\phi}}$ search direction, or $\mathbf{L}\tilde{\mathbf{c}}^n = \tilde{\boldsymbol{\phi}}^n$. In order to ensure that the algorithm is convergent, and that its performance is independent of the implementation, it is essential to accurately satisfy the forward-adjoint duality relation (2.5). For this reason, the discrete adjoint technique was

Algorithm 1: Adjoint-variational algorithm for scalar-source reconstruction from remote measurements.

- $n = 0$;
- Prescribe an initial guess of the source distribution, $\boldsymbol{\phi}^0 = \mathbf{0}$;
- Advance the forward equations $\mathbf{L}\mathbf{c}^0 = \boldsymbol{\phi}^0$ and evaluate the deviation between estimated and true measurements $\epsilon_j^0 = c^0(\mathbf{x}_j^m, t) - M_j(t)$;
- Advance the adjoint equation, $\mathbf{L}^* c^* = \sum_j \epsilon_j^0(t)\delta(\mathbf{x} - \mathbf{x}_j^m)$, and use (2.17) to evaluate the initial gradient direction, $\hat{\boldsymbol{\phi}}^0 = \int_0^T \mathbf{c}^\dagger(\mathbf{x}, t)dt$;
- At the initial step, $\tilde{\boldsymbol{\phi}}^0 = \hat{\boldsymbol{\phi}}^0$;

while *Convergence condition is not satisfied* **do**

- Advance the forward equation $\mathbf{L}\tilde{c}^n = \tilde{\phi}^n$;
- Compute α^n from equation (2.19) and update the source $\boldsymbol{\phi}^{n+1} = \boldsymbol{\phi}^n - \alpha^n \tilde{\boldsymbol{\phi}}^n$;
- Update the corresponding $\epsilon_j^{n+1} = \epsilon_j^n - \alpha^n \tilde{\mathbf{c}}^n(\mathbf{x}_j^m, t)$;
- Solve adjoint equation, $\mathbf{L}^* c^* = \sum_j \epsilon_j(t)\delta(\mathbf{x} - \mathbf{x}_j^m)$, and use (2.17) to evaluate the gradient direction, $\hat{\boldsymbol{\phi}}^{n+1} = \int_0^T \mathbf{c}^\dagger dt$;
- Compute β^n from equation (2.19) and update the search direction $\tilde{\boldsymbol{\phi}}^{n+1} = \beta^n \tilde{\boldsymbol{\phi}}^n + \hat{\boldsymbol{\phi}}^{n+1}$;
- $n = n + 1$;

end

adopted, which computes the adjoint of the discretized forward equations and satisfies (2.5) to machine precision. Details of the discrete adjoint and validation of the forward-adjoint relation are provided in appendix A.1.

Flow variables will be decomposed into mean and fluctuation quantities, $\mathbf{u} = \langle \mathbf{u} \rangle + \mathbf{u}'$, where the mean is obtained by averaging in the homogeneous streamwise and spanwise directions and in time. The forward and adjoint scalar fields can similarly be decomposed into a mean and fluctuation, $c = \overline{c} + c'$ and $c^* = \overline{c^*} + c^{*\prime}$. The mean is marked by an overline, and is computed by averaging in time and over an ensemble of independent simulations with sources at different spanwise and streamwise locations.

2.3 Characteristics of the forward and adjoint scalar fields

It is instructive to examine characteristics of the scalar field and its adjoint in the present flow configuration, because together they underlie the performance of the search algorithm. For example, the time-averaged adjoint scalar field represents the mean sensitivity of a sensor; a scalar source in the higher sensitivity region will be reconstructed more accurately. Meanwhile, the root-mean-square (RMS) of the adjoint scalar field represents the temporal variation of the sensor sensitivity to a scalar source at that location—smaller values are therefore desirable when the time dependence of the source is of interest [e.g. 5].

Simple statistics of the forward and adjoint scalar fields are examined in this section and are, when possible, related to one another analytically; additional statistical quantities will be introduced in subsequent sections to aid the discussion. The sources of release for the evaluation of statistics of c and c^* are assumed to be steady, and the four wall-normal locations of interest are contrasted. Statistics of the forward field were integrated over 700 convective time units for a single plume due to a steady source. Statistics of the adjoint field were integrated over a shorter duration, namely 40 time units, and further ensemble averaged over eighteen independent simulations with the steady source shifted in the homogeneous x and z directions.

Contours of the mean forward and adjoint scalar fields, $\overline{c}$ and $\overline{c^*}$, are reported in figure 2-2; contours of the the root-mean-squares, c'_{rms} and $c^{*\prime}_{rms}$, are plotted in figure 2-3. In both figures colour contours correspond to the forward field and line contours correspond to the adjoint. Note that the streamwise coordinate of the adjoint field is reversed in order to facilitate comparison. When the colour boundaries and the line contours coincide, the forward and adjoint fields are in quantitative agreement, to within the streamwise coordinate transformation. Such agreement is evident in the channel centre and inside the buffer layer, for $\overline{c}$ and $\overline{c^*}$ in figure 2-2 and c'_{rms} and

$c^{*\prime}_{rms}$ in figure 2-3. However, differences among the means and among the root-mean-squares are observed in the log layer, for example $\overline{c^*}$ develops two local maxima in its wall-normal profile (see marked arrows on figure 2-2) which are not observed in $\overline{c}$. The differences are due to the reversed advection by turbulent fluctuations; in a steady laminar flow the forward and adjoint scalar equations are identical to within a coordinate transformation $\tilde{\mathbf{x}} = -\mathbf{x}$. Turbulent fluctuations act against the mean gradients to generate the scalar fluctuations and fluxes. In the adjoint, exchanging ejections and sweeps alters these quantities because of curvature in the mean profile. As a result, the base-state distortions and root-mean-square fluctuations of the forward and adjoint fields differ.

The vertical locations of the maxima in the mean and root-mean-square fields are also plotted in figures 2-2 and 2-3. The results exhibit a degree of mirror symmetry between the forward and adjoint fields, in particular for sources in the channel centre. For sources in the log-layer and below, the y-locations of the maxima of $\overline{c}$ and $\overline{c^*}$ approach and attach to the wall. In contrast, the y-locations of the maxima of c'_{rms} and $c^{*\prime}_{rms}$ lift away from sources in the viscous and buffer layers.

The results raise interesting points: Would a sensor immediately downstream of an unknown source provide the “best" signal for reconstruction? Or would a sensor at lower elevation be preferable because the maxima of the forward field approach the wall with downstream distance? Alternatively, from the standpoint of the adjoint field being the sensitivity of the sensor, should the sensor placement be shifted upward? These questions will be examined in §2.5 by varying the sensor location relative to the source. It should be cautioned that such experiments are only intended to demonstrate the performance of such sensor placements, but in reality the source location is unknown and hence selecting the relative placement of the sensor is not possible.

The duality relation between the forward and adjoint field (2.8) for the instan-

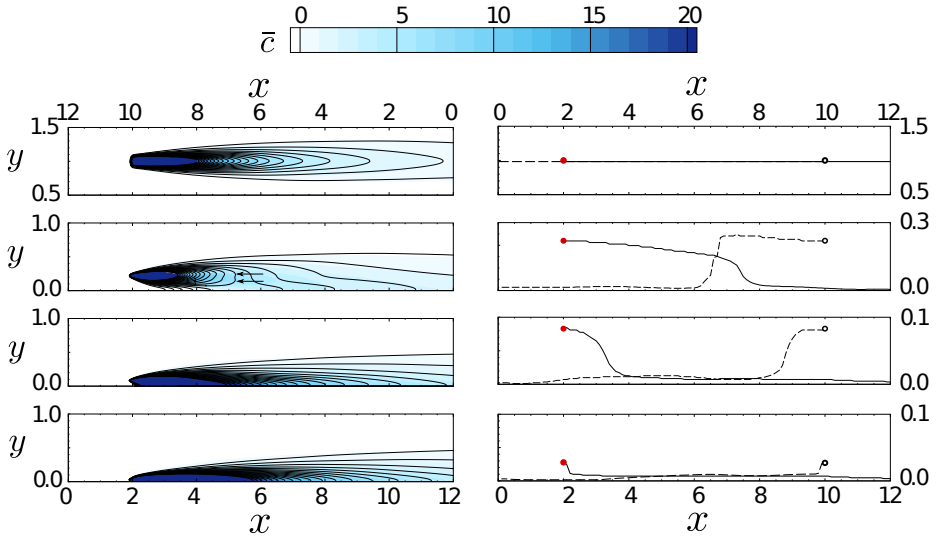

Figure 2-2. Left: side views of the (colour contours) mean forward and (line contours) adjoint scalar fields, from sources at different wall-distances. The bottom abscissae are for forward scalar fields and the top ones are for the adjoint, i.e. the abscissae of the adjoint are reversed. From top to bottom the source locations are in the channel centre ($y^+ = 180$), log layer ($y^+ = 40$), buffer layer ($y^+ = 15$) and sub layer ($y^+ = 5$). Right: the y-location for maximum concentration at different streamwise locations. Solid lines marks $arg\max_y c$ while the dashed lines marks $arg\max_y c^*$.

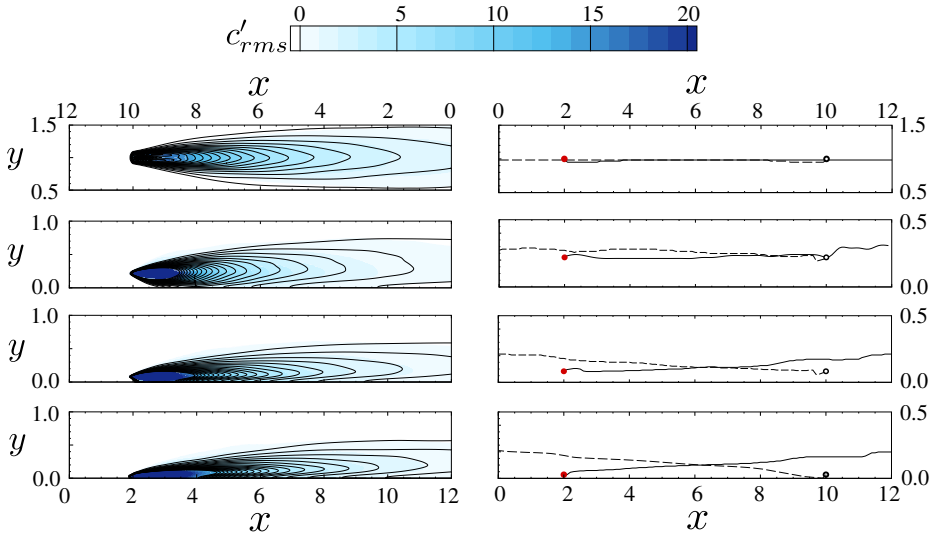

Figure 2-3. Left: side views of the root-mean-square scalar perturbation fields for (colour contours) forward and (line contours) adjoint, from sources at different wall-distances. The bottom abscissae are for forward scalar fields and the top ones are for the adjoint, i.e. the abscissae of the adjoint are reversed. From top to bottom the source locations are in the channel centre ($y^+ = 180$), log layer ($y^+ = 40$), buffer layer ($y^+ = 15$) and sub layer ($y^+ = 5$). Right: the y-location for maximum c'_{rms} at different streamwise locations. Solid lines marks $arg\max_y c'_{rms}$ while the dashed lines marks $arg\max_y c^{*\prime}_{rms}$. The axes on the bottom are for forward scalar fields and those on the top are for adjoint fields.

taneous field is useful in the interpretation of the present results. Recall that the forward field at the sensor location due to an impulse at the source is equal to the adjoint field at the source due to an impulse at the sensor. Therefore, the time-average of the two signals must also be equal,

$$\overline{c}(\mathbf{x}^m;\mathbf{x}^s) = \overline{c^*}(\mathbf{x}^s;\mathbf{x}^m), \tag{2.20}$$

where $\overline{c}(\mathbf{x}^m;\mathbf{x}^s)$ represents the mean scalar at $\mathbf{x}^m$ due to a steady source located at $\mathbf{x}^s$; similarly, $\overline{c^*}(\mathbf{x}^s;\mathbf{x}^m)$ is the average adjoint at $\mathbf{x}^s$ due to a steady source at $\mathbf{x}^m$. This equality holds for any arbitrary source and sensor locations. In the present case, the sensor and source are placed at the same locations in the y and z directions. Therefore, the mean forward and adjoint fields along the streamwise direction, $\mathbf{e}_x$, should become the same function of the source-sensor separation $x^m - x^s$,

$$\overline{c}\left(\mathbf{x}^s + \left(x^m - x^s\right)\mathbf{e}_x;\mathbf{x}^s\right) = \overline{c^*}\left(\mathbf{x}^s;\mathbf{x}^s + \left(x^m - x^s\right)\mathbf{e}_x\right) = \overline{c^*}\left(\mathbf{x}^s - \left(x^m - x^s\right)\mathbf{e}_x;\mathbf{x}^s\right). \tag{2.21}$$

Comparison of the mean forward and adjoint fields as a function of $(x^m - x^s)$ are shown in figure 2-4, and agree at all four wall-normal heights within the channel. Similar equalities could not be derived for the root-mean-square scalar fields. As a result, when plotted as a function of $(x^m - x^s)$, the root-mean-square forward and adjoint scalar fields do not collapse (see figure 2-4).

2.4 Results

2.4.1 Performance of the algorithm

We start with a series of source reconstructions using measurements from a single sensor placed directly downstream of the source. We will examine the effect of different source-sensor separations and also wall-normal heights within the channel. The measurements were obtained by solving the forward flow and scalar equations, and recording the scalar signal at the sensor location, $M(t) = c\left(\mathbf{x}^m, t\right)$.

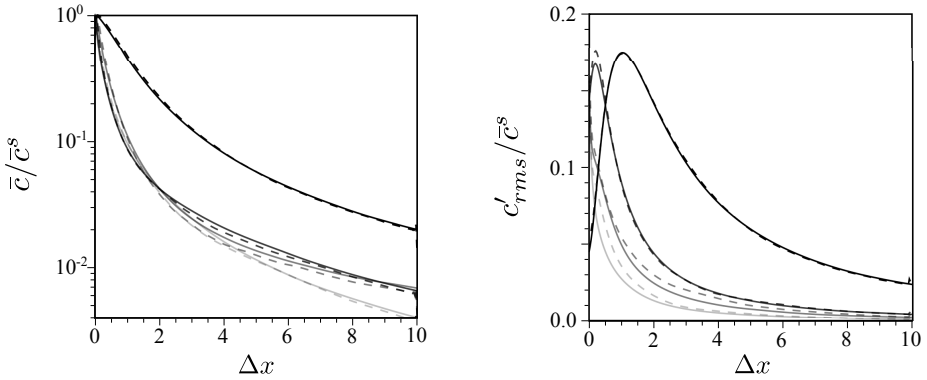

Figure 2-4. Comparison of mean (left) and root-mean-square perturbation (right) scalar fields from the forward (solid lines) and adjoint (dashed lines) simulations. Scalar fields are normalized by $\overline{c}^s = \overline{c}(\mathbf{x}^s)$, and are plotted directly downstream (for forward) and upstream (for adjoint) of the steady source. Sources are put at four different y locations $y^+ = \{180, 40, 15, 5\}$ marked by reduced greyscale levels.

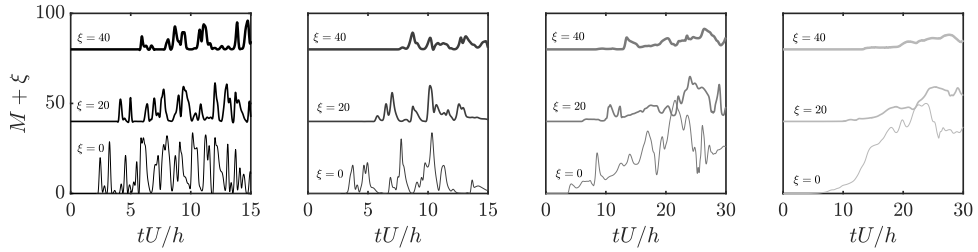

Figure 2-5. Sensor signals for different source-sensor separations, $D = x^m - x^s$, and wall distances. Left to right: Measurements from source-sensor pairs located at channel centre ($y^+ = 180$), log-layer ($y^+ = 40$), buffer layer ($y^+ = 15$) and viscous sublayer ($y^+ = 5$). At each height, three different source-sensor separations are considered , $D = x^m - x^s = \{3, 5, 7\}$ (thin to thick lines). In order to separate their respective measurements signals, the associated M are vertically shifted by an offset $\xi = \{0, 40, 80\}$.

Some sample signals $M(t)$, all from the same realizations of the velocity field, are shown in figure 2-5; for every y-location three value of $D \equiv x^m - x^s = \{3, 5, 7\}$ are compared. In the middle of the channel, a time shift is evident in the measurement signals as the sensor is placed at a larger distance from the source, and its duration is proportional to the scalar advection velocity. The signal intensity is also reduced with increased source-sensor distance due to the action of diffusion. At smaller distances to the wall, the time-shifts in the sensor signals due to increased separation from the source become less prominent. In addition, the measurement signals become smoother, especially in the viscous sublayer. In that region, a shear filtering effect leads to a weak sensitivity of the scalar field to high-frequency velocity fluctuations [52, 53]. Additional, diffusion is dominant and, as a result, the measurements from different downstream sensors are more difficult to distinguish.

Using the measurements, we adopted the adjoint-variational algorithm to reconstruct the source. The initial guess of the source distribution is identically zero, and thus assumes no prior knowledge of its location. In order to gauge convergence of the algorithm, we evaluated the normalized cost functional,

$$\tilde{\epsilon} = \frac{\sum_j \int_0^T \left(M_j(t) - c(\mathbf{x}_j^m, t)\right)^2 dt}{\sum_j \int_0^T M_j^2(t) dt} = \frac{\sum_j \int_0^T \epsilon_j^2(t) dt}{\sum_j \int_0^T M_j^2(t) dt}, \tag{2.22}$$

where j is the sensor index. The stopping criterion for our iterative algorithm is $\tilde{\epsilon} \leq 0.01$ with a maximum possible number of iteration $N_{max} = 50$. Changing these values does not alter the trends reported herein for the reconstruction quality at different wall-normal position and sensor-source separations.

The convergence history of the algorithm is reported in figure 2-6. Each panel corresponds to a different y-location and the increase in line thickness denotes larger source-sensor separation D. For all cases, the adjoint-variational approach minimizes the cost functional until the stopping criterion is satisfied, namely one percent relative error. The different convergence rates are a symptom of different dominant physical processes in the scalar transport problem. Diffusion renders the solution non-unique:

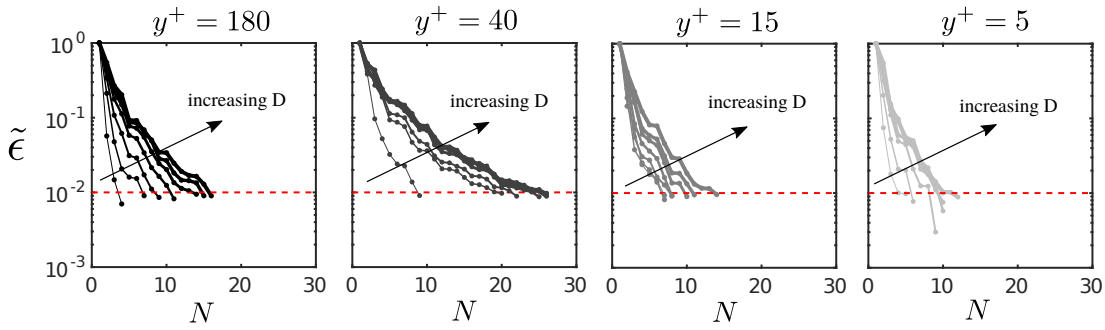

Figure 2-6. Normalized cost functional versus number of iterations N. Left to right: $y^+ = \{180, 40, 15, 5\}$. Larger separations $D = x^m - x^s$ are marked by increased line thickness.

consider for example that in laminar flow a steady measurement signal can be ascribed to a weak nearby source or a high-intensity distant one. As a result, when the effect of diffusion is dominant, which is anticipated to be the case near the wall, the decay rate of the cost functional is fast although the reconstruction is unlikely to match the true source. Conversely, when the system of equations is better conditioned, the search for the optimality condition may require more iterations as seen in the log-layer, but the reconstruction is expected to more faithfully reproduce the source. This qualitative interpretation of the convergence rate will be verified by an examination of the reconstruction quality, and in §2.4.2 by an analysis of relevant scalar statistics.

The reconstructed and true sources are compared in figure 2-7, for the smallest and largest source-sensor separations $D = \{1, 7\}$. In the channel centre and the log layer (top two rows in the figure), the algorithm provides an accurate prediction of the source location and size in the crossflow $(y - z)$ plane. However the reconstructed source is much more elongated in the streamwise direction relative to the true one. In the viscous sublayer, the predicted source distribution has an erroneous high-amplitude region near the sensor, far from the true source location. This result is related to the behaviour of the adjoint scalar field: in figure 2-2, the mean adjoint field decays quickly upstream of the sensor, thus limiting the region of sensor sensitivity. Although a large number of iterative evaluations of conjugate directions were performed in the search algorithm to mitigate this effect, it still remains significant

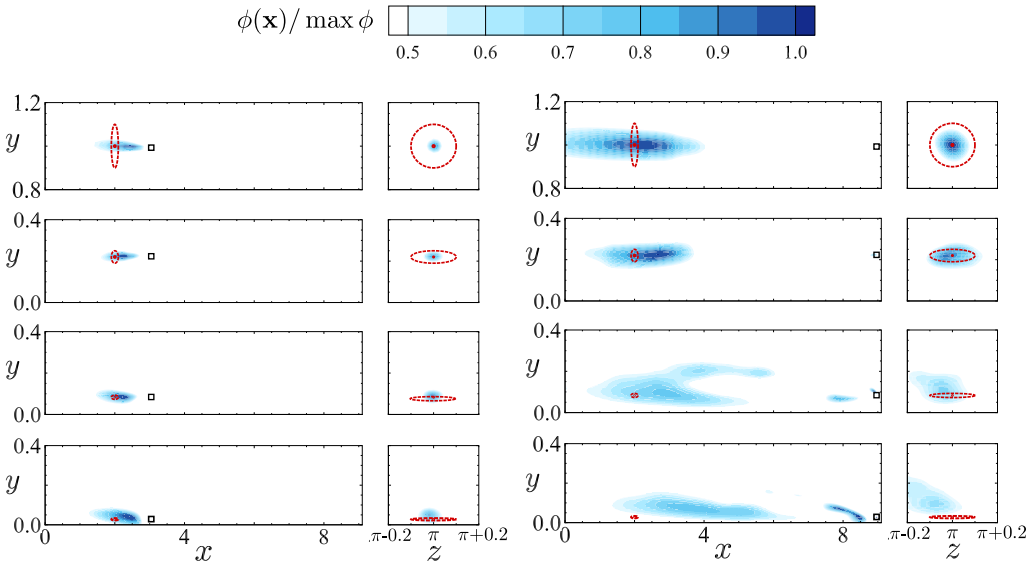

Figure 2-7. Contour of reconstructed source on x-y plane ($z = \pi$) and y-z plane ($x = 2$), normalized by $\max\phi$. Dashed circles mark the centre and outer edge of the true source; the square marks the sensor position. Left: $D = 1$; right: $D = 7$.

in the near-wall region.

The quality of the solution is quantified using the correlation coefficient between the reconstructed and true source distributions, in each of the three spatial direction,

$$R^x_{\phi\phi} = \frac{\frac{1}{L_x}\int_x \langle\phi\rangle^{yz}\langle\phi\rangle^{yz}_T dx}{\langle\phi\rangle^{yz}_{rms}\langle\phi\rangle^{yz}_{T,rms}}, \quad R^y_{\phi\phi} = \frac{\frac{1}{L_y}\int_y \langle\phi\rangle^{xz}\langle\phi\rangle^{xz}_T dx}{\langle\phi\rangle^{xz}_{rms}\langle\phi\rangle^{xz}_{T,rms}}, \quad R^z_{\phi\phi} = \frac{\frac{1}{L_z}\int_z \langle\phi\rangle^{xy}\langle\phi\rangle^{xy}_T dz}{\langle\phi\rangle^{xy}_{rms}\langle\phi\rangle^{xy}_{T,rms}}, \tag{2.23}$$

where ϕ_T is the true source distribution, and the angled brackets $\langle\,\cdot\,\rangle^{ab}$ denote averaging in the a and b directions. These correlations are reported in figure 2-8. Note that the size of the source was reduced at lower wall-normal heights in order to account for the presence of the wall. In this regard, the reconstruction in the y-direction is more challenging for the smaller near-wall sources, relative to the larger ones near the channel centre, and hence the focus will be placed primarily on the reconstruction quality is in x and z directions where the size of the true source is unchanged for all cases. Since the reconstruction is elongated in the streamwise direction, $R^x_{\phi\phi}$ is generally the lowest of the three correlations. The log-layer values of $R^x_{\phi\phi}$ are the highest,

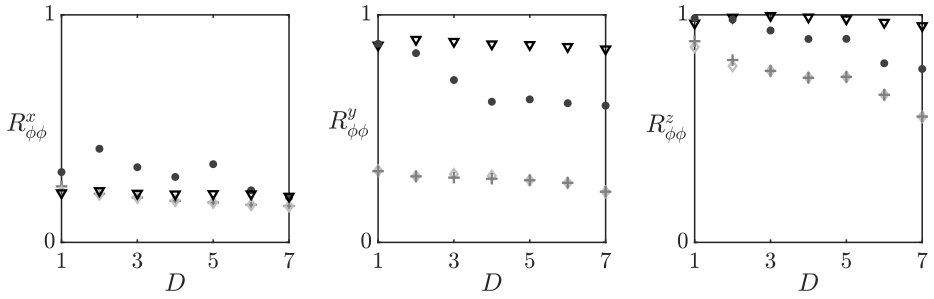

Figure 2-8. Correlation coefficients between reconstructed source ϕ and the true source ϕ_T in x (left), y (middle) and z (right) directions versus source-sensor separation, $D = x^m - x^s$. Symbols $(\triangledown, \bullet, +, \diamond)$ and reduced grayscale intensity correspond to $y^+ = \{180, 40, 15, 5\}$.

for the same relative error in the estimated and true measurements $\tilde{\epsilon}$. Recall that it was in the log layer that the convergence rate of the solution was slowest, yet the identified source most faithfully reproduces the true in comparison to other wall-normal locations. The quality of the reconstruction generally deteriorates in the buffer and viscous layers. There the relative error in the estimated and true measurements $\tilde{\epsilon}$ decays fastest but the identified source deviates most from the true one, which is indicative of the degree of non-uniqueness in the reconstruction near the wall.

The results in figures 2-7 and 2-8 remain qualitatively unchanged for a smaller number of iteration N of the search algorithm. In figure 2-9, the effect of N is shown for a source-sensor pair at the channel centre, and separated by $D = 5$. The reconstruction in y and z directions converges quickly. In contrast, the reconstruction in x continues to improve with iterations, and the correlation coefficient with the true source increases from $R^x_{\phi\phi} = 0.18$ after five iterations to $R^x_{\phi\phi} = 0.24$ after twenty iterations.

Although the predicted source distribution is elongated in the streamwise direction, it reproduces the measurements accurately. It is therefore interesting to consider whether it also reproduces the scalar field, or plume, away from the measurement location, and in particular downstream of the sensor. Figure 2-10 shows a sample comparison of the scalar fields due to the reconstructed and true sources at the channel centre. Differences are clear in the upstream regions of the plumes, but the two fields

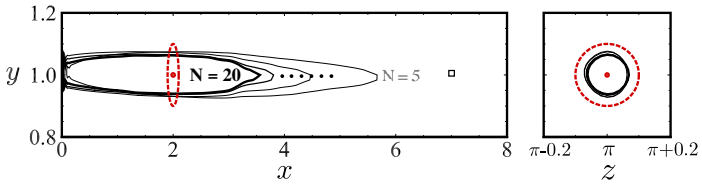

Figure 2-9. Iso-contour $\phi/\phi_{max} = 0.5$ of reconstructed source in the x-y plane ($z = \pi$) and y-z plane ($x = 2$). Results are shown for different numbers of iterations of the adjoint search algorithm, $N = \{5, 10, 15, 20\}$, at the channel centre with source-sensor separation $D = 5$. Dashed circles mark the centre and outer edge of the true source; the square marks the sensor position.

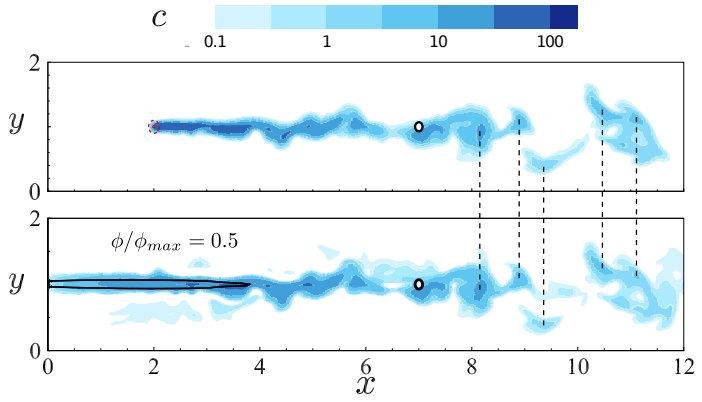

Figure 2-10. Comparison of scalar fields from forward simulations using the true (top) and reconstructed (bottom) sources; the latter is marked by a iso-contour $\phi/\phi_{max} = 0.5$. The closed circle marks the sensor location. Vertical dashed lines identify the coincidence of local concentration maxima in the scalar plumes from the true and reconstructed sources.

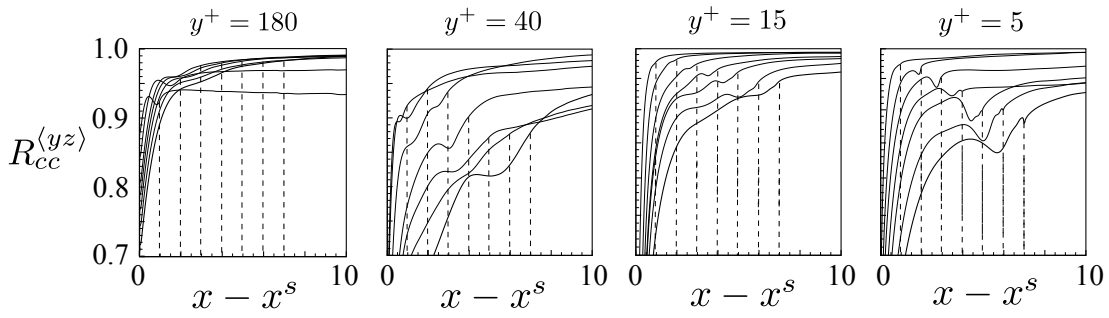

Figure 2-11. Correlation coefficients between reconstructed scalar plume and the true plume downstream of the source. Left to right: $y^+ = \{180, 40, 15, 5\}$. Locations of the sensors are marked by dashed lines with a darker colour as sensors moves farther.

become rather similar as we approach the sensor and downstream of it. The similarity arises due to the correlation between the scalar and the velocity fields [54]. In order to quantify the agreement between the true and reconstructed plumes, we evaluate the correlation coefficient,

$$R_{cc}^{<yz>} = \frac{\dfrac{1}{S_{yz}T}\displaystyle\int_t \int_{y,z} c(\mathbf{x},t;\phi)c(\mathbf{x},t;\phi_T)dydz\,dt}{c(\mathbf{x},t;\phi)_{rms}\; c(\mathbf{x},t;\phi_T)_{rms}}, \tag{2.24}$$

where S_{yz} is the area of the $y-z$ plane; the results are plotted in figure 2-11. The observations from the single realization (figure 2-10) are verified statistically. The correlations between the pairs of scalar fields start increasing around the source location, converge near the sensor position, and demonstrate high-accuracy of plume prediction downstream. These results are encouraging for a number of applications, for example in disaster response where it is important to predict the transport of pollutants while the search for their source continues. One interesting observation is that the correlation between the estimated and true plumes is lowest in the log layer, where the reconstructed and true sources were most correlated. The interpretation is, however, consistent with the earlier discussion: The measurement in the log layer can enable distinction of different sources and hence accurate reconstruction of $\phi(\mathbf{x})$, which reproduces the measurements. However, any small errors in $\phi(\mathbf{x})$ generate differing signals *away from the sensor*.

The reconstruction quality in figures 2-7 and 2-8 indicate that the prediction of the source distribution in the streamwise direction is most challenging. This motivates examination of characteristics of the scalar field along that direction. Particularly informative are two-point statistics that quantify the correlation of measurements due to adjacent sources or adjacent sensors.

2.4.2 Shifting-sensor and shifting-source correlation coefficients

We will examine two correlation coefficients, both evaluated for the sensor signal $c(\mathbf{x}^m, t; \mathbf{x}^s)$. Here the measurement location is denoted $\mathbf{x}^m$ and the source is $\mathbf{x}^s$. In the first case, we will shift the streamwise position of the sensor, $\Delta\mathbf{x}^m = \Delta x^m \mathbf{e}_x$, and examine the correlation of the two measured signals,

$$R^m_{MM}(\Delta x^m, \Delta t^m; D) = \frac{\frac{1}{T}\int_0^T c(\mathbf{x}^m, t; \mathbf{x}^s) c\left(\mathbf{x}^m + \Delta x^m \mathbf{e}_x, t + \Delta t^m; \mathbf{x}^s\right) dt}{c_{rms}(\mathbf{x}^m, t; \mathbf{x}^s)\; c_{rms}\left(\mathbf{x}^m + \Delta x^m \mathbf{e}_x, t + \Delta t^m; \mathbf{x}^s\right)}. \tag{2.25}$$

In the second case, the sensor position will be held fixed, but the streamwise placement of the source will be shifted, $\Delta\mathbf{x}^s = \Delta x^s \mathbf{e}_x$, and the two resulting measurements will again be correlated,

$$R^s_{MM}(\Delta x^s, \Delta t^m; D) = \frac{\frac{1}{T}\int_0^T c(\mathbf{x}^m, t; \mathbf{x}^s) c\left(\mathbf{x}^m, t + \Delta t^m; \mathbf{x}^s + \Delta x^s \mathbf{e}_x\right) dt}{c_{rms}(\mathbf{x}^m, t; \mathbf{x}^s)\; c_{rms}\left(\mathbf{x}^m, t + \Delta t^m; \mathbf{x}^s + \Delta x^s \mathbf{e}_x\right)}. \tag{2.26}$$

The distance $D \equiv x^m - x^s$ is the separation between the reference source and sensor locations in the streamwise direction. In both cases, we take into account the effect of a time-lag in the signal, Δt^m. Notice that these correlation coefficients for the sensor signals were evaluated with the mean, although usually the mean would be subtracted for correlation coefficients. In the current application, the algorithm utilized the full signal and therefore the coefficients evaluated here is equally representative as the one evaluated without the mean for the algorithm.

Using only the fluctuation part would imply that we have knowledge of the mean scalar field (and the source location) ahead of time.

Note that the computation of $R^m_{MM}(\Delta x^m, \Delta t^m)$ only requires a single forward scalar simulation, and measurements are recorded at various sensor locations. The computation of $R^s_{MM}(\Delta x^s, \Delta t^m)$, on the other hand, requires multiple forward simulations of the scalar field each with a different source placement. In appendix B.2.1, a relationship between the forward and adjoint field is derived whereby only a single forward-adjoint loop is needed to compute R^s_{MM}. That expression is reliant on a Taylor hypothesis, and is hence not used in the present computation, but is included in the appendix for the interested reader.

The shifting-sensor and shifting-source correlation coefficients, R^m_{MM} and R^s_{MM}, are plotted in figure 2-12 as functions of Δx and Δt. The four panels correspond to the four wall-normal heights within the channel, $y^{s+} = \{180, 40, 15, 5\}$. The ridge in the contours represents the optimal time lag for the signals from two sensors separated by Δx to achieve the highest correlation. For the shifting-source correlation coefficient, the optimal time shift is nearly zero. For R^m_{MM}, the optimal time shift changes linearly with Δx^m and a clear slope can be identified. The reciprocal of the slope is the transport velocity U_t of the scalar in the streamwise direction. Normalized by viscous units, U_t^+ is compared to the mean-flow speed $\langle U^+ \rangle^{xz}$ in figure 2-13. While the transport and mean-flow speeds agree in the outer part of the channel, the former is appreciably higher near the wall. Similar trend was observed by Quadrio & Luchini [55] who examined the transport of velocity fluctuations; They found agreement between the transport velocity and the mean profile in the bulk, and a nearly constant advection velocity on the order of 10 plus units near the wall.

It is evident that a shift in the sensor location will introduce a shift in the time series of measurements, which will be proportional to the advection time between the two locations. Perhaps less evident is that a downstream shift in the source location does not necessarily yield a similar time-shift in the sensor signal. Consider for example the scalar fields in figure 2-14; beyond an initial transient, the two sources result

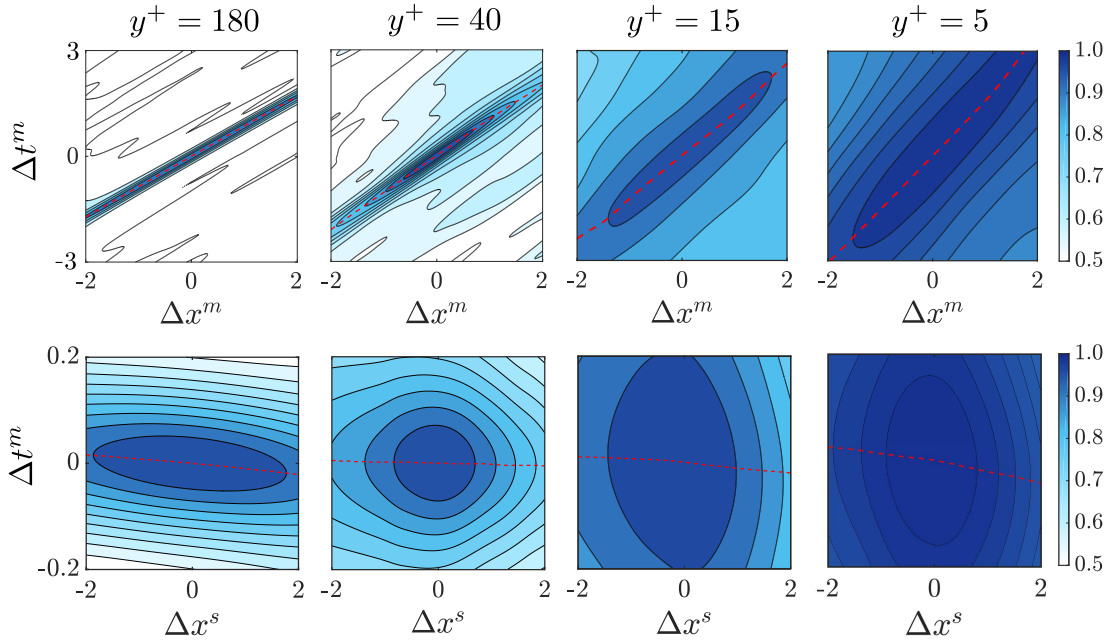

Figure 2-12. Top: Contour plot of shifting-sensor correlation coefficients $R^m_{MM}(\Delta x^m, \Delta t^m; D)$ for $D = 5$ at different wall distances of the source and sensor $y^+ = \{180, 40, 15, 5\}$ (left to right). The dashed lines mark the optimal time shift to obtain largest correlation for any given Δx^m. Bottom: Contour plot of shifting-source correlation coefficients $R^s_{MM}(\Delta x^s, \Delta t^m; D)$ for $D = 5$ at different wall distances $y^+ = \{180, 40, 15, 5\}$ (left to right).

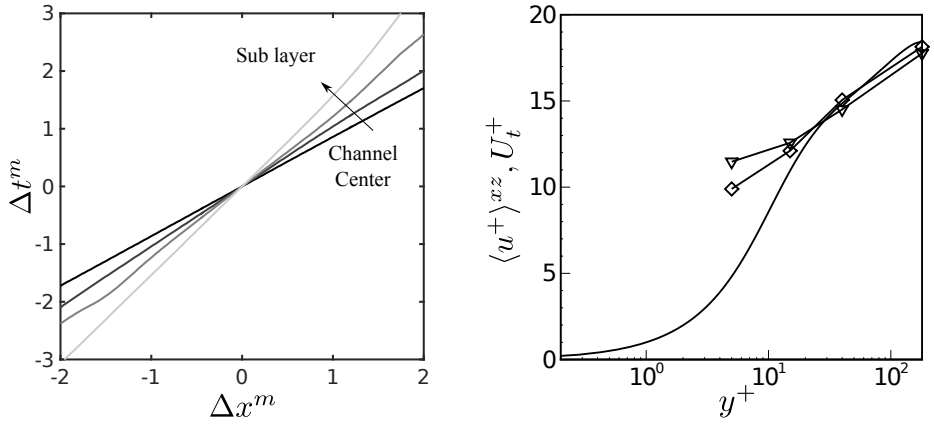

Figure 2-13. (a) Optimal time shift Δt^m vs. sensor location shift Δx^m for $y^+ = 180$, $y^+ = 40$, $y^+ = 15$ and $y^+ = 5$ (From black to light grey). (b) Triangle symbols show the transport velocity $U_t^+ = d\Delta x^m / d\Delta t^m$ calculated from the Δt^m-Δx^m diagram for scalar source at different wall-distance. Diamonds show the transport velocity for u', defined in a similar manner as the transport velocity for c. Line without symbol is the mean velocity profile plotted as a comparison.

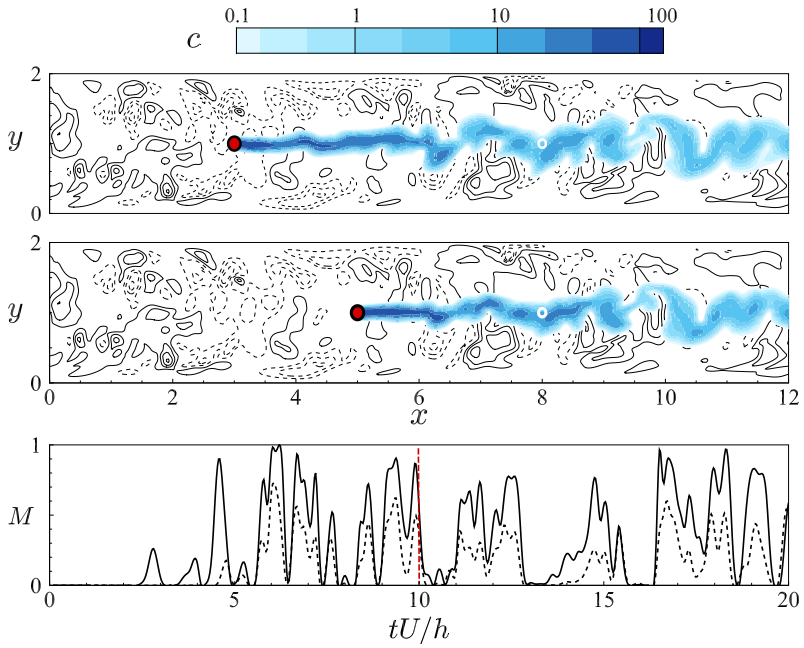

Figure 2-14. Contours of sample scalar fields with sources put in the channel centre at different streamwise locations $x = 3$ and 5, the corresponding vector fields of velocity perturbation and contour of v are also shown in background. On the bottom is the measurement data M taken at the same location for different plumes versus time tU/h. dashed and solid lines represent measurement from the plume at top and middle, respectively.

in very similar scalar fields at the sensor and similar time-trace of the measurement. The above correlation coefficients will quantify this effects.

Using the optimal time shift, both R^s_{MM} and R^m_{MM} are plotted at different wall-normal locations in figure 2-15. The similarity between the shifting-sensor and shifting-source correlation coefficients is evident. In fact, when the velocity field satisfies the Taylor's frozen-eddy hypothesis $\mathbf{u}\left(\mathbf{x}, t + \frac{\Delta x}{\mathcal{U}}\right) = \mathbf{u}\left(\mathbf{x} - \Delta x, t\right)$, i.e. is merely transported downstream with constant velocity $\mathcal{U}$, it can be shown that shifting the sensor is equivalent to shifting the source with a time lag — a proof is provided in Appendix B.2.2. As a result, for such conditions, the shifting-sensor correlation is a mirror image of the shifting-source correlation, $R^m_{MM}(\Delta x, \frac{\Delta x}{U_t}; D) = R^s_{MM}(-\Delta x, 0; D)$.

The correlation remains above 90% for all cases when the displacement is on the order of $\Delta x^{s,m} \simeq 1$, which highlights the difficulty of the scalar reconstruction: Based on R^s_{MM}, an appreciable shift in the source location only yields a small change in the

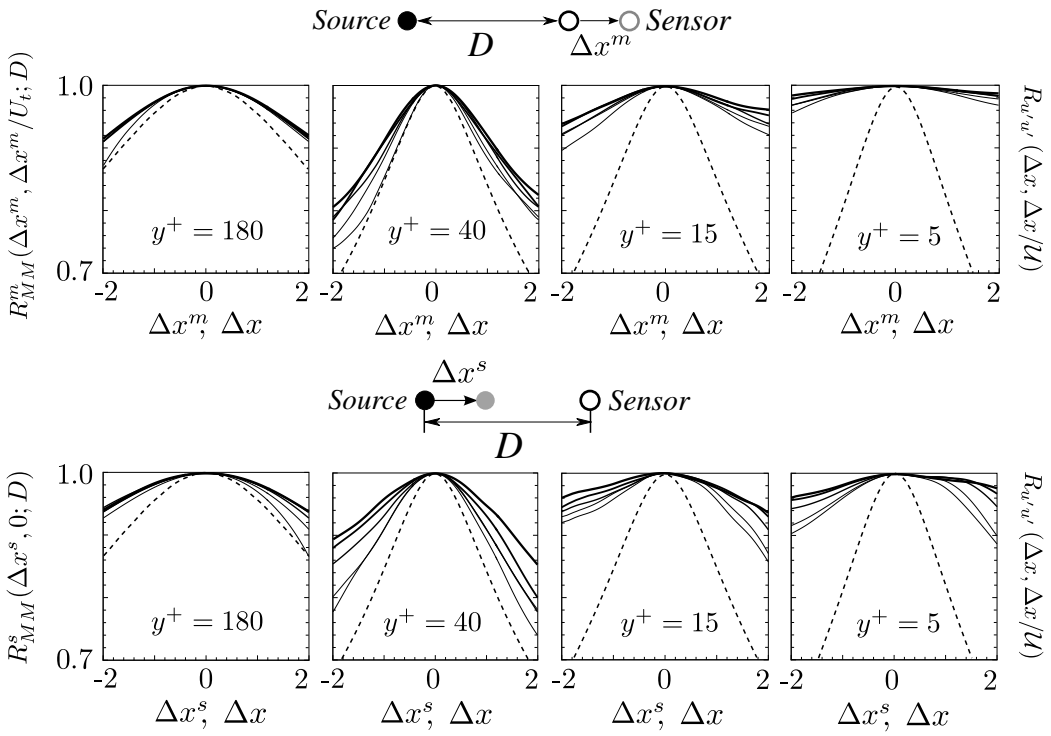

Figure 2-15. (top) Shifting-source correlation coefficients $R^s_{MM}(\Delta x^s, 0; D)$ at (left to right) $y^+ = \{180, 40, 15, 5\}$ and (thin to thick) $D = \{3, 4, 5, 6, 7\}$. (bottom) The corresponding optimal shifting-sensor correlation coefficients $R^m_{MM}(\Delta x^m, \Delta t^m; D)$. Dashed lines shows the spatiotemporal correlation for u' at the same y locations as references.

measurements; The interpretation based on R^m_{MM} is that the measurements based on different sensor placements in the streamwise direction are not easily distinguished.

The present results also explain the convergence rate of the adjoint-variational algorithm (figures 2-6 and 2-8 in §2.4). The coefficient R^s_{MM} (figure 2-15) decays fastest in the log-layer, which demonstrates that two sources with a streamwise displacement produce more distinct sensor signals in that region compared to any other wall-normal heights. This can be interpreted, albeit informally, as a measure of the uniqueness of the solution. In this region, the convergence rate of the cost functional is slow (figure 2-6), but the same reduction in the cost functional leads to the best reconstruction quality in the streamwise direction (figure 2-8). In the near wall region, where the shifting-source correlation is highest, the signals from various sources are highly correlated and it is thus difficult to distinguish them. It is therefore relatively easy to identify a solution which yields a similar signal to the measurement data, but it is unlikely to be unique since many source distributions can result in the same sensor data. Therefore in the near-wall regions the convergence of the cost functional is faster than the log-layer, but the quality of the reconstruction in the streamwise direction is poorer.

The behaviour of the correlation coefficient is due to a combined effects of diffusion and dispersion. On the one hand, diffusion blurs the scalar signal, thus making it harder to differentiate the measurements from different sources. And since the cumulative influence of diffusion increases with increased separation between the source and sensor, the correlation coefficients increase at larger D (thicker lines in the figure). Diffusion is also responsible for the increase in the correlation as the wall is approached as demonstrated in the two right panels which correspond to $y^+ = \{15, 5\}$. The effect of dispersion, on the other hand, is more difficult to characterize: If the turbulence decorrelates quickly, the measurements from two sources or at two sensors should differ; However dispersion does not act alone because, by stretching the scalar

field, it enhances the action of diffusion. The correlation coefficients of the streamwise velocity perturbation,

$$R_{u'u'}(\Delta x, \Delta t) = \frac{\overline{u'(x,t)u'(x+\Delta x, t+\Delta t)}}{u'^2_{rms}}, \tag{2.27}$$

is included in figure 2-15. The results are plotted for the time shift $\Delta t = \Delta x/\mathcal{U}$ that maximizes the correlation coefficient. Here $\mathcal{U}$ is the streamwise transport speed for velocity perturbations, which is similar to the scalar transport velocity U_t. The velocity signal is most preserved at the channel centre and, as a result, despite the relatively weak diffusion at that location the scalar correlations remain high. In the log layer, the velocity decorrelates relatively quickly and hence the scalar correlation also decays. Nearer to the wall, the decorrelation of the velocity field is not as effective because the diffusion becomes dominant and the measurements are highly correlated.

2.4.3 Physical mechanisms

The asserted relative importance of dispersion and diffusion can be quantified by evaluating the budget equation for the mean scalar variance $\overline{c^2}$ outside the source,

$$0 = \frac{\partial \overline{c^2}}{\partial t} = \underbrace{-U\frac{\partial \overline{c^2}}{\partial x}}_{\mathcal{A}_l} \underbrace{-\nabla \cdot \overline{\mathbf{u}'c^2}}_{\mathcal{D}_l} + \underbrace{\frac{1}{RePr}\nabla^2\overline{c^2}}_{\nu_l} \underbrace{-\frac{2}{RePr}\left(\overline{\nabla c \cdot \nabla c}\right)}_{\mathcal{E}_l}. \tag{2.28}$$

The advection of the scalar variance by the mean velocity is denoted $\mathcal{A}_l$, and is balanced by dispersion by the turbulent fluctuations $\mathcal{D}_l$, molecular diffusion ν_l, and dissipation $\mathcal{E}_l$. The streamwise decay of the variance field is encapsulated in the mean advection term. In order to take into account the development of the scalar plume between the source and any potential sensor location, we normalize the equation by $U\overline{c^2}$ and integrate it along the streamwise direction from x^{s+}, immediately downstream of the source, to an arbitrary x. The resulting balance equation for the decay in

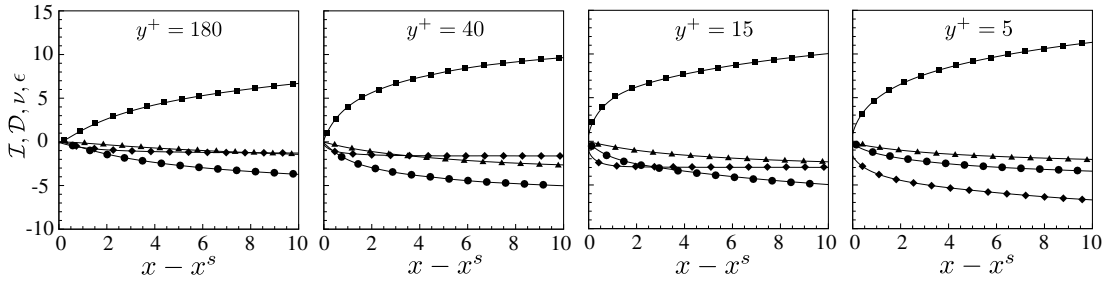

Figure 2-16. Terms $\mathcal{I}$ (■), ν(◆), $\mathcal{D}$(●), $\mathcal{E}$(▲) in the balance equation (2.29) for different wall-normal locations. Left to right: $y^+ = \{180, 40, 15, 5\}$.

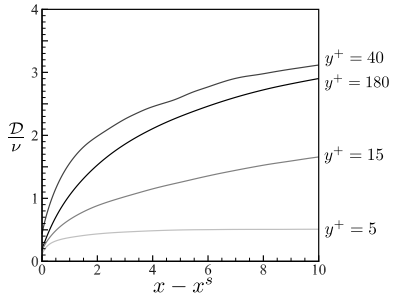

Figure 2-17. The ratio between terms $\mathcal{D}$(●) and ν(◆) in the balance equation (2.29) downstream of the source. Lighter line represents smaller wall-normal height of the source, $y^+ = \{180, 40, 15, 5\}$.

concentration intensity is therefore,

$$\underbrace{\ln \frac{\overline{c^2}|_{x^{s+}}}{\overline{c^2}|_x}}_{\mathcal{I}} \underbrace{- \int_{x^{s+}}^{x} \frac{1}{U\overline{c^2}} \nabla \cdot \overline{\mathbf{u}' c^2} dx}_{\mathcal{D}} + \underbrace{\int_{x^{s+}}^{x} \frac{1}{U\overline{c^2}} \frac{1}{RePr} \nabla^2 \overline{c^2} dx}_{\nu} \underbrace{- \int_{x^{s+}}^{x} \frac{1}{U\overline{c^2}} \frac{2}{RePr} \left(\overline{\nabla c \cdot \nabla c}\right) dx}_{\mathcal{E}} = 0. \tag{2.29}$$

Terms in the above balance equation are plotted in figure 2-16 for different heights in the channel. Dissipation remains relatively unimportant at all heights, and turbulent dispersion $\mathcal{D}$ is dominant in the channel centre and log layer. Molecular diffusion is prominent in the near-wall regions, $y^+ = \{15, 5\}$. This effect is highlighted by evaluating the ratio of the turbulent dispersion and diffusion terms (figure 2-17). The highest ratio appears in the log layer, representing more intense turbulent activities and a stronger dispersion compared to the channel centre. The results are in good agreement with figure 2-15(a), where we show that the ability to differentiate different sources locations is the best in the log-layer. Therefore the log-layer cases are the

least ill-posed among all especially regarding source reconstruction in x direction. As a result, with the same level of measurement discrepancy ($\tilde{\epsilon}$), it will has the closest solution to the true source.

2.5 Discussion

The results examined so far demonstrate that diffusion undermines the performance of the adjoint-variational algorithm in determining the true source location. In addition, the reconstruction of the source distribution in the streamwise direction is most challenging, which was explained in terms of the shifting-source correlation. The algorithmic performance was examined when the sensor is immediately downstream of the source. It was shown that the scalar plume has a tendency to shift towards the wall. It is therefore important to verify the impact of adjusting the sensor position based on this observation. Also note that, in real conditions, the locations of the source is unknown and precise relative placement of the sensor, for example immediately downstream, is not possible to plan. In many applications, multiple sensors are permanently installed and the objective is to interpret their measurements — a configuration that is also examine in this section.

We first consider the region of mean shear, where we evaluate alternate placements of the sensor and the performance of the search algorithm. Instead of positioning the sensor directly downstream of the source, we displace it closer to the wall motivated by the forward mean field (figure 2-2). Two sensor positions would seem of interest: (i) the location where the mean forward scalar concentration is largest and (ii) the location that yields the largest mean adjoint signal at the true source location (not the peak of a particular adjoint plume, but the largest value of $\overline{c^*}\,(x^s)$ for all possible sensor heights). Due to the duality relation (2.8) and its time-average, $\bar{c}(\mathbf{x}^m;\mathbf{x}^s) = \overline{c^*}(\mathbf{x}^s;\mathbf{x}^m)$ and therefore both placements (i) and (ii) coincide.

Figure 2-18 compares the source reconstruction from sensors directly downstream

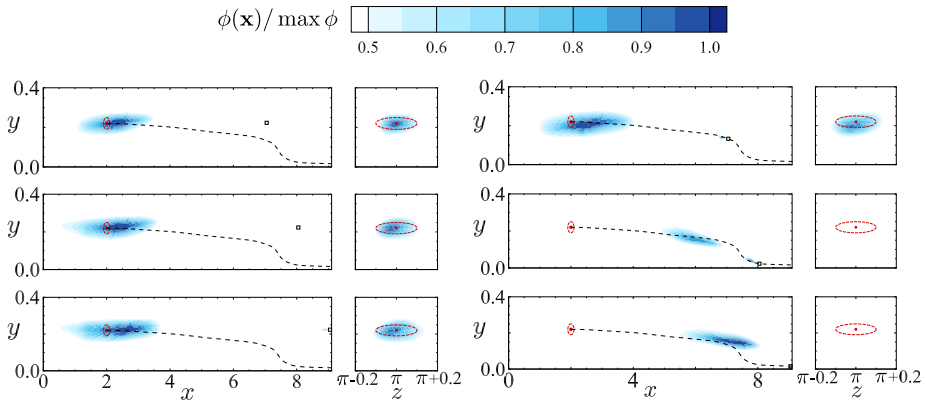

Figure 2-18. Contours of reconstructed source on x-y plane ($z = \pi$) and y-z plane ($x = 2$), normalized by $\max\phi$. Dashed circles mark the centre and outer edge of the true source. Left: sensor directly downstream of the source; Right: sensor placed at the maxima of mean forward field. Horizontal distance from the sensor to the source is $D = x^m - x^s = \{5, 6, 7\}$ from top to bottom. The dashed lines mark the location of the maximum mean scalar concentration, and are reproduced from figure 2-2.

of the sources and others at the locations of the peaks in the mean forward plumes. The quality of the reconstruction is visibly compromised as the sensor are placed nearer to the wall. When the scalar plume enters the near-wall region, it is subjected to slow advection velocities and increased relative importance of diffusive effects. As a result, even though the peak concentration might be close to the surface, the interpretation of a sensor signal from such location is highly obfuscated by diffusive effects. This trend is most pronounced when the sensor is inside the viscous sublayer, even when the mean scalar concentration $\overline{c}$ is large.

In monitoring applications, since there is no prior knowledge of the source location, often multiple distributed sensors are used. The adjoint-variational search algorithm described in §2.2.2 was derived for multiple sensors, and its computational cost per forward-adjoint loop is independent of the number of measurements sites. From the standpoint of the adjoint fields of the collection of sensors, which span a larger domain than a single one, the monitored search area is effectively enlarged which renders the problem more difficult. On the other hand, the various measurements sample more information from the dispersed scalar field which could facilitate an improved source

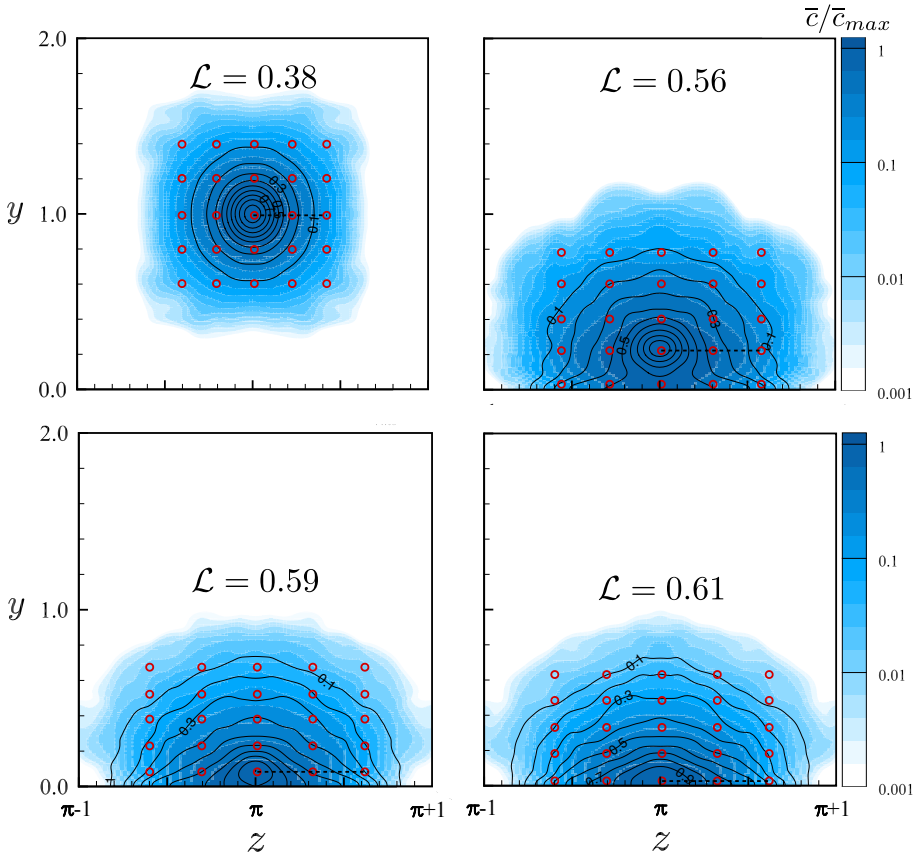

Figure 2-19. Placement of sensor (red circles) in the cross-flow plane at a distance $D = 5$ from the source. Flood contours show the mean forward scalar field normalized by its maximum value, $\overline{c}/\overline{c}_{max}$, on the sensing plane. Line contours correspond to the correlation coefficient between $c(\mathbf{x}; t)$ and the measurement data of the middle sensor, or R_{cM}. From left to right, top to bottom are the results for decreasing wall-distances.

reconstruction. This last view is supported by an earlier effort to reconstruct the time-history of scalar release from a source at a known location [5], where the increase of the mass sampled by additional sensors was shown to correlate with improved performance of the algorithm. Whether additional sensors can similarly improve the accuracy of the spatial source reconstruction is examined here.

The optimal placement of sensors is a subject worthy of its own study [see e.g. 29, 30]; for the present purposes we adopt a simple approach. We consider a regular distribution of 25 sensors at distance $D = x^m - x^s = 5$ from the source. Their arrangement was chosen to ensure coverage of the entire plume. Specifically, the sensor

spacing was set such that the correlation of the scalar signals at the central and the outermost sensors,

$$R_{cM}(\Delta y, \Delta z) \equiv \frac{\dfrac{1}{T}\displaystyle\int_0^T c(\mathbf{x}^m, t)c\left(\mathbf{x}^m + \Delta\mathbf{x}^m, t; \mathbf{x}^s\right) dt}{c_{rms}(\mathbf{x}^m, t)\; c_{rms}\left(\mathbf{x}^m + \Delta\mathbf{x}^m\right)} \tag{2.30}$$

where $\Delta\mathbf{x}^m = (0, \Delta y, \Delta z)$, decayed to an infinitesimal value. Contours of R_{cM} (lines) and sensor locations (symbols) are reported in figure 2-19. The sensitivity of each sensor in the array to the true source is given by its mean adjoint scalar field due to a steady release from its site, and evaluated at the true-source position. Taking advantage of the derived forward-adjoint relation for the mean scalar field (2.20), the same sensitivity can be obtained using a single forward computation, and evaluating the mean forward field $\overline{c}$ in the sensing plane (see flood contours in figure 2-19).

An integral lengthscale of the plume can be obtained from the correlation coefficient,

$$\mathcal{L} = \sqrt{\int_S R_{cM} dydz}, \tag{2.31}$$

and is displayed in figure 2-19. The integral scale is smallest at the channel centre when mean advection is appreciable, and increases in size in in the active near-wall turbulence region where the scalar disperses and diffuses more effectively. The sensor separation was set to half this integral length scale, which guaranteed coverage of the scalar plume.

The same stopping criterion was adopted in the search algorithm, namely $\tilde{\epsilon} \leq 0.01$, and the convergence history is reported in figure 2-20. In general, more iterations are required for convergence with multiple sensors than for a single measurement location. This trend is partly due to the increased search domain spanned by the adjoint of multiple sensors and also due to the the difficulty of estimating a source that reproduces more measurements signals, or information.

Contours of the reconstructed sources are shown in figure 2-21, where results from the single-sensor experiments are reproduced at left for comparison and those for

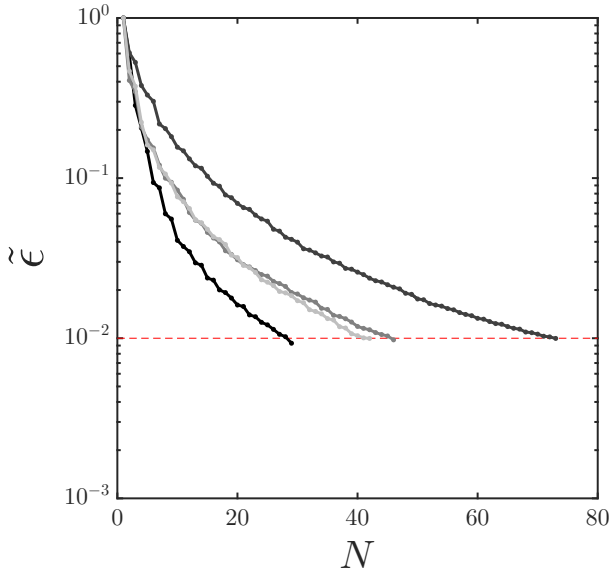

Figure 2-20. Relative difference between reconstructed and measured sensor signals versus number of iterations N for multiple sensor cases. From left to right, top to bottom the y-location of the source is: $y^+ = 180$, $y^+ = 40$, $y^+ = 15$ and $y^+ = 5$.

multiple sensors are at right. With additional measurements, we observe improved reconstruction, in particular away from the wall where the estimated $\phi(\mathbf{x})$ becomes more concentrated in the streamwise direction. The improvement near the wall, however, appears less substantial.

The quality of source reconstruction is evaluated by computing the correlation coefficients between the true and estimated sources (equation 2.23). Comparisons of these values for a single and multiple sensors are reported in figure 2-22. Despite the larger area covered by multiple sensors, an overall improvement in the correlations is achieved with additional measurements, for example in the wall-normal and spanwise directions in the log layer. The additional sensors can sample the dispersed scalar in this region, and yield a more accurate interpretation of the source. The reconstruction is also improved in the streamwise direction at the channel centre, although it remains poor in the near-wall region due to the irreversible influence of diffusion that renders the solution non-unique and, as a result, the problem ill-posed.

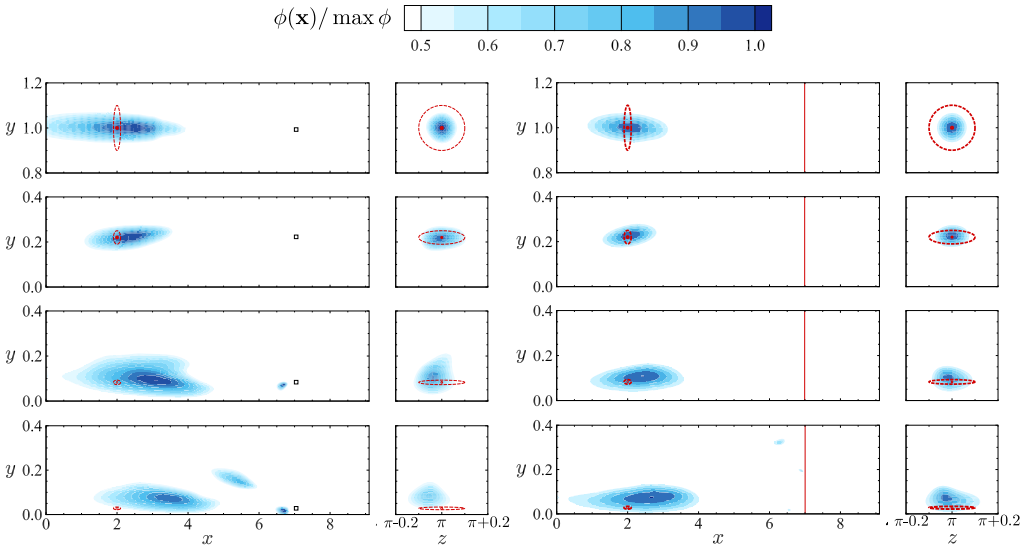

Figure 2-21. Contours of reconstructed source on x-y plane ($z = \pi$) and y-z plane ($x = 2$), normalized by $\max\phi$. Dashed circles mark the centre and outer edge of the true source. Left: single sensor arrangement; Right: 25-sensor arrangement. Distance from the sensor plane to the source is $D = x^m - x^s = 5$.

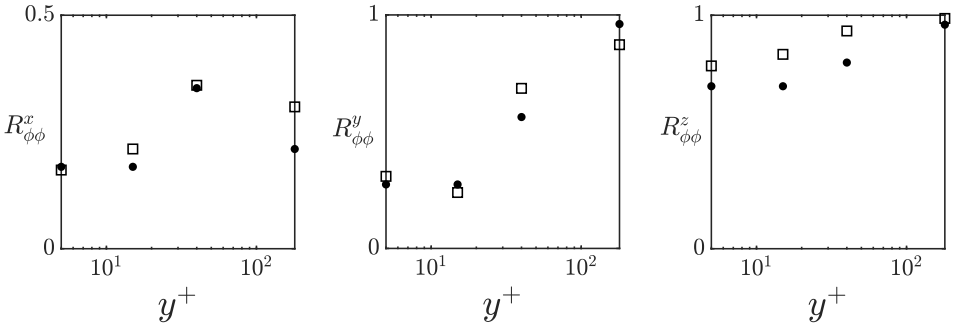

Figure 2-22. Correlation coefficients between reconstructed source and the true source in x (left), y (middle) and z (right) directions with 1 sensor (closed circles) and 25 sensors (open squares).

Use of multiple sensors is anticipated to become more urgent at higher Reynolds numbers. Two scenarios should, however, be distinguished in terms of the Péclet number, $Pe = Re\,Sc$. In the first, Re is increased while Sc is constant and therefore Pe also becomes large. As a result, dispersion is dominant and the scalar is fragmented into small parcels that are advected by the flow. Each isolated sensor thus detects a very limited fraction of the released scalar and reconstruction quality will depend on the total number of sensors. This condition naturally arises in turbulent boundary layers where Re increases with downstream distance. In the second scenario, $Re \to \infty$ is increased but $Sc \propto 1/Re$ and therefore Pe is constant. This configuration will feature very effective diffusion of the dispersed scalar and, as a result, the inverse problem is anticipated to be very ill conditioned and the reconstruction of the source very challenging, even with multiple sensors.

2.6 Conclusions

When a passive scalar is released in a turbulent environment, even from a steady source, it is dispersed by the turbulence eddies and diffused as it advects downstream. A remote sensor receives a highly intermittent signal that is difficult to relate back to the unknown source location. We proposed an adjoint-variational algorithm to perform this source-reconstruction from remote measurements, and evaluated its performance in turbulent channel flow. The problem was formulated as a constrained minimization, where the cost functional is proportional to the difference between the true measurements and their prediction from an estimated source. A conjugate gradient method was used to minimize the Hamiltonian whose gradient was evaluated using the discrete forward and adjoint scalar advection-diffusion equations. Since the algorithm is an adjoint-variational approach, it is equally applicable to a single or multiple sensors without increasing the computational cost of each iteration.

The performance of the algorithm was tested at different locations within the

channel flow and for increasing sensor-source separations. The quality of the reconstructed source was evaluated in terms of its correlation coefficient with the true one, in each of the three spatial coordinates. In general, the correlations were highest away from the wall, and decrease in the near-wall region and with increase source-sensor separation. The reconstructed sources more faithfully approximated the true ones in the cross-stream directions, but were too elongated in the streamwise direction. This trend was explained by computing the shifting-sensor and shifting-source correlations which were shown to decay very slowly in the streamwise direction: Two streamwise-separated sources generate very highly correlated measurements at the sensor and are hence very difficult to distinguish; Conversely two streamwise-separated sensors have very highly correlated signals from an upstream source, and hence the sensor placement in this coordinate is difficult to optimize. It is also noteworthy that, even though the algorithm aims to reproduce measurements at the sensor location, the entire scalar plume downstream of the sensor was also shown to correlate well with the true field.

The scalar budget was examined in order to explain these trends in terms of physical processes, in particular turbulent dispersion, diffusion and dissipation. In the log layer, the effect of dispersion is the most pronounced and, since it is reversible, the sensor can provide a relatively good reconstruction of the source. In the near-wall region, however, diffusion plays a more important role by smoothing, or filtering, the scalar signal. This process is irreversible, and hence the reconstruction problem becomes more challenging.

Since prior knowledge of the source location cannot be assumed, multiple sensors are often adopted. We examined the performance of the algorithm when 25 sensors are placed downstream of the source and span the extent of the plume. Although their combined adjoint field spans a much larger search region, the multiple sensors also collect more information from the dispersed scalar. Relative to an isolated mea-

surement, the source-reconstruction quality was improved in the streamwise direction when the source is near the channel centre, because dispersion is dominant.

Future research should examine the optimal placements of isolated and networks of sensors, which deliver the optimal reconstruction of an unknown source distribution. Moreover, when multiple sensors and types of measurements are available, their optimal weighting should be evaluated.

Chapter 3

Optimal sensor placement for spatial reconstruction of scalar sources in turbulent channel flow

3.1 Introduction

A key challenge for pollution control is to determine the spatial distribution of the source release based on remote sensor measurements. Being able to monitor a certain region and quickly identify the source of a pollution release, for example PM2.5, from optimized sensor networks has become an important topic in recent years [56]. Locating the pollution source also provides diagnostic information for the design of fuel-related systems such as the internal combustion engine. However, reconstructing the source in a turbulent environment is a challenging problem, particularly because the local gradient of the signal does not provide meaningful information for the source location, which prevents the use of chemotaxis-based approaches as in low-Reynolds number scenarios [57]. In high-Reynolds number scenarios, scalar plumes are broken into smaller patches due to turbulent dispersion and the signal becomes intermittent. In addition, it has been shown in the canonical channel flow scenario that the scalar field becomes highly correlated with streamwise velocity fluctuations [58], and quickly "forgets" its initial state, making the differentiation of signals from different sources locations extremely hard in fully turbulent environments [6]. In this work, we formulate

the problem of scalar source reconstruction in a turbulent channel as an optimization problem that is constrained by the governing equations of a passive scalar transport. The objective cost function to minimize here quantifies the discrepancies between the sensor signals and the ones associated to the estimated source.

In any application, the potentialities of source location identification critically depend on the design of the sensor network. Accordingly, how to arrange the sensor network or design the weight of acquired information from existing sensors in order to ensure satisfactory reconstruction performances is another valuable and important topic. The objective of finding the optimal sensor placement is here expressed as the minimization of the condition number of the Hessian matrix that is associated to the cost function in the source reconstruction problem. For an efficient tracking of the Hessian spectrum in terms of computational cost as the sensors are gradually moved to their optimal locations, we further introduce a subspace-tracking algorithm within the condition number optimization procedure. The algorithm is tested in a turbulent channel flow for different search regions and the improvement for using the optimal sensor is demonstrated.

3.1.1 Scalar source reconstruction

Numerous attempts have been conducted to establish algorithms to reconstruct the spatial information of the source. Liu & Zhai [13] summarized previous algorithms into three categories: forward, backward and probability methods. The forward methods utilize only forward simulations to adjust assumed source parameters based on the deviation between the simulated outcome and true measurements [14–18], while backward methods rely on solving backwards in time the scalar transport equation with a non-physical stabilizing term to trace back from the end status to the initial source information [19, 20]. Probability methods are derived from a Bayesian formulation of the source identification problem. They either try to estimate the Probability

Density Function (PDF) of the source parameters or to maximize a probability objective function [21–23]. In this study, however, we are more concerned about whether or not the approach utilizes the relation between potential source locations and corresponding measurement by incorporating the scalar transport equation. Therefore, we here prefer to classify search algorithms into adaptive and model-based methods, following the categorization by Cerizza *et al.* [5]. Adaptive methods are more inspired by the trajectories of animals and insects and treat the fluid system as a black box [35–37]. Model-based methods, on the other hand, rely on the use the scalar transport equation and on an accurate relation between the source distribution and the measurement data. These methods can benefit from the growing ability of numerical simulation techniques and stored database of complex flow simulations. They are our primary focus in this work.

Gorelick *et al.* [14] first performed separate forward simulations for impulses at different potential source locations and defined a unit impulse-response matrix (the "concentration response matrix"). Different rows of the matrix are measurement data of unit releases from different potential source locations. Other similar works also incorporate this impulse-response relation and adopted different optimization algorithms to find the initial source distribution [4, 15–18]. While previous studies have obtained promising results for low-dimensional scenarios, constructing the impulse-response matrix (whether for temporal or spatial problems) explicitly for three-dimensional problems is nearly impossible because of the required large number of forward simulations. Some traditional optimization algorithms have been adopted in combination with forward and adjoint simulations to avoid explicitly building the impulse-response matrix. Huang *et al.* [24] used a conjugate gradient method formed in an adjoint-looping manner to simultaneously reconstruct the spatial and temporal distribution of a scalar source in a steady flow environment. Cerizza *et al.* [5] reconstructed the temporal signal of a source release in a turbulent channel flow by solving the forward

and adjoint transport equations repetitively. Wang *et al.* [6] follows a similar idea and tried to reconstruct the spatial distribution of a concentrated source in turbulent channel flow. Although these methods did not construct the impulse-response relation explicitly, they still rely on the corresponding relation implicitly.

For model-based methods, whatever the impulse-response is explicitly formed or not, the ability to invert this matrix is very important to perform accurate source reconstruction. Therefore, we aim to improve the condition of the impulse-response matrix, which can be characterized by a condition number based on the singular values of this matrix, and obtain better reconstruction results by changing the sensor placements in order to minimize its condition number, as detailed in the following.

3.1.2 Optimal sensor placement

The problem of optimal sensor placement has been formulated within various frameworks. In the context of velocity state reconstruction, Mokhasi & Rempfer [25] chose their optimal sensor placement to correspond to the local maxima of the dominant modes of a proper orthogonal decomposition (POD). Similar formulations can be found in the works by Yildirim *et al.* [26] and Cohen *et al.* [27]. Optimal sensor placement has also been a subject of interest in the field of flow control. Burns & King [59] shows that the linear feedback laws and structure of the functional gains can provide useful information about the sensor locations. A recent work by Akhtar *et al.* [28] used the functional gains to identify appropriate sensor locations.

Mons *et al.* [29] proposed an algorithm to find the optimal sensor placement by maximizing the sensitivity with respect to a change in the initial and boundary conditions. This approach was formed in an iterative procedure that utilizes both forward and adjoint simulations, and aimed to enhance the efficiency of variational data assimilation (DA) procedure and was applied to a two-dimensional unsteady flow scenario. In our problem, when search in a confined region, improvement of the search algorithm

is not guaranteed by enhancing the sensitivity to any particular source location in the region, but rather by the attempt to “equalize" the sensitivity to different source distributions in the search region. Mathematically, this is equivalent as minimizing the condition number of the system. It is worth noticing that the work by Kang & Xu [30] to maximize the observability of the system, approximated by the method of practical Gramian matrix to determine the optimal sensor placement is equivalent as maximizing the smallest eigenvalue of the Gramian matrix. When applied to one-dimensional Burger's equation, it has obtained a significant improvement of the observability for the initial flow state. When applied to much complicated systems in three-dimensional space, more efficient algorithms for estimating the eigenvalues of the system is needed. Normally, to procedure of obtaining the smallest and largest eigenvalues can also be formulated as optimization problem and incorporate a similar iterative method as Mons *et al.* [29]. However, due to the huge number of iterations required to obtain the smallest eigenvalue, this becomes nearly impossible to perform. Therefore, in the current study, the condition number of the Hessian matrix can be instead represented by

$$\kappa_I = \lambda_1/\lambda_I,$$

where I is an empirical index that should be large enough to represent the trend of the spectrum of the system. Our objective is to minimize this condition number to find the optimal sensor placements. This requires efficient calculation of the principle eigenvalues of a system that is changing as the sensors move gradually to their optimal locations. In large-dimension systems, it is not applicable to perform repetitive Singular Vector Decomposition (SVD) for every possible sensor placement. Therefore, we incorporate the idea of subspace tracking method to quickly track the principle subspace of a changing system.

3.1.3 Subspace tracking method

Oftentimes, high-dimensional dynamical systems can be well-summarized in lower-dimensional subspaces. The singular value decomposition (SVD) of the input-output response is one of the most informative way of summarizing the dynamics of the system and is applied in current study. Subspace tracking methods have been widely used in signal processing when dealing with incomplete or rapidly changing information. In the context of signal processing, it is necessary to keep track of a low-rank approximation (singular values and the corresponding vectors) of the covariance matrix. In most scenarios, this matrix would vary slowly with time, especially when new information keeps accumulating and constant updating of the system is needed. Since repetitive SVD is prohibitive because of the large demand of computation, the brute force approach of evaluating spectrum for exhaustive tests for different sensor networks is not an option. Various methods for efficient tracking of these low-rank approximation has been investigated by[60–65]. In our application, the Hessian matrix varies with different placement of the sensor. Subspace tracking method can therefore be used to select the optimal placement of sensors. We applied the most basic technique of projection approximation with power method [66], to keep track of the principle subspace as the sensors are moving toward its optimal locations. The method turned out to be efficient enough for our problem.

The structure of this chapter is as follows, in §3.2.1 we present the problem setup, governing equation and numerical methods to solve the forward scalar-transport problem. §3.2.2 introduces the impulse-response matrix, the Hessian matrix and evaluation of its condition number as the criterion to select the optimal system. §3.3 presents the subspace tracking algorithm to find the optimal sensor placement as to minimize the condition number. In §3.4, we introduce a one-dimensional reconstruction problem where the scalar source distribution is only unknown along the streamwise direction. The impulse-response matrix of this smaller problem can be

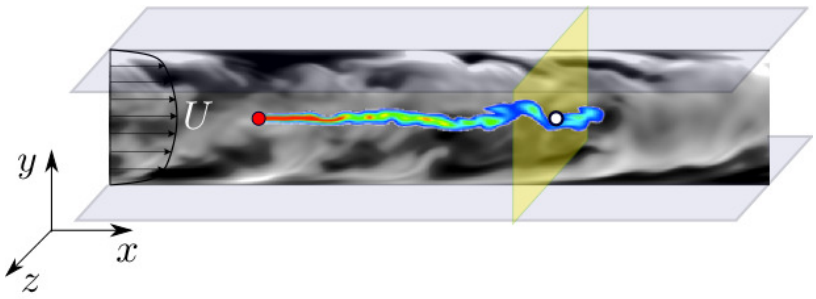

Figure 3-1. A schematic of the rectangular computational domain. Filled and empty circles represent the source and sensor, respectively. The sensors are restricted on a cross-flow plane at $x = 10$.

explicitly calculated and stored by brute force. Therefore, it is used to briefly demonstrate and validate the proposed algorithms, for both one-sensor and multiple-sensor cases. §3.5 considers a three-dimensional reconstruction problem where the scalar source can be anywhere in a confined region within the outer flow region of channel flow. We consider multiple sensor to show the full capability of this approach for optimal sensor placement. §3.6 we include discussion for the possibility of extending the algorithm to finding the optimal weighing of existing sensor network. Improvement of reconstruction quality with fixed error in the measurement is obtained for optimal sensor placement or weighting for all the aforementioned cases.

3.2 Problem Setup

3.2.1 Physical domain & Governing equation

In present study, we focus on a canonical configuration of a fully developed turbulent channel flow, where an isolated sensor or a network of sensors is placed downstream of a steady scalar source. Their measurements are used to reconstruct the spatial distribution of the source. A schematic of the configuration is shown in figure 3-1. In all cases, the sensors were restricted on a cross-flow plane shown in the schematic at $x = 10$. Dimensions of the computational domain in different directions are $L_x = 4\pi h$, $L_y = 2h$ and $L_z = 2\pi h$, where h is half channel height. The flow fields are obtained

by solving the Newtonian incompressible Navier-Stokes equation,

$$\frac{\partial \mathbf{u}}{\partial t} + \mathbf{u} \cdot \nabla \mathbf{u} = -\nabla p + \frac{1}{Re} \nabla^2 \mathbf{u}, \qquad \nabla \cdot \mathbf{u} = 0, \tag{3.1}$$

The Reynolds number here is $Re = \mathcal{U}_b h/\nu = 2800$, normalized by the bulk velocity $\mathcal{U}_b$, channel half height h and the kinematic viscosity ν. The corresponding friction Reynolds number is $Re_\tau \equiv u_\tau h/\nu = 180$, where $u_\tau \equiv \sqrt{\nu \left(d\overline{U}/dy\right)_{wall}}$ is the friction velocity evaluated from the mean wall shear stress, and overbar denotes averaging in the homogeneous spatial directions and in time. Periodic boundary condition is imposed in the both the streamwise (x) and spanwise (z) directions for the flow field, with no-slip conditions in the wall-normal (y) direction at both bottom and top walls. Direct numerical simulations of fully developed turbulent channel flow is performed. The Navier-Stokes equations are solved with a fractional step method with second-order accuracy on a staggered grid. The diffusion term is treated implicitly in time with Crank-Nicolson scheme and the nonlinear convective terms are treated explicitly using Adams-Bashforth scheme. The computational domain is discretized with a Cartesian mesh uniform in streamwise and spanwise directions while a hyperbolic tangent function for grid stretching is used in wall-normal direction to resolve the boundary layer. A thorough parameter study and validation has been performed by Jelly *et al.* [50], who used the same Navier-Stokes solver. We have therefore adopted a Cartesian grid with similar resolution to their study, with uniform grid spacing in both the streamwise and spanwise directions and hyperbolic stretching in the wall-normal coordinate (see table 2-I).

The scalar concentration c is governed by the advection-diffusion equation with a steady source term,

$$\underbrace{\left(\frac{\partial}{\partial t} + \mathbf{u} \cdot \nabla - \frac{1}{Pe} \nabla^2\right)}_{\mathbf{L}} c = \phi(\mathbf{x}), \tag{3.2}$$

where $Pe \equiv ReSc$ is the Péclet number and the Schmidt number was set to $Sc = 0.7$, similar to gas diffusion in air. In the case of a thermal source, Péclet number is

defined as $Pe \equiv RePr$, where Pr is the Prandtl number ($Pr \approx 0.7$ for air). $\phi(\mathbf{x})$ is a steady source distribution as a function of spatial coordinates. $\mathbf{L}$ is a matrix representation of the advection-diffusion operator. Boundary conditions of the scalar include: periodic condition in the spanwise, homogeneous Neumann condition $\frac{\partial c}{\partial n} = 0$ at top and bottom walls, $c = 0$ at the inlet and $\frac{\partial c}{\partial t} + U_b \frac{\partial c}{\partial x} = 0$ at the outlet. To solve the scalar transport equation on top of the stored velocity fields, finite volume method with Adams-Bashforth for the advection, Crank-Nicolson for the diffusion term is used to obtain second-order accuracy in time and space. The source term is treated explicitly.

3.2.2 Impulse-response matrix and the correlation matrix

We briefly recapitulate the idea of unit impulse-response matrix introduced by [14] and apply it to our problem. When the velocity fields are known, the measurement data for a given sensor is linearly dependent on the source distribution $\phi(\mathbf{x})$. From the governing equation,

$$\mathbf{L}\mathbf{c} = \boldsymbol{\phi}(\mathbf{x}), \tag{3.3}$$

we have,

$$\mathbf{c} = \mathbf{L}^{-1}\boldsymbol{\phi}(\mathbf{x}). \tag{3.4}$$

The measurement data for a certain sensor placement can be written as

$$\mathbf{M}(t) = \begin{bmatrix} \mathbf{M}_1(t) \\ \mathbf{M}_2(t) \\ \cdots \\ \mathbf{M}_J(t) \end{bmatrix} = \begin{bmatrix} \mathbf{e}^T(\mathbf{x}_1^m) \\ \mathbf{e}^T(\mathbf{x}_2^m) \\ \cdots \\ \mathbf{e}^T(\mathbf{x}_J^m) \end{bmatrix} \mathbf{L}^{-1}\phi(\mathbf{x}). \tag{3.5}$$

Here $\mathbf{M}_j(t)$ is the measurement data as a function of time at the j^{th} sensor. Their vertical concatenation is denoted as $\mathbf{M}(t)$. The total number of sensors are denoted as J. the vector $\mathbf{e}\left(\mathbf{x}_j^m\right)$ represents a column vector that is unity at the cell $\mathbf{x}_j^m$ and zero elsewhere.

We can write $\boldsymbol{\phi}(\mathbf{x})$ in terms of these impulse functions $\mathbf{e}(\mathbf{x})$,

$$\boldsymbol{\phi}(\mathbf{x}) = \sum_k \mathbf{e}(\mathbf{x}_k)\,\phi(\mathbf{x}_k), \tag{3.6}$$

where the sum is over all grid points in the computational domain. The measurement data can be reformulated as a superposition of measurements from different point sources,

$$\begin{aligned}\mathbf{M}(t) &= \begin{bmatrix}\mathbf{e}^T(\mathbf{x}_1^m)\\ \mathbf{e}^T(\mathbf{x}_2^m)\\ \cdots\\ \mathbf{e}^T(\mathbf{x}_J^m)\end{bmatrix}\mathbf{L}^{-1}\phi(\mathbf{x}). = \begin{bmatrix}\mathbf{e}^T(\mathbf{x}_1^m)\\ \mathbf{e}^T(\mathbf{x}_2^m)\\ \cdots\\ \mathbf{e}^T(\mathbf{x}_J^m)\end{bmatrix}\mathbf{L}^{-1}\sum_k \mathbf{e}(\mathbf{x}_k)\,\phi(\mathbf{x}_k)\\ &= \sum_k \underbrace{\left(\begin{bmatrix}\mathbf{e}^T(\mathbf{x}_1^m)\\ \mathbf{e}^T(\mathbf{x}_2^m)\\ \cdots\\ \mathbf{e}^T(\mathbf{x}_J^m)\end{bmatrix}\mathbf{L}^{-1}\mathbf{e}(\mathbf{x}_k)\right)}_{\mathbf{c}(\mathbf{x}^m,t;\mathbf{x}_k)}\phi(\mathbf{x}_k) = \sum_k \mathbf{c}(\mathbf{x}^m,t;\mathbf{x}_k)\phi(\mathbf{x}_k),\end{aligned} \tag{3.7}$$

where $\mathbf{c}(\mathbf{x}^m,t;\mathbf{x}_k)$ represents the measurement sequence from a point source at $\mathbf{x}_k$. If we write matrix $\mathbf{A}$ as $A_{lk} = c(\mathbf{x}^m,t_l;\mathbf{x}_k)$, then the source-sensor response system can be written simply as,

$$\mathbf{M}(t) = \mathbf{A}\boldsymbol{\phi}(\mathbf{x}). \tag{3.8}$$

The matrix $\mathbf{A}$, in general, is not a square matrix. To solve the system we need to formulate it into an optimization problem to minimize the cost functional, defined as

$$J = \frac{1}{2}\|\mathbf{A}\boldsymbol{\phi}(\mathbf{x}) - \mathbf{M}(t)\|^2, \tag{3.9}$$

and solve the equation

$$\mathbf{A}^T\mathbf{M}(t) = \mathbf{A}^T\mathbf{A}\boldsymbol{\phi}(\mathbf{x}). \tag{3.10}$$

Normally for large systems the above equation can be solved by using the forward and adjoint operator iteratively. An exact transpose operator $\mathbf{A}^T$, generally addressed as "discrete adjoint", is used for the accuracy of the computation. A thorough description and validation of the adjoint code is provided in our previous work [6]. Evaluating

the adjoint field $\mathbf{A}^T\mathbf{M}(t)$ is equivalent as solving the adjoint equation,

$$\mathbf{L}^T\mathbf{c}^\dagger = \sum_{j=1}^{J} \mathbf{M}_j(t)\mathbf{e}(\mathbf{x}_j^m). \tag{3.11}$$

And it has been demonstrated that $\mathbf{A}^T\mathbf{M}(t) = \int_t \mathbf{c}^\dagger(\mathbf{x}, t)$, where the adjoint scalar field $c^\dagger$ is integrated in the assimilation window, as a result of the steady source assumption.

The matrix we attempt to invert here is the correlation matrix $\mathbf{A}^T\mathbf{A} = \mathbf{H} = \mathbf{H}\Big|_{\mathbf{x}^m}$, which is a function of sensor placement $\mathbf{x}^m$. It can be shown that the matrix $\mathbf{H}$ is the Hessian matrix of the cost functional 3.9,

$$\frac{\partial J}{\partial \boldsymbol{\phi}\partial \boldsymbol{\phi}} = \mathbf{A}^T\mathbf{A} = \mathbf{H}. \tag{3.12}$$

The Hessian matrix is $K \times K$, symmetric and semi-positive definite, with K being the number of grid points in the search domain. Also notice that for multiple sensors, the impulse-response matrix will be a simple concatenation from individual sensors. As a result, the corresponding correlation matrix is simply the summation of correlation matrices for each individual sensor – a result that will be revisited in the following sections. The large size of the matrix in a three-dimensional search problem renders it normally intractable to be constructed explicitly. However, the leading eigenvalues and eigenvectors can be computed, which provides summary about $\mathbf{H}$. Eigen-decomposition yields the following equation,

$$\boldsymbol{\Phi}^T\Big|_{\mathbf{x}^m}\mathbf{H}\Big|_{\mathbf{x}^m}\boldsymbol{\Phi}\Big|_{\mathbf{x}^m} = \boldsymbol{\Lambda}\Big|_{\mathbf{x}^m}. \tag{3.13}$$

Here $\boldsymbol{\Phi} = [\phi_1, \phi_2, \ldots, \phi_q]$ is the subspace formed by the dominant q eigenvectors of $\mathbf{H}$, $\boldsymbol{\Lambda}$ is the diagonal matrix with the corresponding eigenvalues $\lambda_1, \lambda_2, \ldots, \lambda_q$. They are both functions of the sensor placement $\mathbf{x}_j^m$. Since $\mathbf{H}$ is symmetric, we have $\boldsymbol{\Phi}^T\boldsymbol{\Phi} = \mathbf{I}_q$.

Normally, the level of ill-posedness, or the difficulty to invert a matrix system can be estimated by the condition number $\kappa = \|\mathbf{H}\|_2\|\mathbf{H}^{-1}\|_2 = \lambda_1/\lambda_K$. It also represents

the maximum possible ratio between relative discrepancy in the reconstruction and discrepancy in the measurement data,

$$\kappa = \max \frac{||\delta\phi||^2/||\phi||^2}{||\delta\mathbf{M}||^2/||\mathbf{M}||^2} \tag{3.14}$$

As we cannot approach the smallest eigenvalue λ_K, we can use $\kappa_I = \lambda_1/\lambda_I$ as an indicator when we are not provided with enough information of the matrix. If we choose I to be large enough, κ_I can predict the trend of the spectrum for different sensor placements accurately.

3.3 Subspace tracking algorithm

The objective of the algorithm is to minimize κ_I and find the optimal placement $\mathbf{x}^m$,

$$(\mathbf{x}^m)^{opt} = arg\min_{\mathbf{x}^m} \frac{\lambda_1}{\lambda_I}. \tag{3.15}$$

In order to circumvent the expensive computational cost of eigen decomposition of $\mathbf{H}$ for every sensor placement, we introduce an algorithm which tracks the subspace $\mathbf{\Phi}$, consisting of the q leading eigenvectors of the Hessian, and use it to estimate the eigenvalues as the sensor placement is updated. Larger subspace, or larger q provides better accuracy when we estimate condition numbers in the algorithm at an expense of larger computational cost. An intrinsic requirement is $q > I + 1$ in order to be able to estimate κ_I from the subspace.

The algorithm contains two steps in every iteration: For the initial sensor placement (iteration index $n = 0$), the subspace is obtained from Arnoldi iterations using the FORTRAN library ARPACK [67], which takes the majority of the computational cost. When the sensors are updated from the old arrangement $(\mathbf{x}^m)^{(n-1)}$ to a new placement $(\mathbf{x}^m)^{(n)}$, the corresponding updated subspace $\mathbf{\Phi}\Big|_{(\mathbf{x}^m)^{(n)}} = \mathbf{\Phi}_n$ need to be evaluated from the old subspace $\mathbf{\Phi}\Big|_{(\mathbf{x}^m)^{(n-1)}} = \mathbf{\Phi}_{n-1}$. Secondly, the estimated $\mathbf{\Phi}_n$ can

be used to evaluate an approximation of $\lambda_1, \lambda_2, \ldots, \lambda_q$ as a function of $\mathbf{x}^m$, and used to adjust new sensor locations. The two steps are detailed in the following subsections.

3.3.1 Subspace iteration

When the sensor placement is adjusted from $(\mathbf{x}^m)^{(n-1)}$ to $(\mathbf{x}^m)^{(n)}$, the Hessian matrix changes from $\mathbf{H}_{n-1}$ to $\mathbf{H}_n$, and the subspace from $\mathbf{\Phi}_{n-1}$ to $\mathbf{\Phi}_n$. To obtain $\mathbf{\Phi}_n$, we can use $\mathbf{\Phi}_{n-1}$ as initial guess and perform subspace iteration using the matrix $\mathbf{H}_n$, which results in the procedures shown below.

Firstly, the subspace from previous sensor placement is hold as the initial guess for $\mathbf{\Phi}_n$

$$\mathbf{\Phi}'_n \leftarrow \mathbf{\Phi}_{n-1}. \tag{3.16}$$

Forward-Adjoint simulations are then performed with column vectors of $\mathbf{\Phi}'_n$ as source terms,

$$\mathbf{W} \leftarrow \mathbf{H}_n \mathbf{\Phi}'_n = \mathbf{A}_n^T \mathbf{A}_n \mathbf{\Phi}'_n. \tag{3.17}$$

For every column vector of $\mathbf{\Phi}'_n$, denoted as $\boldsymbol{\phi}'_{n,l},\ l = 1, 2, \ldots, q$, the corresponding column vector of $\mathbf{W}$, namely $\mathbf{w}_l$ can be obtained by solving the following forward and adjoint equations,

$$\mathbf{c}_l = \mathbf{L}^{-1} \boldsymbol{\phi}'_{n,l}, \quad \mathbf{m}_l(t) = \begin{bmatrix} \mathbf{m}_{l,1}(t) \\ \mathbf{m}_{l,2}(t) \\ \cdots \\ \mathbf{m}_{l,N}(t) \end{bmatrix} = \begin{bmatrix} \mathbf{e}^T\left(\mathbf{x}_1^m\right) \\ \mathbf{e}^T\left(\mathbf{x}_2^m\right) \\ \cdots \\ \mathbf{e}^T\left(\mathbf{x}_N^m\right) \end{bmatrix} \mathbf{c}_l. \tag{3.18}$$

and

$$\mathbf{c}_l^\dagger = \mathbf{L}^{-T} \sum_{j=1}^{N} \mathbf{m}_{l,j} \mathbf{e}\left(\mathbf{x}_j^m\right), \quad \mathbf{w}_l = \int_t \mathbf{c}^\dagger(\mathbf{x}, t). \tag{3.19}$$

Gram-Schmidt orthonormalization (QR factorization) for $\mathbf{w}_l,\ l = 1, 2, \ldots q$ yields,

$$\mathbf{W} = \mathbf{Q}\mathbf{R}^{-1} \tag{3.20}$$

The unitary matrix $\mathbf{Q}$ contains our updated estimate of the eigenvectors,

$$\mathbf{\Phi}'_n \leftarrow \mathbf{Q} \tag{3.21}$$

Once an estimation of $\mathbf{\Phi}'_n$ is obtained, we can repeat equation 3.17 – 3.21 and the estimated $\mathbf{\Phi}'$ will approach the true $\mathbf{\Phi}_n$ after several iterations. This procedure is the same as a standard subspace iteration [68] and the convergence rate is related to the separation between two adjacent eigenvalues, λ_q/λ_{q+1}. Throughout this work, we benefit from the fact that the shape of the eigenvectors do not change significantly for small shifts in the sensor locations. Therefore, performing the above subspace iteration once for every new sensor placement is enough for the current problem.

3.3.2 Estimation of eigenvalues

Once we have computed $\mathbf{\Phi}_n$, it can be used to estimate the eigenvalues for nearby sensor placements. For a general system $\mathbf{H}\Big|_{\mathbf{x}^m}$, equation 3.13 yields the results from eigen decomposition. However, it is intractable to evaluate $\mathbf{\Phi}\Big|_{\mathbf{x}^m}$ everywhere and it is economical to use $\mathbf{\Phi}_n = \mathbf{\Phi}\Big|_{(\mathbf{x}^m)^{(n)}}$ for evaluation of eigenvalues associated with sensor arrangements in the vicinity of $(\mathbf{x}^m)^{(n)}$. By substituting this subspace into a eigen-value decomposition form, it yields,

$$\mathbf{\Phi}_n^T \mathbf{H}\Big|_{\mathbf{x}^m} \mathbf{\Phi}_n = \mathbf{\Gamma}\Big|_{\mathbf{x}^m}. \tag{3.22}$$

Matrix $\mathbf{\Gamma}$ can be easily evaluated for every $\mathbf{x}^m$. In fact, if we regard the eigenvectors in $\mathbf{\Phi}_n$, namely $\boldsymbol{\phi}_{n,1}, \boldsymbol{\phi}_{n,2}, \ldots, \boldsymbol{\phi}_{n,q}$ as scalar sources and perform forward simulations with them, every element of $\mathbf{\Gamma}$ can be written as,

$$\begin{aligned} \Gamma_{jk} &= \boldsymbol{\phi}_{n,j}^T \mathbf{H} \boldsymbol{\phi}_{n,k} \\ &= \boldsymbol{\phi}_{n,j}^T \mathbf{A}^T \mathbf{A} \boldsymbol{\phi}_{n,k} \\ &= \left(\mathbf{A}\boldsymbol{\phi}_{n,j}\right)^T \mathbf{A}\boldsymbol{\phi}_{n,k}, \end{aligned} \tag{3.23}$$

which is the vector inner product of measurement data from different eigen-sources. By simultaneous forward simulations starting from sources $\boldsymbol{\phi}_{n,l}$, $l = 1, 2, \ldots, q$, measurement sequences at various $\mathbf{x}^m$ can be recorded and used to evaluate $\mathbf{\Gamma}$ for all possible nearby sensor placements. We denote the eigenvalues of matrix $\mathbf{\Gamma}$ as $\gamma_1, \gamma_2, \ldots, \gamma_q$ and use them as an estimate of $\lambda_1, \lambda_2, \ldots, \lambda_q$. Notice that if the subspace $\mathbf{\Phi}_n$ is close

approximation of the leading subspace of $\mathbf{H}(\mathbf{x}^m)$ for a generic measurement placement $\mathbf{x}^m$, using q or $q-1$ leading eigen vectors to estimate its I-th eigenvalue, or the condition number $\kappa_I = \lambda_1/\lambda_I$ does not yield significant difference. On the other hand, the level of trust we have for the estimated eigenvalues can be determined by quantifying the difference between the results obtained from using q and $q-1$ leading vectors in $\mathbf{\Phi}_n$. Therefore, we quantify the error of this estimation using the following empirical formula,

$$\epsilon_I = \frac{|\gamma_{1,q}/\gamma_{I,q} - \lambda_1/\lambda_I|}{\lambda_1/\lambda_I} \approx \frac{|\gamma_{1,q}/\gamma_{I,q} - \gamma_{1,q-1}/\gamma_{I,q-1}|}{\gamma_{1,q}/\gamma_{I,q}} = \tilde{\epsilon}_I, \tag{3.24}$$

where $\gamma_{i,q-1}$ are the i-th eigenvalue of the matrix $\mathbf{\Gamma}(1:q-1, 1:q-1)$, a truncation of the matrix $\mathbf{\Gamma}$ to ignore its last row and column. This allows us to estimate the error without knowing the true λ_i. A threshold value E is then chosen for $\tilde{\epsilon}_i$ and the sensor placement update is constrained to be within the trust region $\Omega = \{\mathbf{x}^m | \tilde{\epsilon}_i < E\}$.

The final algorithm is summarized as the procedure in algorithm 2.

Algorithm 2: Subspace tracking algorithm for evaluation of optimal sensor placement.

- $n = 0$;
- Prescribe an initial placement of the sensor $(\mathbf{x}^m)^{(0)}$;
- Choose the index I and the size of the subspace, $q > I + 1$;
- Perform Arnoldi iterations using forward-adjoint loops to compute the starting subspace $\mathbf{\Phi}_0$ and the corresponding eigenvalues of the Hessian matrix;

while *Convergence condition is not satisfied* **do**

- Perform forward simulations using estimated eigenvectors in $\mathbf{\Phi}_n$ and store measurement data. Use equation 3.23 to evaluate matrix $\mathbf{\Gamma}$ for nearby sensor placements;
- Evaluate the estimate error $\tilde{\epsilon}$ from equation 3.24;
- Establish the trust region $\Omega = \{\mathbf{x}^m | \tilde{\epsilon}_i < E\}$ and move sensor to $(\mathbf{x}^m)^{(n+1)} = arg \max_{\mathbf{x}^m \epsilon \Omega} \gamma_1/\gamma_I$.;
- Perform adjoint simulations by solving equation 3.19 for the new sensor locations $(\mathbf{x}^m)^{(n+1)}$.;
- Obtain estimated subspace $\mathbf{\Phi}_{n+1}$ for the new sensor placement using equations 3.17 – 3.21.;
- $n = n + 1$

end

3.4 One-dimensional source reconstruction

In most scenarios, explicitly building the impulse-response matrix **A** is practical, since the number of possible source locations is equal to the number of grid points in the search domain, which is generally a huge number in three-dimensional cases. However, if the search domain is confined to include only a limited number of grid points, it becomes possible to compute and store the impulse-response system by brute force. Studies have shown that reconstructing the source in the streamwise direction is the most difficult compared to y and z directions [6]. Therefore, in our first step, we restrict our focus in the stream-wise direction and perform source reconstruction only as a function of x. As shown in figure 3-2, we assumed that the y and z locations of the source is already known, and the source only exists along the center line from $x_B = 1$ to $x_E = 9$, denoting the starting and ending points of the search region. A series of forward simulations were performed from every possible sources along the line while measurement data were recorded in the cross-flow plane located at $x^m = 10$. The recording procedure includes $t = 100h/U_b$ convective time units that excludes the transit time when measurements are influenced by the initiation of the source. A total number of 245 forward simulations were performed in order to obtain all the systems, each starting from an impulse on a single grid point. Through these forward simulations, the impulse-response matrices for every possible combination of the sensors on the plane can be easily obtained. This system for one-dimensional reconstruction enables us to have full understanding of the optimal sensor placement in the most challenging direction for source localization and helps to validate the algorithm before we approach more complicated scenarios.

3.4.1 Optimal placement for a single sensor

When only one sensor is available, we can map out the condition number κ_I over different possible locations of the sensor on the $y-z$ plane after building the Hessian

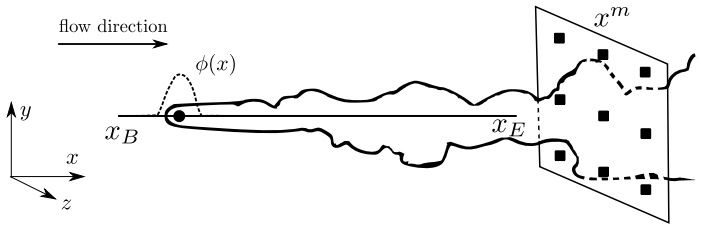

Figure 3-2. Schematic for the one-dimensional source reconstruction problem.

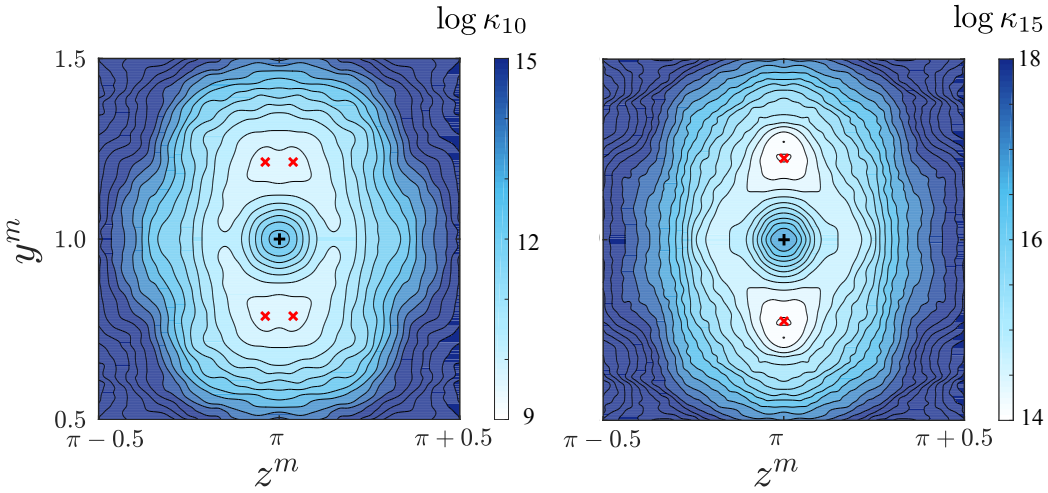

Figure 3-3. Contour of $\log(\lambda_1/\lambda_{10})$ (left) and $\log(\lambda_1/\lambda_{15})$ (right) for different sensor locations on the cross-flow plane at $x = 10$. The domain of search here is the channel centerline from $x = 1$ to $x = 9$.

matrices $\mathbf{H}$ for every possible sensor location. The contour plot in figure 3-3 shows κ_{10} and κ_{15} for different sensors on the plane. In the channel center case, although different index I give slightly different results, they point out the optimal sensor locations at roughly the same distance from the center. Thus the naive placement of a single sensor directly downstream of the search region is not the best option.

The difference between a sensor directly downstream and at the optimal location in terms of the leading eigenvalues and eigenvectors is shown in figure 3-4. The spectrum decays quickly in log scale, representing a heavily dampened system and thus the ill-posed nature of the source reconstruction problem. By moving the sensor from the center to the optimal location, we successfully decrease κ_{15} by 90% and the whole spectrum is shifted upwards. All the leading eigenvectors for the optimal sensor

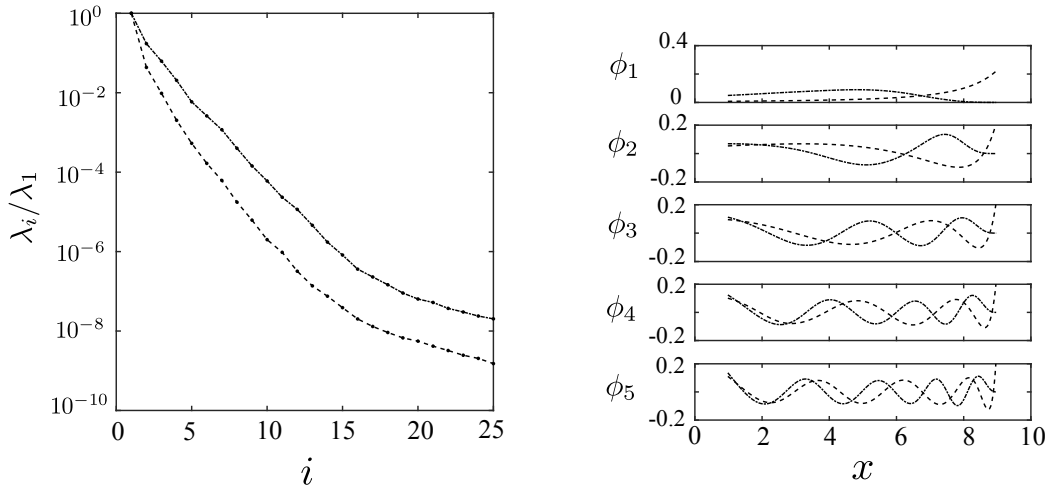

Figure 3-4. The leading eigenvalues (left) and eigenvectors (right) of the Hessian matrix P for a sensor located directly downstream of the source (dashed line) versus at the optimal location found by minimizing λ_1/λ_{15} (dash-dotted line).

are more oscillatory. This is an essential phenomenon to explain the improvement of source reconstruction using the optimal sensor. If we calculate the projection of a source localized at x^s onto the eigenvectors in figure 3-4, the coefficient as a result of the projection would change if x^s is shifted. For a more oscillatory eigenvector, the change of the projection would change even more, implying an enhanced ability to differentiated nearby sources. Therefore, the leading eigenvectors using the optimal sensor provide a better potentiality to differentiate different source distributions, and thus provide better source reconstruction. Another important observation from these eigenvectors is that reconstructing a source farther away from the sensor is much harder than reconstructing nearer sources, as the eigenvectors become smoother away from the sensor.

In order to further quantify the superiority of the optimal sensor over the one directly downstream, we reconstruct scalar sources at various locations x^s with sensors at different locations and compare the quality of the prediction. A well-resolved one-dimensional kernel of the localized sources that vanishes outside a short range is

incorporated and the true source can be expressed as,

$$\phi_T(x;x^s) = \frac{1}{4\rho_0}\left[\cos\left(\frac{\pi|\mathbf{x}-\mathbf{x}^s|}{\rho_0}\right)+1\right]\Big[\,\mathrm{sign}(\rho_0-|\mathbf{x}-\mathbf{x}^s|)+1\Big]. \tag{3.25}$$

This profile integrates to unity and its width can be controlled by adjusting the value of ρ_0, here chosen to be 0.2. Measurement can be generated through equation 3.10. Initial guess of the source is zero everywhere. Conjugate gradient method is then used to reconstruct the source distribution by minimizing the following cost functional,

$$J = \frac{1}{2}||\mathbf{A}\phi-\mathbf{M}||^2 = \frac{1}{2}||\mathbf{A}\phi-\mathbf{A}\phi_T||^2 \tag{3.26}$$

The cost functional represents the discrepancy between estimated measurement and the true output. The stopping criterion for our conjugate-gradient iterations is set to be,

$$\frac{J}{J_0} = \frac{||\mathbf{A}\phi-\mathbf{M}||^2}{||\mathbf{M}||^2} \le 0.001, \tag{3.27}$$

where J_0 is the value of cost function for the initial guess. By this criterion we are fixing the relative discrepancy in the measurement in equation 3.14 and address the ability to accurately estimate the source. For large-dimension problems, the conjugate gradient method would be formulated in the manner of iterative forward-adjoint loops and requires a lot of computational resource [5, 6, 24]. However, for the one-dimensional search in current section, we benefit from the storage of impulse-reponse matrices A and could directly apply the matrix-vector multiplication for the source reconstruction. Three-dimensional search problems that actually incorporate the adjoint-looping algorithm will be conducted and discussed in section §3.5.

Sample reconstruction of the source are shown in figure 3-5, where the improvement of prediction accuracy using the optimal sensor is apparent especially for sources near the sensor.

Furthermore, the reconstruction quality can be characterized by the correlation coefficient,

$$R_{\phi\phi} = \frac{\int_V \phi\phi_T dV}{\phi_{rms}\phi_{T,rms}}, \tag{3.28}$$

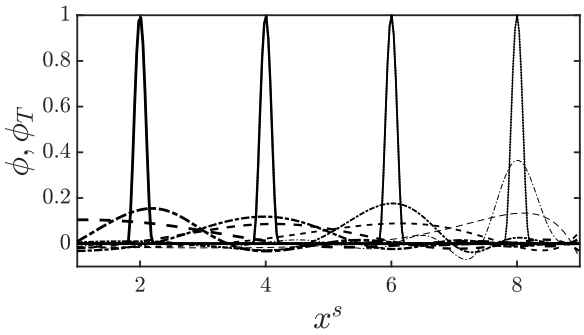

Figure 3-5. Sample reconstruction of sources located at different x^s along the channel centerline. Dashed line shows the results using one sensor at the channel center, dash-dotted line shows that with the sensor at the optimal location found by minimizing λ_1/λ_{15}.

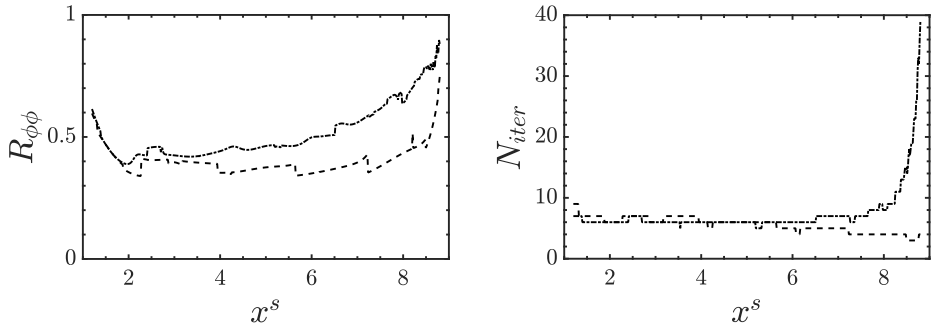

Figure 3-6. Left: Reconstruction quality of sources located at x^s along the channel centerline. Dashed line shows the results using one sensor at the channel center, dash-dotted line shows that with the sensor at the optimal location found by minimizing λ_1/λ_{15}. Right: The number of iterations required to drive the cost functional to the converge criterion.

where the subscript V represent the computational domain. The rms values are defined by,

$$\phi_{rms} = \sqrt{\int_V \phi^2(\mathbf{x}) dV}. \tag{3.29}$$

Comparison of reconstruction quality for both sensors are plotted in figure 3-6. Numbers of conjugate gradient iterations for each reconstruction are also included.

A universal improvement of reconstruction quality for all possible x^s is obtained if the optimal sensor is used. However, for a near source, the optimal sensor requirements much more iterations than a sensor directly downstream. This can be explained by the shape of leading eigenvectors in figure 3-4. For the optimal sensor, the leading eigenvectors become very small close to the sensor plane, meaning a loss

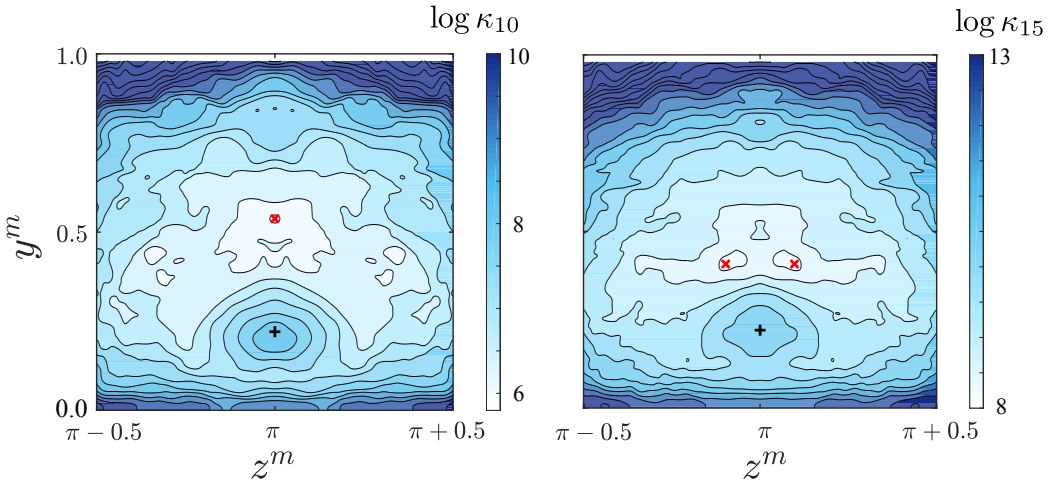

Figure 3-7. Contour of $\log(\lambda_1/\lambda_{10})$ (left) and $\log(\lambda_1/\lambda_{15})$ (right) for different sensor locations on the cross-flow plane at $x = 10$. The domain of search here is a streamwise line from $x_B = 1$ to $x_E = 9$ at the log layer $y^+ = 40$.

of sensitivity for the principle subspace to represent a near source. It is worth noticing that while the optimal sensor is optimal for detecting a source that can be anywhere within the search domain, it is not necessarily optimal for every source location x^s. As in the current case, the optimal sensor trades the ability to detect near sources for an enhanced ability to differentiate farther sources. The fact that it requires 40 iterations for the near source, is mainly due to the limitation of the efficiency of the algorithm to decrease the cost functional.

If the search domain is the same streamwise range but in the middle of log layer with $y^+ = 40$, we can perform the same procedure of recording forward simulations and construct the Hessian matrix $\mathbf{H}$ for each sensor location. The condition number κ_{10} and κ_{15} are plotted in figure 3-7.

Notice that for the log-layer case, the optimal sensor is shifted up from the log layer. Comparison of reconstruction quality if shown in figure 3-8.

To understand the different characteristics of the naive and optimal placed sensor, we plot the mean scalar field and the streamwise decay rate of the mean scalar field from steady sources in figure 3-9. The contour of mean scalar field represent the "mean signal intensity" for hypothetical sensor locations. The streamwise decay rate

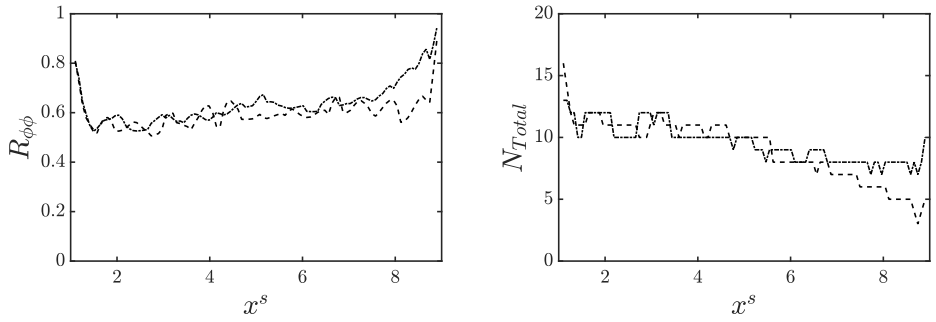

Figure 3-8. Left: Reconstruction quality of sources located at x^s along the log layer ($y^+ = 40$). Dashed line shows the results using one sensor at the channel center, dash-dotted line shows that with the sensor at the optimal location found by minimizing λ_1/λ_{15}. Right: The number of iterations required to drive the cost functional to the converge criterion.

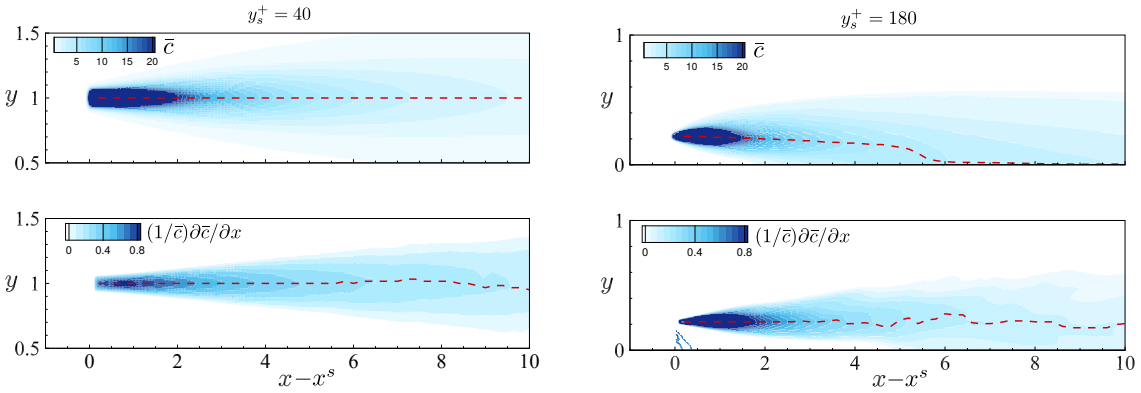

Figure 3-9. Mean scalar field (top) and streamwise decay rate (bottom) for steady sources release at channel center (left) and log layer (right).

represent the relative change of mean signal intensity if the source is shifted slightly in the streamwise direction. In previous applications, optimal sensor placements are usually selected based on maximum sensitivity [27] or maximum change of signal intensity due to a perturbation in the control vector [29]. These approaches correspond to putting sensor at the local maxima of the top or bottom contours in figure 3-9. However, the maximum signal intensity or decay rate of signal intensity remain directly downstream of the source for the channel center case. In the log-layer case, the maxima of decay rate of signal intensity is directly downstream of the source, which is not the optimal location of the sensor placement. The maxima of the signal intensity move closer to the wall, which shows even worse condition number from figure 3-7.

These results shows clear evidence that the optimal sensor placement is not due to either maximum sensitivity nor to the difference of sensitivity to nearby sources. For any given sensor, it is essential that the signal from two nearby sources can be differentiated. Equivalently, when a source is shifted in the streamwise direction, the sensor signal should exhibit enough difference to represent such shift.

To further investigate why the reconstruction quality is improved for the optimal sensor location, we evaluate and compare the "shifting-source correlation coefficient" for different sensors. The "shifting-source correlation coefficient" selects a reference source x^s and shift the source location by the amount of Δx^s. The correlation coefficient between measurements from the reference and the shifted sources is then evaluated and used as a measure of the ability for sensors to differ nearby source locations.

$$R^s_{MM}(\Delta x^s, \Delta t^m; D) = \frac{\overline{c(\mathbf{x}^m, t; \mathbf{x}^s) c\left(\mathbf{x}^m, t + \Delta t^m; \mathbf{x}^s + \Delta x^s \mathbf{e}_x\right)}^{\langle t \rangle}}{c_{rms}(\mathbf{x}^m, t; \mathbf{x}^s)\, c_{rms}\left(\mathbf{x}^m, t + \Delta t^m; \mathbf{x}^s + \Delta x^s \mathbf{e}_x\right)}, \tag{3.30}$$

where the overline represents average in time and $D = x^m - x^s$ is the streamwise distance between the reference source and the sensor. The shifting-source correlation coefficients for different Ds and different sensors (naive and optimized ones) are shown in figure 3-10. In both channel center and log layer cases, the optimal sen-

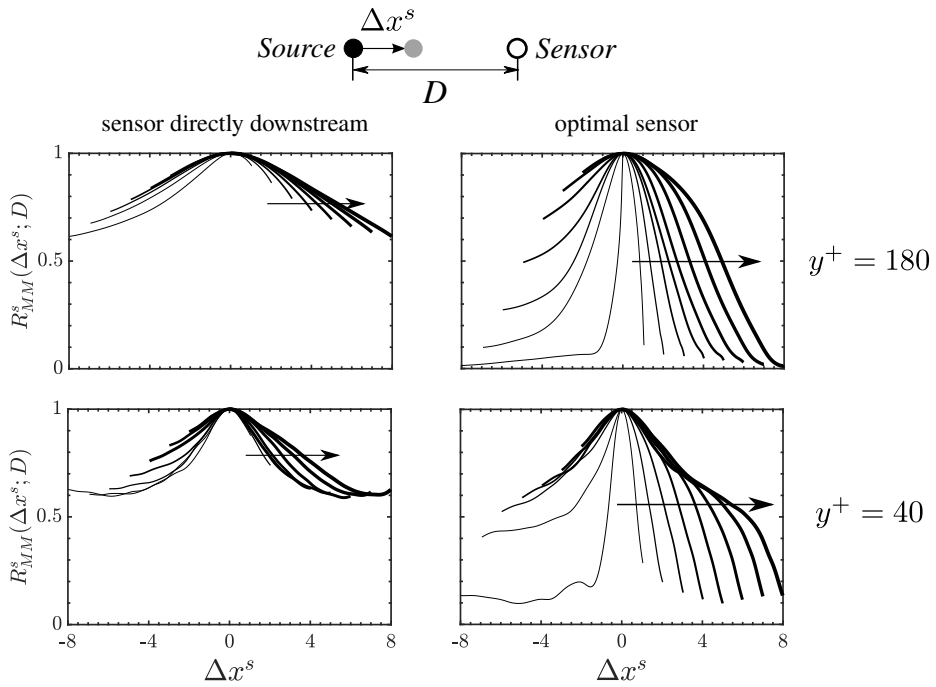

Figure 3-10. Shifting-source correlation coefficient for sensor placed directly downstream of the source (left) and at the optimal location determined by minimizing κ_{15} (right). Thicker lines marks larger distance between the sensor and the reference source, D. Arrow also shows this trend.

sors yield a much better ability to differentiate adjacent sources, represented by a quickly-decaying shifting-source correlation coefficient. It can also be observed that the correlation of nearby sources is much lower in the log layer than in the channel center, therefore, the reconstruction in log layer is more accurate – a result agreed with previous findings [6].

Furthermore, different roles of physical mechanisms has been investigated in the process of scalar transport from a localized source, especially the dispersion by turbulent fluctuation and molecular diffusion, as terms of the governing equation for the mean scalar "energy" $\overline{c^2}$,

$$0 = \frac{\partial \overline{c^2}}{\partial t} = \underbrace{-U\frac{\partial \overline{c^2}}{\partial x}}_{\mathcal{A}} \underbrace{-\nabla\cdot\overline{\mathbf{u}'c^2}}_{\mathcal{D}} + \underbrace{\frac{1}{Pe}\nabla^2\overline{c^2}}_{\mathcal{M}} \underbrace{-\frac{2}{Pe}\left(\overline{\nabla c\cdot\nabla c}\right)}_{\mathcal{E}}. \tag{3.31}$$

where the streamwise decay of $\overline{c^2}$ is balanced by the turbulent dispersion ($\mathcal{D}$), molecular diffusion ($\mathcal{M}$) and dissipation ($\mathcal{E}$). Figure 3-11 shows the y-profile of $\mathcal{D}$ and $\mathcal{M}$

for channel center and log layer cases. These statistics are collected within a time horizon of $t\mathcal{U}_b/h = 2000$ with an initial 200 convective time units to clear the transient. We also utilized the homogeneity in z direction and averaged 9 point sources placed at different spanwise locations. The dash-dotted lines show the y-location of the optimal sensor location. We should bear in mind that the optimal sensor location is for reconstructing a source that could be anywhere within in the search region, namely $D \in [1, 9]$. By looking at the physical mechanism for a point source, however, we aim at analyzing the effect of optimal sensor on detecting an isolated source at a specific location, where the statistics should still be instructive. In the channel center, the turbulent dispersion and molecular diffusion have similar shape of profiles and they both change sign near the edge of the plume, where the optimal sensor location lies. Similar trend appear in the log layer case as well and both terms change sign near the optimal sensor location. The sign change of turbulent dispersion and molecular diffusion reveals where we are in the field and marks the location to take informative measurements. We can also observe that the dispersion term in log layer is much more important compared with the molecular diffusion, a trend that is less prominent in the channel center. Since turbulent dispersion is a reversible process and molecular diffusion is irreversible, it is presumed that the molecular diffusion would jeopardize the ability to trace back to the source location. In fact, measurement signals from different sources can be blurred due to the effect of diffusion and become difficult to differentiate. Therefore, the dominating role of turbulent dispersion in the log layer explained the much better reconstruction results compared with the channel center cases. These results are consistent with our previous findings [6] and justify the reason to avoid putting measurements inside the buffer layer, where the effect of diffusion is much more pronounced and causing the condition number of the system to rise up in figure 3-7.

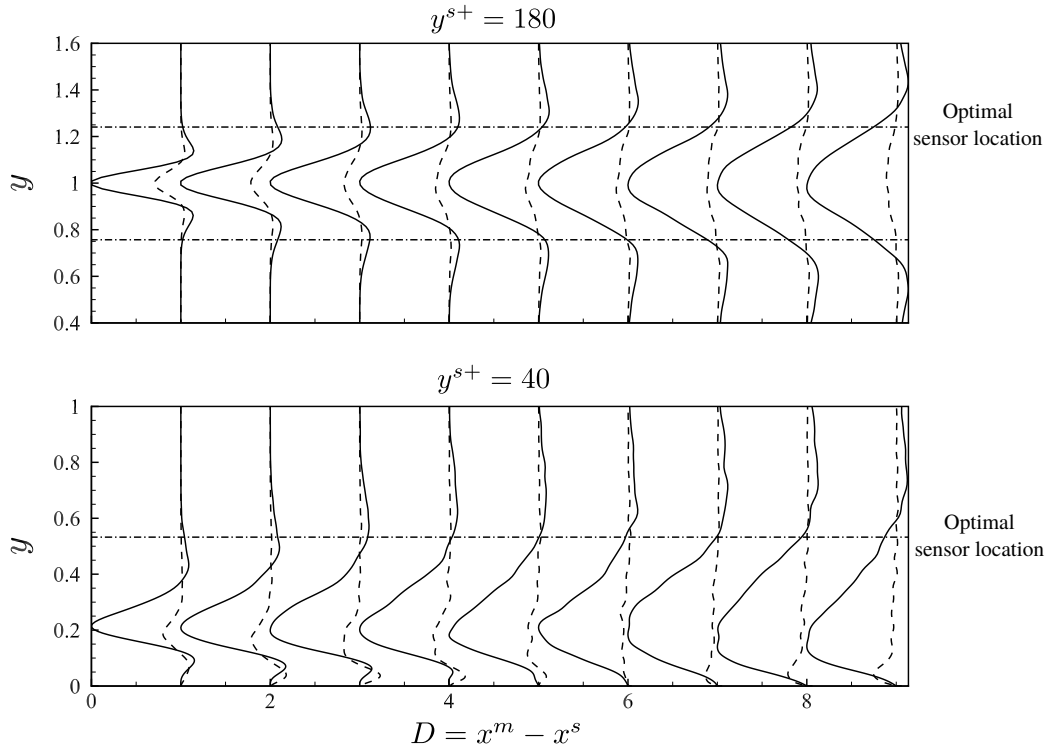

Figure 3-11. Profile of normalized turbulent dispersion $\mathcal{D}/\mathcal{D}_{max}$ (solid lines) and molecular diffusion $\mathcal{M}/\mathcal{D}_{max}$ (dashed lines) in y direction. The profiles are horizontally shifted by the distance between source and sensor, $D = x^m - x^s$. Top and bottom figures are cases in the channel center and log layer, respectively. The optimal sensor location are marked by the dash-dotted lines.

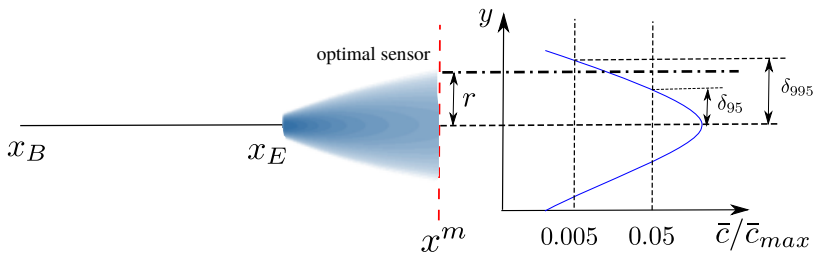

Figure 3-12. Schematic of comparing the optimal location of one sensor to the edge of the plume from the nearest source $x^s = x_E$.

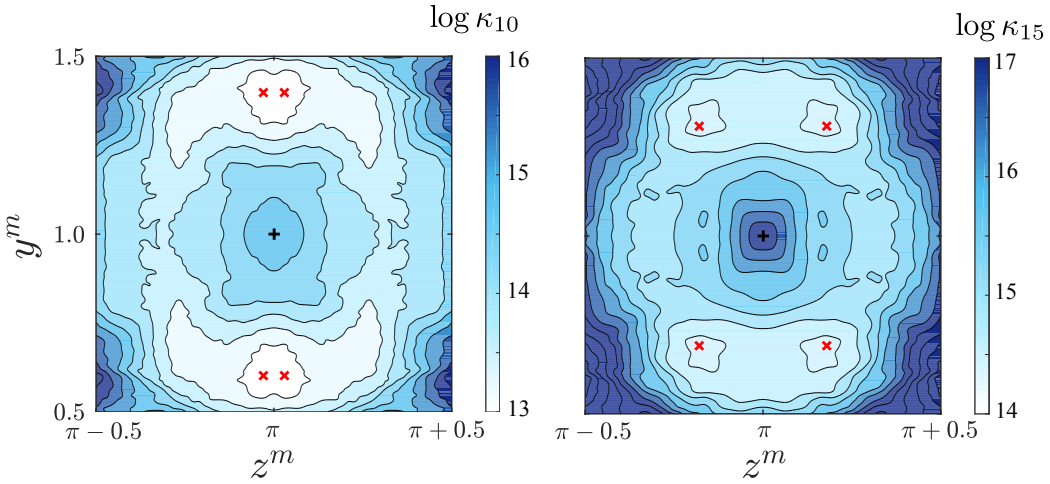

Figure 3-13. Contour of $\log(\lambda_1/\lambda_{10})$ (left) and $\log(\lambda_1/\lambda_{15})$ (right) for different sensor locations on the cross-flow plane at $x = 10$. The domain of search here is the channel centerline from $x_B = 1$ to $x_E = 6$.

3.4.2 Influence of the search domain and eigenvalue index on the optimal sensor location

The optimal sensor location is spotted near the plume edges for the point sources inside the domain of search. Presumably, the location of the optimal sensor depends on the domain of search according to the plume edges from sources inside the domain. If we decrease the end point of the search domain to $x_E = 6$ in figure 3-2, the optimal sensor location moves further away from the center, as shown in figure 3-13.

We are particularly interested in the comparison between the optimal sensor location and the edge of the plume from the nearest source, as shown in the schematic in figure 3-12. Location of the optimal sensor is characterized by its distance r from the point directly downstream on the sensor plane $x^m = 10$. As can be seen from figure

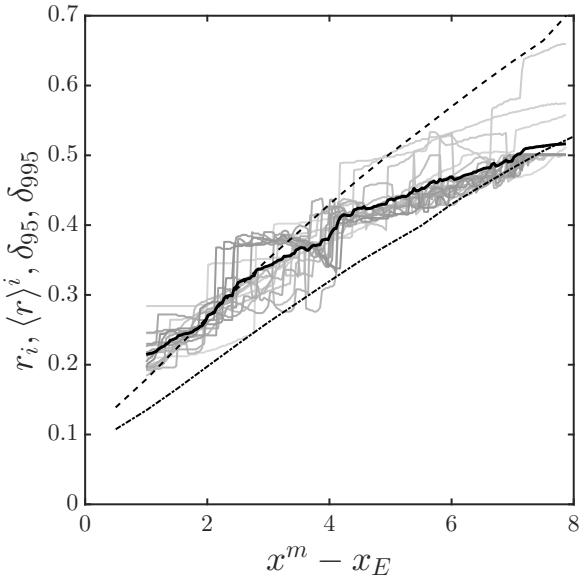

Figure 3-14. Distance r between the optimal sensor location and the channel center by minimizing λ_1/λ_I for different Is. Thicker grey lines represents larger I from 5 to 25. Averaged distance is marked by the solid black line. Comparison with the distance to the edge of the plume are marked by dashed line(δ_{995}) and dash-dotted line(δ_{95}).

3-3, different eigenvalue index I yields slightly different optimal sensor locations. We use r_I to denote the distance from the optimal sensor to the point on the sensor plane and directly downstream of the source. the quantity r_I will accurately quantify the locations of optimal sensors when different I is used to evaluate the condition number.

To access the effect of search domain, we set x_E systematically smaller, as shown in figure 3-14. The plume edges characterized by δ_{95} and δ_{995} , corresponding to 95% and 99.5% drop of the mean profile, are plotted for comparison. The trend of the optimal sensor location seems to follow that of the plume edge from the nearest source, since most of the optimal locations we found were within the region confined by $\delta_{95} \leq r \leq \delta_{995}$. It is consistent with our previous findings that the optimal sensor stays near the edge of the nearest plume, instead of directly downstream. The same trend can be observed even if the source is located in the log layer, as shown in figure 3-15.

While all the previous results are obtained by brute force calculation of the con-

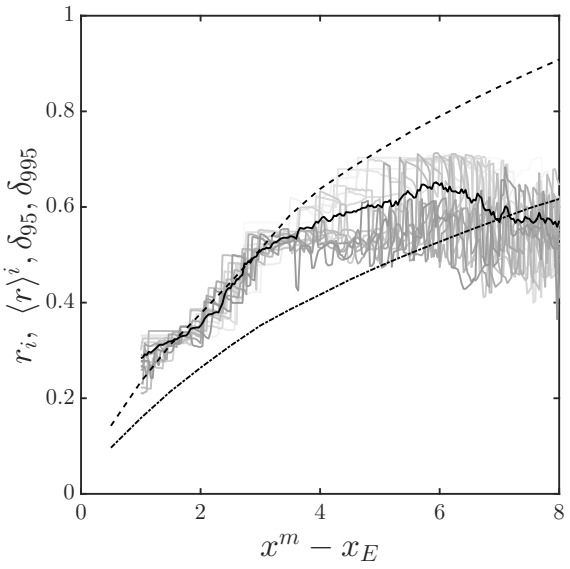

Figure 3-15. Distance r between the optimal sensor location and the channel center by minimizing λ_1/λ_i for different Is. Thicker grey lines represents larger I from 5 to 25. Averaged distance is marked by the solid black line. Comparison with the distance to the edge of the plume are marked by dashed line(δ_{995}) and dash-dotted line(δ_{95}).

dition number κ, we are also interested in the accuracy of our subspace-tracking algorithm in this simple case. We start from a initial placement of the sensor directly downstream and obtain the principle subspace $\mathbf{\Phi}_0$. The size of the subspace here is chosen to be q = 15. Through equation 3.22, matrices $\mathbf{\Gamma}$ can be evaluated for each sensor location. In the subspace-tracking algorithm the condition numbers $\kappa_I = \lambda_1/\lambda_I$ are approximated using γ_1/γ_I, where $\gamma_1, \gamma_2, \ldots \gamma_q$ are eigenvalues for matrix $\mathbf{\Gamma}$. We plot κ_I for every sensor and compare with the true condition number. The comparison for the channel center case is shown in figure 3-16. Notice that the left figure uses brute force to calculate the condition number for each sensor while the right one only uses the subspace for the sensor directly downstream and is much less costly. The results show very good agreement especially near the center and the optimized locations obtains by the subspace-tracking algorithm and by brute force are identical. In this case, the optimal sensor location can be reached with only one iteration. Moreover, we examine the estimated error evaluated by equation 3.24. As shown in

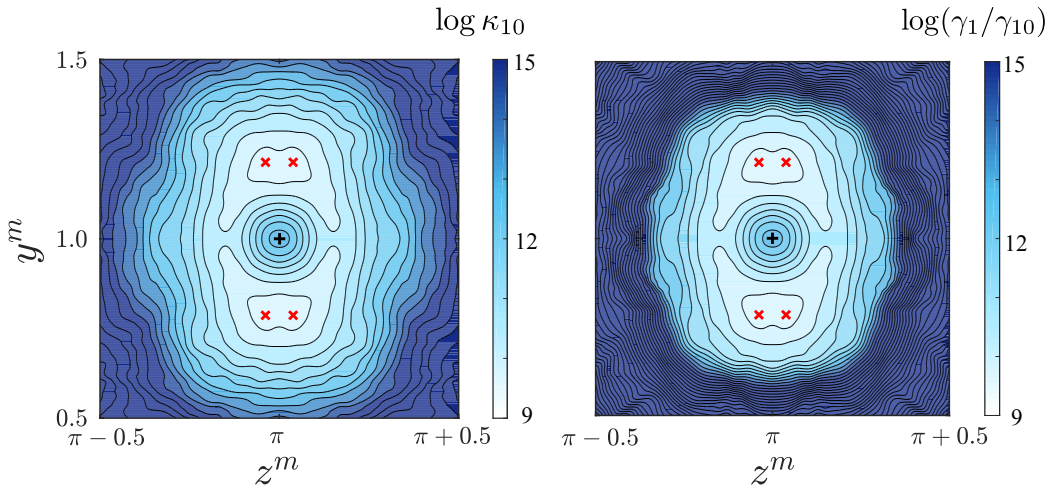

Figure 3-16. Contour of $\log(\lambda_1/\lambda_{10})$ (left) and $\log(\gamma_1/\gamma_{10})$ (right) for different sensor locations on the cross-flow plane at $x = 10$. The domain of search here is the channel centerline from $x = 1$ to $x = 9$.

figure 3-16, On the left-hand side we have the contour of λ_1/λ_{10}, where for every point we calculate λ_i, $i = 1, 10$ by brute force. On the right-hand side we use the subspace $\mathbf{\Phi}_0$ for a sensor at the channel center and use it to calculate γ_i, $i = 1, 2, \ldots, I$ and estimate of κ_{10}. The results are quite similar. The contour of 10% relative difference $\epsilon_{10} = 0.1$ is shown in figure 3-17 as dashed lines. Meanwhile, we use our criterion $\tilde{\epsilon}_{10}$ and plot the contour $\tilde{\epsilon}_{10} = 0.1$, shown as solid line. The criterion $\tilde{\epsilon}_{10}$ matches well with the true ϵ_{10} and thus can be used when knowledge of λ_i cannot be pre-occupied.

3.4.3 Optimal placement for multiple sensors

We then apply this technique to a four-sensor case to reconstruct the source in the channel center as a demonstration when multiple sensors are available.

The correlation matrix $\mathbf{H}$ for a combination of sensors is equal to the summation of individual correlation matrices for each sensor. For multiple-sensor cases, since every possible combination of sensors has to be taken into account, the search space for sensor arrangements becomes too large to deal with brute force. Therefore, the subspace-tracking method becomes necessary in this situation. We still consider the

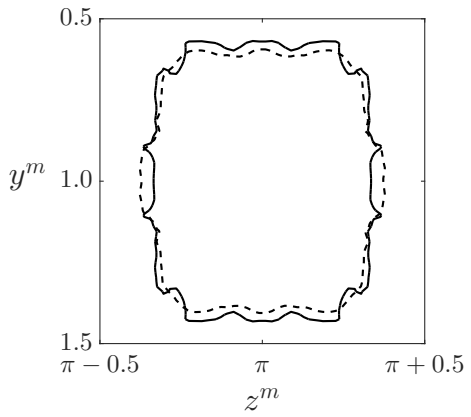

Figure 3-17. Contour line of 10% error calculated by $\epsilon_{10} = \frac{|\gamma_{1,q}/\gamma_{10,q} - \lambda_1/\lambda_{10}|}{\lambda_1/\lambda_{10}}$ (dashed line) and $\tilde{\epsilon}_{10} = \frac{|\gamma_{1,q}/\gamma_{10,q} - \gamma_{1,q-1}/\gamma_{10,q-1}|}{\gamma_{1,q}/\gamma_{10,q}}$ (solid line).

case where the scalar source is known to be in the channel center. The initial sensor placement is shown in figure 3-18 as dark crosses. The placement is far outside the plume edge of the nearest source, as marked by the dashed contours. Therefore, it would be very difficult for the initial sensor to reconstruct a near source since projection of the source onto the principal subspace would be nearly negligible.

The size of the subspace is chosen to be $q = 20$ and we aim at minimizing $\kappa_{15} = \lambda_1/\lambda_{15}$. As shown in figure 3-18, during the subspace-tracking iterations, two of the sensors were moved closer to the plume edge for the nearest source, enhancing our ability to detect a source nearby. As a result, the spectrum of the system is also improved. optimization converges after just two iterations. Reconstruction results are shown in figure 3-19. The initial placement of the sensors are poor to detect a near source and the number of required iteration goes to extreme values (results are shown with maximum 50 conjugate gradient iterations). The optimal sensor placement, on the other hand, obtain much better results for the near source with reasonable number of iterations. Although for the source farther away, the initial placement is still better.

As mentioned before, the formulation of optimal sensor placement takes into ac-

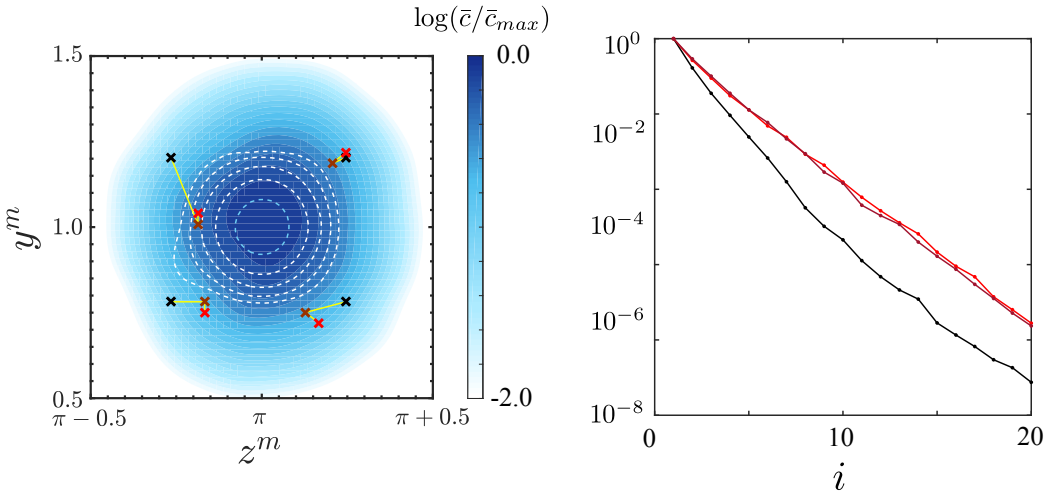

Figure 3-18. Left: traces of four sensors as they move to their optimal placement in the cross-flow plane to place the sensors. Their colors become lighter as more iterations are performed. In the background the mean scalar field $\log(\bar{c}/\bar{c}_{max})$ from the nearest source ($x^s = x_E$) and the farthest source ($x^s = x_B$) are shown by dashed and flood contours, respectively. Right: the corresponding eigen-value spectrum for evolving sensor placements.

count the whole search domain and is not optimal for every source location. In the current case, the algorithm trade the performance of constructing a farther source for better sensitivity of the near sources. The overall reconstruction quality is maintained (the averaged correlation varies from 0.52 to 0.51) with a significant reduce of computational cost (the averaged number of iterations drops from 16 to 8). One would assume that with more sensors, we tend to obtain better results for the source

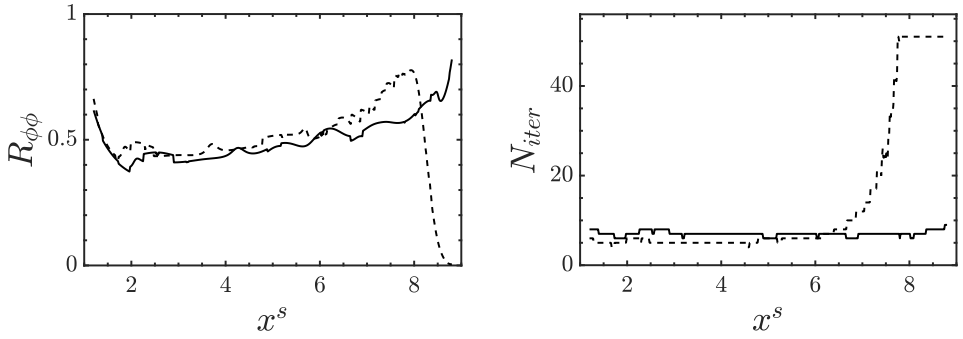

Figure 3-19. Left: Reconstruction quality of sources located at x^s along the channel centerline. Dashed line shows the results using initial sensor placement dash-dotted line shows that with the sensors at the optimal locations found by minimizing λ_1/λ_{15}. Right: The number of iterations required to drive the cost functional to the converge criterion.

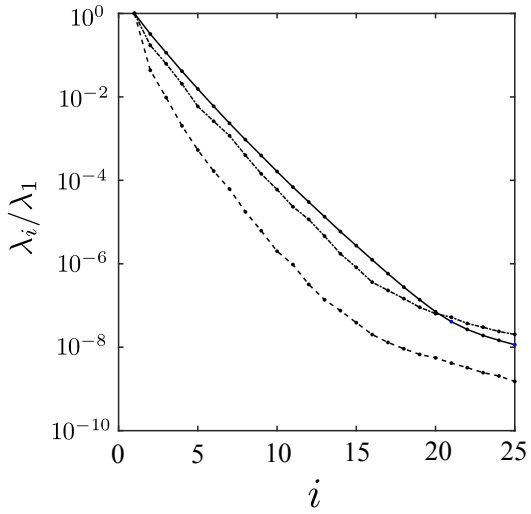

Figure 3-20. Comparison of leading eigenvalues between one sensor directly downstream (dashed line), at the optimal location (dash-dotted line) and using all the sensors in the cross-flow plane (solid line).

reconstruction. This is actually not true, since information using different sensors can easily become redundant. Oftentimes multiple-sensor cases can be dominated by sensors that are not helpful to reconstruct the source unless we apply different weight for these sensors. The limitation of multiple-sensor cases without weighting can be simply demonstrated by using all the sensors on the plane. The resulting spectrum are shown in figure 3-20. Even with all the sensors on the plane, the improvement of the spectrum is very limited and is on the same level with using only one sensor at its optimal location. Based on the comparison of reconstruction quality in figure 3-21 with one-sensor cases. It is hardly conclusive that using all the sensors on the plane greatly outperforms one sensor at its optimal location. Therefore, to further improve the condition of the system, it is necessary to apply different weight for different sensors, which is illustrated more in §3.6.

3.5 Three-dimensional source reconstruction

The condition number minimization combined with the subspace tracking algorithm has been illustrated to be efficient for a one-dimensional search. The algorithm is

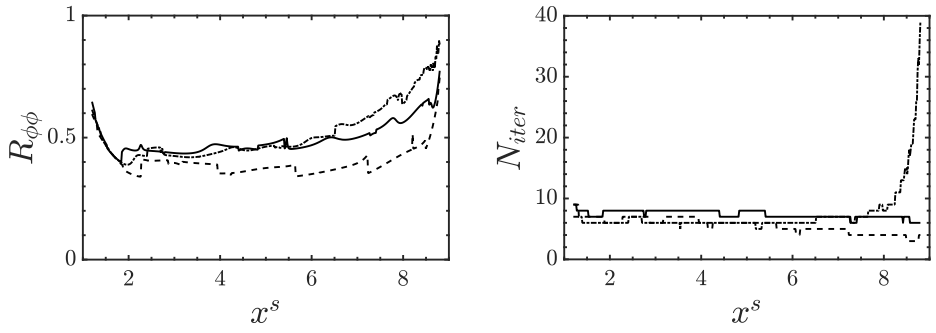

Figure 3-21. Top: Reconstruction quality of sources located at x^s along the channel centerline. Dashed line shows the results using initial sensor placement dash-dotted line shows that with the sensors at the optimal locations found by minimizing λ_1/λ_{15}. Bottom: The number of iterations required to drive the cost functional to the converge criterion.

incorporated here for search within a three-dimensional region using multiple sensors, where the three-dimensional domain of search is set to be the following region,

$$1 \leq x \leq 4, \quad 0.75 \leq y \leq 1.25, \quad \pi - 0.25 \leq z \leq \pi + 0.25, \tag{3.32}$$

while the sensors are located on a cross-flow plane at $x = 7$.

We keep track of the subspace, consisting of $q = 25$ eigen-vectors of the system, and move the sensors on the $y - z$ plane to minimize the condition number of the Hessian matrix $\mathbf{H}(\mathbf{x}^m)$, estimated by $\kappa_{15} = \lambda_1/\lambda_{15}$. The initial sensors are placed all near the center, as shown on the left-hand side of figure 3-22. During the process, it clear shows that the originally nearby sensor were separated from one another by the algorithm and were move away from the center. The corresponding change of the spectrum is plotted on the right-hand side of figure 3-22. As a result, the condition number κ_{15} is improved by a factor of 3.

The iso-contours of some selected eigenvectors for the initial and optimal sensor placements are shown in figure 3-23. The first few eigenvectors (ϕ_1 to ϕ_5) are streaky in x-direction, representing the loss of ability to differentiate sources at different stream-wise locations. The other eigenvectors have bigger fluctuations in x-direction and thus will be more helpful to reconstruct the source in the stream wise direction. While the eigenvectors for the initial sensor placement have highest values

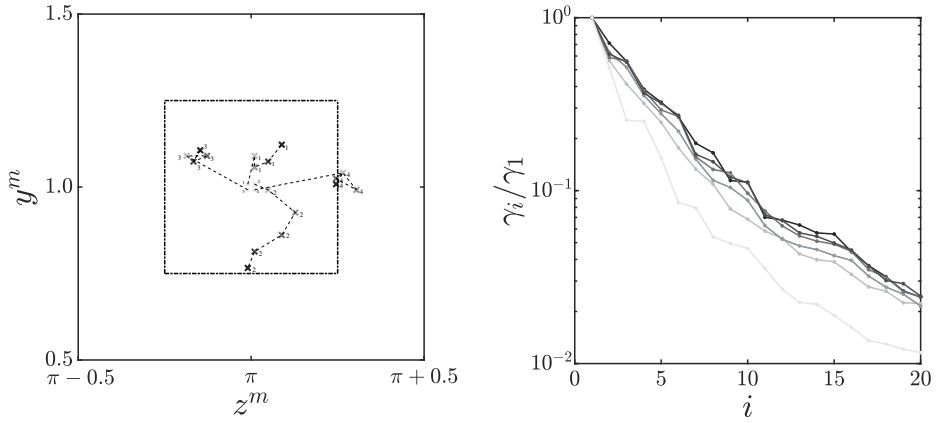

Figure 3-22. Left side plots the history of sensor placement during the subspace-tracking procedure. As more iterations are performed, we use darker markers for the sensors. The corresponding spectrums of the system are plotted on the right-hand side. We used γ_i (the eigen values of matrix $\mathbf{\Gamma} = \mathbf{\Phi}_n^T \mathbf{H} \mathbf{\Phi}_n$, where $\mathbf{\Phi}_n$ is the subspace we keep updating as the sensors move) to estimate $\lambda_i, i = 1, 2, \ldots, q$.

near the channel center, those from the optimal one become more sensitive to sources away from the center, as shown on the right panel of figure 3-23. To make sure that our subspace-tracking method has already converged, we plot the contour of κ_{15} estimated by γ_1/γ_{15} in figure 3-24 if we were to move one specific sensor around. The colored regions in the plots are where the estimated error ($\tilde{\epsilon}$) between γ_1/γ_{15} and the true condition number λ_1/λ_{15} is less than 5 percent. Similarly, the other three sensors are also located at their local minimums, although not shown here.

3.5.1 Comparison of reconstruction quality

In order to compare the reconstruction quality between initial and optimal sensors, five different y-z locations for the source were selected in the search domain, including the channel center ($y = 1,\ z = \pi$) and four peripheral locations ($y = 1 \pm 0.15,\ z = \pi \pm 0.15$). For each $y - z$ source location, we performed a series of adjoint-looping optimization to reconstruct the source at different x locations with the same $y - z$ coordinates. The selected x locations are evenly distributed on $1 \leq x \leq 4$. The expression of the true

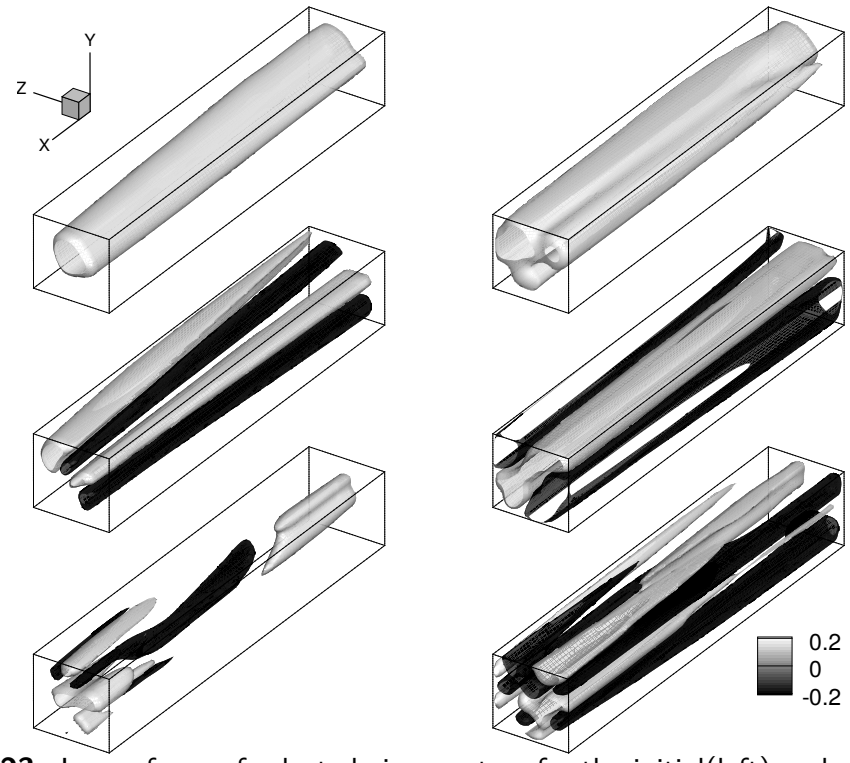

Figure 3-23. Iso-surfaces of selected eigenvectors for the initial(left) and optimal(right) sensor placements. From top to bottom we plot ϕ_1, ϕ_5 and ϕ_{20}, all normalized by their highest values.

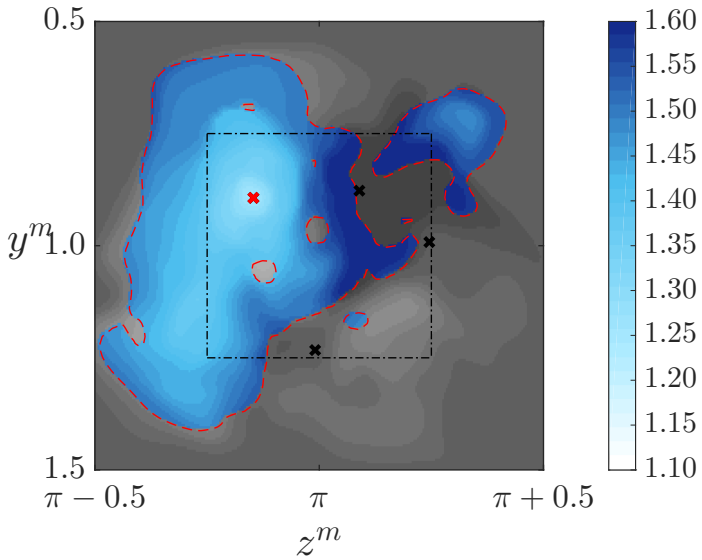

Figure 3-24. Contour of the condition number κ_{15} estimated by γ_1/γ_{15} if we were to move the target sensor (marked by red cross). The dashed lines marks the projection of the search region onto the sensor plane. We also estimate the error (denoted by $\tilde{\epsilon}$) between γ_1/γ_{15} and the true condition number λ_1/λ_{15}. In each figure, the trust/untrustworthy region is the blue/gray one, separated by the line contour of $\tilde{\epsilon} = 0.05$.

source is as follows,

$$\phi_T(\mathbf{x}) = \alpha\left[\cos\left(\rho\pi\right) + 1\right]\left[\text{sign}(1-\rho) + 1\right]. \tag{3.33}$$

$$\alpha = \frac{3}{2\left(\pi - 6/\pi\right)\rho_x\rho_y\rho_z}, \qquad \rho = \sqrt{\left(\frac{x-x_c}{\rho_x}\right)^2 + \left(\frac{y-y_c}{\rho_y}\right)^2 + \left(\frac{z-z_c}{\rho_z}\right)^2}, \tag{3.34}$$

where (x_c, y_c, z_c) is the location of the source, and $(\rho_x.\rho_y, \rho_z)$ is the size of the source in different directions. In current work they are all selected to be 0.1.

A brief summary of the adjoint-looping algorithm is provided here: i) Forward simulation are performed first to collect true measurement data. An initial guess of the source is selected (in this case, zero everywhere). ii) Forward simulations are performed to collect the measurement for estimated sources. iii) the deviation between estimated and true measurements drives the adjoint equation as source term. iv) the time-integrated adjoint scalar variable is the gradient of the cost functional to the steady source distribution. v) conjugate gradient method is then applied to utilize the gradient to update source estimation. vi) We go back to step ii) until convergence.

Readers interested in more detail of the algorithm are referred to Wang *et al.* [6] for formulation and discussion of the algorithm.

For the reconstruction quality comparison in three-dimensional search, the stopping criterion is set to be,

$$\epsilon_M = \frac{\sum_j \int_t \left(c(\mathbf{x}_j^m, t) - M_j(t)\right)^2 dt}{\sum_j \int_t \left(M_j(t)\right)^2 dt} \leq 0.001. \tag{3.35}$$

figure 3-25 shows a the side-view contours of sample reconstructions. The top contours show the reconstruction using initial sensors. It is good to reconstruct a source at the channel center, but not as good when we are trying to find a source near the boundary of the search domain. The results from optimal placement of sensors

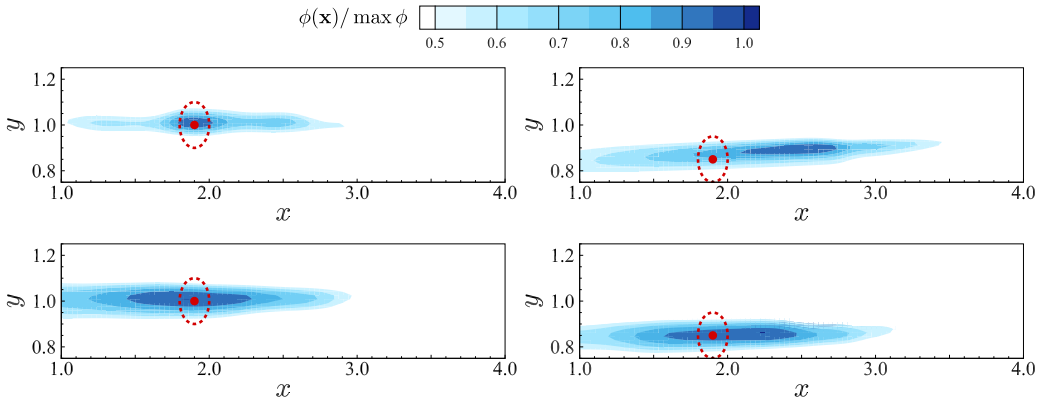

Figure 3-25. Side views of sample reconstruction. We are trying to reconstruct a source located at the channel center (left) or at a peripheral location ($y = 0.85, z = \pi - 0.15$). The red dashed lines marks the true source and the side-view planes cut through the center of the true source. Top contours show the reconstruction using initial sensors while bottom ones show those using optimal sensor placement.

are less accurate for source located at the channel center. However, for peripheral locations, the prediction is much more accurate.

To further quantify the reconstruction quality, we use the correlation coefficient between the true and reconstructed source,

$$R_{\phi\phi_T} = \frac{\int_V \phi(\mathbf{x})\phi_{True}(\mathbf{x})dV}{\phi_{rms}\phi_{T,rms}}. \tag{3.36}$$

to measure how well we can predict the true source. The correlation coefficients are plotted in figure 3-26 while the corresponding number of iterations are shown in figure 3-27. We can see that with similar number of iterations, the optimal placement of sensor sacrifices the accuracy to predict a source in the channel center to improve the sensitivity for peripheral sources. In all reconstructions, we improve the averaged correlation coefficient by 25% (from 0.19 to 0.25). We report here the computational cost to find the optimal arrangement in this three-dimensional search region is 220 forward-adjoint loops including 70 loops to obtain the initial subspace of 25 eigen vectors using Arnoldi iteration. This is a significant improvement over the brute force approach to find the correlation matrix for every possible sensor arrangement, on the order of 10^6 forward simulations.

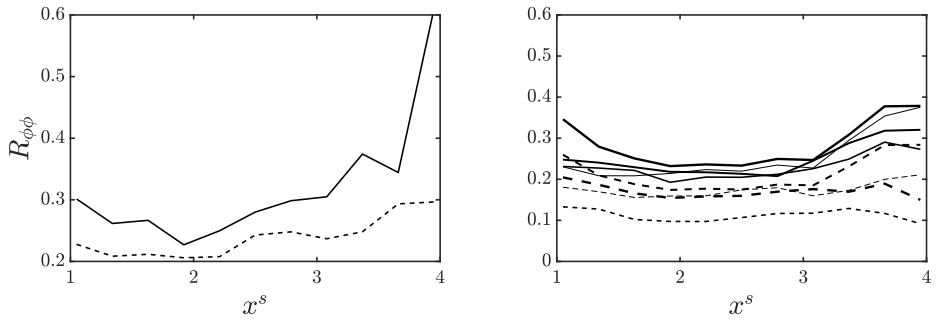

Figure 3-26. Correlation coefficients between true and reconstructed source versus the x-location of the source. Left figure shows the comparison of initial sensor placement (dashed) and optimal (solid) placement when trying to reconstruct a source in the channel center. Right figure show the comparison when trying to reconstruct a source at peripheral locations ($y^s = 1 \pm 0.15, z^s = \pi \pm 0.15$).

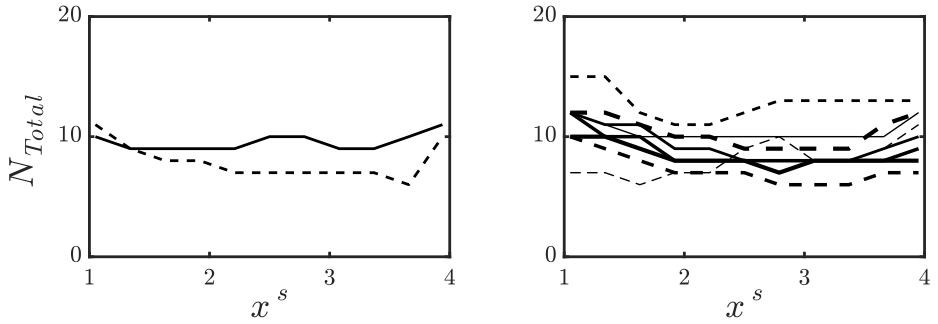

Figure 3-27. Number of iterations needed in order to meet the criterion ($\epsilon_M \leq 0.001$) versus the x-location of the source. Left figure shows the comparison of initial sensor placement (dashed) and optimal (solid) placement when trying to reconstruct a source in the channel center. Right figure show the comparison when trying to reconstruct a source at peripheral locations ($y^s = 1 \pm 0.15, z^s = \pi \pm 0.15$).

3.6 Optimal sensor weighting

It has been demonstrated that in §3.4.3, the condition of a system can be improved by changing the placement of a sensor network. However, without appropriate weighting of the sensors, the system can be easily corrupted by certain sensors that are not helpful to improve the condition of the system. As a result, even if we use all the sensors available, improvement of the results remains limited. With appropriate weighting of the sensor network, it is also possible to enhance the efficiency of the measurement (and thus the data assimilation process). This technique would be especically desirable in applications where it is not possible to adjust the sensor network (e. g. measurements of wall friction or pressure on the wall of a turbulent channel [69, 70] or airfoil [71, 72]), where we have to resort to weighting the sensor network to improve the condition of the system. When appropriate weightings $\omega_1, \omega_2, \ldots, \omega_N$ of the sensors $\mathbf{x}_1^m, \mathbf{x}_2^m, \ldots, \mathbf{x}_N^m$ are applied, the corresponding correlation matrix, denoted as $\mathbf{H}(\mathbf{x}^m; \omega)$, can be calculated by,

$$\mathbf{H}(\mathbf{x}^m; \omega) = \sum_{j=1}^{J} \omega_j \mathbf{H}\left(\mathbf{x}_j^m\right) \tag{3.37}$$

The objective in this section is to determine the optimal weighting $\omega = [\omega_1, \omega_2, \ldots, \omega_j, \ldots, \omega_J]$ for J fixed sensors $\mathbf{x}^m$ such that the condition number of $\mathbf{H}$, estimated by $\kappa_I = \lambda_1/\lambda_I$ is minimized. Notice that all $\mathbf{H}(\mathbf{x}^m)$ are positive definite, which is an important feature for variational approach to invert the matrix. Therefore, a constraint $\omega_j \geq 0$ is added to preserve this quality. Without loss of generality, we add another constraint that $\sum_j^J \omega_j = 1$.

We reinvestigate the one-dimensional reconstruction problem in the channel center. An introductory problem to determine the optimal weighting for two sensors: one directly downstream, the other at the optimal location, is presented as our first step.

The weight ω is placed on to the sensor at the center. As a result, the sensor at optimal location is weighted by $1-\omega$. As shown in figure 3-28. Since different criterion

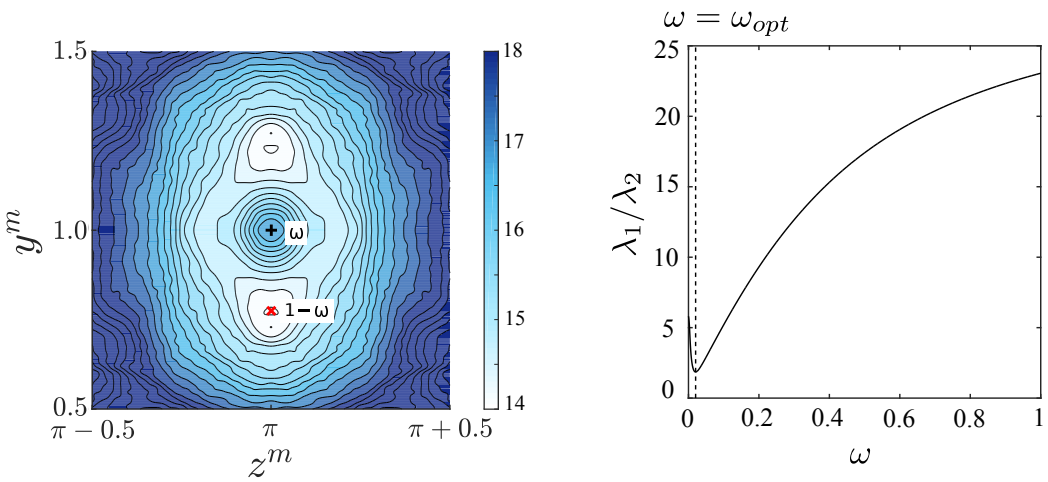

Figure 3-28. Schematic of determine the optimal weighting for a two-sensor case(left) and $\kappa_2 = \lambda_1/\lambda_2$ for different weighting (right). Optimal weighting ω_{opt} are marked by dashed line it the right figure.

gave us similar results, we only present $\kappa_2 = \lambda_1/\lambda_2$ here for different weighting within $0 \leq \omega \leq 1$.

The optimal weighting is found to be very close to 0, meaning that a large portion of weighting is applied to the optimal sensor away from the center while very limited weighting is added onto the sensor in the center. However, the small portion of weighting on the middle sensor is essential to improve the spectrum of the system, as shown in figure 3-29. If one weights the two sensors equally, namely $\omega = 0.5$, the resulting spectrum is actually worse than using one sensor at the optimal location. The slowest-decaying spectrum is found using the optimal weighting. Furthermore, the leading eigenvectors for the optimal weighting yields are more sensitive to a near source than a single optimal sensor in that the projection of a near source onto the subspace has non-zero values. This can again be observed in the reconstruction quality in figure 3-30. For farther sources, performance of the optimal weighting is nearly the same as using one sensor at optimal location while for near source, much less number of required iterations represents enhanced sensitivity. We then applied this idea to a larger sensor network. Similarly to the discussion for the previous multiple-sensor case, the optimal weighting here cannot be done by brute force and

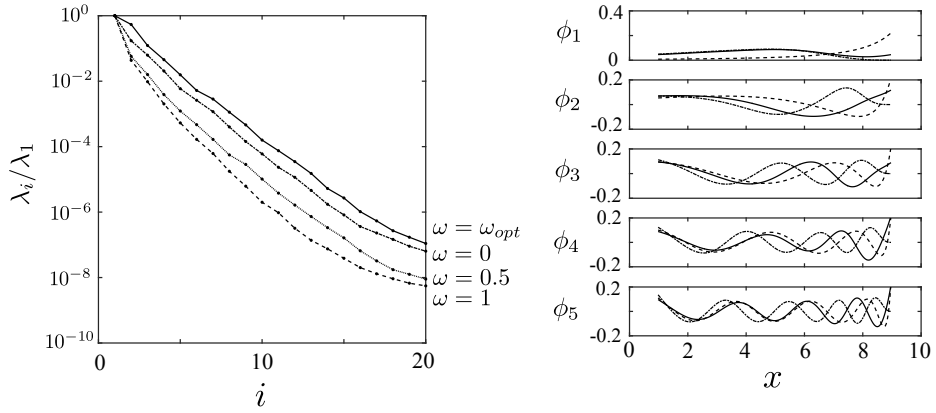

Figure 3-29. The leading eigen values (left) and eigen vectors (right) of the correlation matrix $\mathbf{H}$ for different weighting of two sensors: one located at the channel center, the other at aforementioned optimal location.

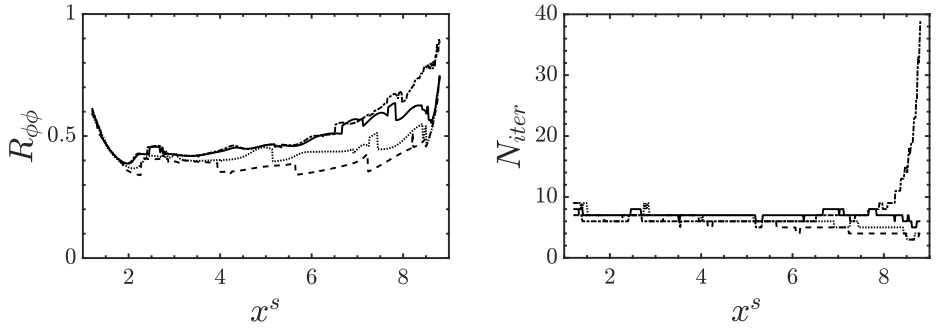

Figure 3-30. Top: Reconstruction quality of sources located at x^s along the channel centerline. Dashed line shows the results using one sensor at the channel center, dash-dotted line shows that with the sensor at the optimal location found by minimizing λ_1/λ_{15}. Dotted line shows the results using equal weighting of two sensor while the solid line uses the optimal weighting. Bottom: The number of iterations required to drive the cost functional to the converge criterion.

subspace tracking is needed to reduce the computational cost. We applied a similar procedure as to determine optimal location of the sensors to determine the optimal weighting, summarized in algorithm 3. This algorithm is then applied to determine

Algorithm 3: Subspace tracking algorithm for exploration of optimal sensor weighting.

- $n = 0$;
- Prescribe an initial weight of the sensors, ω_j;
- Choose the size of the subspace, q and the index I to estimate condition number κ_I. Make sure $q > I + 1$;
- Choose the allowed error level E of the eigenvalue estimate.;
- Perform Arnoldi iteration to obtain the starting subspace $\mathbf{\Phi}_0$ and the corresponding singular values;

while *Convergence condition is not satisfied* **do**

- Perform forward simulations with $\boldsymbol{\phi}_{n,l}, \quad l = 1, 2, \ldots, q$ and collect measurement data $\mathbf{m}_l(\mathbf{x}^m, t)$. Use equation 3.23 and evaluate matrix $\mathbf{\Gamma}$ for nearby sensor weighting;
- Evaluate the estimate error $\tilde{\epsilon}$ from equation 3.24;
- Establish the trust region $\Omega = \{\boldsymbol{\omega} \big| \tilde{\epsilon}_I < E, \sum \boldsymbol{\omega} = 1, \boldsymbol{\omega} > \mathbf{0}\}$ and change weighting to $(\boldsymbol{\omega})^{(n+1)} = arg \max_{\boldsymbol{\omega} \epsilon \Omega} \gamma_1 / \gamma_I$.;
- Perform adjoint simulations (Or evaluate $\mathbf{w}_l = \mathbf{A^T}[\boldsymbol{\omega}(\mathbf{x}^m)\mathbf{m}_l(\mathbf{x}^m, t)]$) for the new sensor weighting $(\boldsymbol{\omega})^{(n+1)}$.;
- Perform Q-R decomposition to matrix $\mathbf{W} = [\mathbf{w}_1, \mathbf{w}_2, \ldots, \mathbf{w}_q] = \mathbf{QR}^{-1}$ and used estimated subspace $\mathbf{\Phi}_{n+1} = \mathbf{Q}$ for the new sensor weighting.

end

the optimal weighting for 25 sensors evenly distributed in one quadrant on the cross-flow plane, as shown in figure 3-32. The size of the subspace is chosen to be $q = 20$. By following the previous procedure and minimize κ_{15}, we found the optimal weighting as plotted on the left. Only 5 sensors has positive weightings while the others have zero weighting. This reiterates the previous point that some sensors are actually not helpful in improving the condition of the system. The same optimal weighting is found using different initial weightings. Therefore the results shown here is the global optimal for κ_{15}. On the right-hand side of figure 3-32 the evolution of the spectrum is shown. After three iterations, the spectrum has converged near its optimal state and further

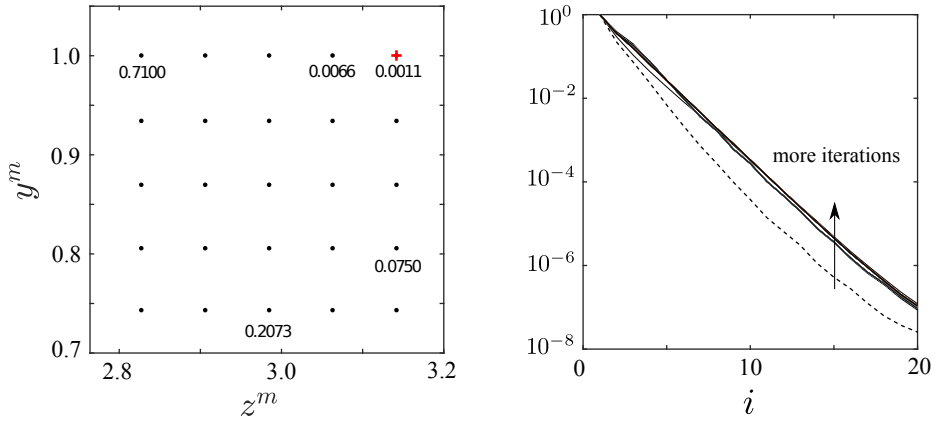

Figure 3-31. Left: Sensors distributed on one quadrant of the sensor plane with their optimal weights. Right: evolution for the spectrum of the correlation matrix $\mathbf{H}$ as the weights converge to the optimal, marked by darker lines. Dashed line shows the initial spectrum.

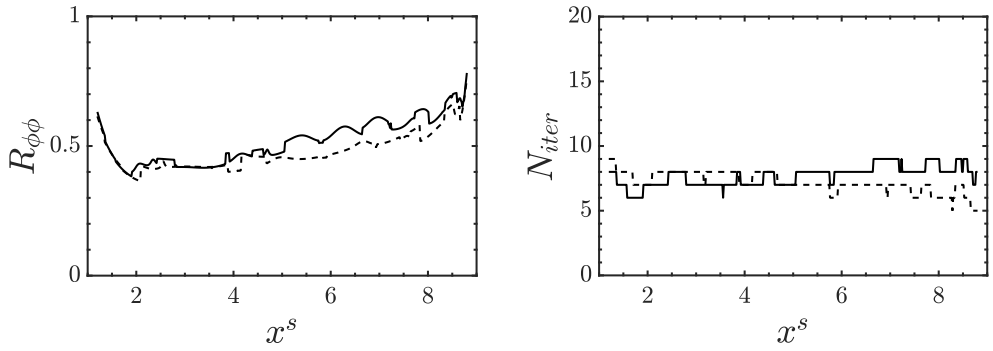

Figure 3-32. Top: Reconstruction quality of sources located at x^s along the channel centerline. Dashed line shows the results using one sensor at the channel center, dash-dotted line shows that with the sensor at the optimal location found by minimizing λ_1/λ_{15}. Bottom: The number of iterations required to drive the cost functional to the converge criterion.

improvement becomes very limited as more iterations are performed. Comparison of reconstruction quality in figure 3-31 shows that with the same computational cost, the optimal weighting is universally better than the initial average weighting and can obtain a maximum 20% improvement in the reconstruction quality.

3.7 Conclusions

The impulse-response matrix is essential to characterize the relation between scalar source distribution to sensor measurements. The Hessian matrix, also the cross-

correlation of the impulse-response matrix, encodes the difficulty of reconstructing the source, where the ill-posed nature of inverting the system can be shown by a quickly deteriorated eigen-spectrum of the Hessian, indicating a heavily dampened system by diffusion.

We introduced a framework, by which the optimal sensor placement is sought by minimizing the condition number of the Hessian matrix. The optimal sensor placement can then be solved by forming the matrices explicitly for all possible sensor placements, or in more general cases, by applying a subspace-tracking algorithm that gradually moves the sensors to their optimal arrangement.

The framework is then exercised to reconstruct the spatial distribution of a steady passive scalar source in a turbulent channel flow. For a simple case where the source is limited to a one-dimensional region in the x-direction, we calculate the impulse-response system by recording measurement data at all sensors from all possible source locations. The optimal single sensor is found to be away from the one directly downstream and borders on the edge of the plume from the nearest source, where its mean concentrate drops over 95% of its maximum value. Source reconstruction by variational optimization techniques is performed to shown that the reconstruction quality is indeed improved using the optimal sensor for this one-dimensional reconstruction. We trace the superiority of the optimal sensor to the shifting-source correlation coefficient, which quantifies the ability of a sensor to differentiate sources from nearby locations. The optimal sensor near the plume edge is found to have a much less shifting-source correlation coefficient.

To show the full capacity of the algorithm, we also apply it in placing multiple sensors and for a three-dimensional search. Improvement of the reconstruction quality is validated and explained.

For wider applications where sensor location are pre-defined and constrained to be stationary, we show that the algorithm can also be modified into determining the

optimal weighting of stationary sensors.

For future work, we can either consider more complex flow configurations, or develop the algorithm that can determine simultaneously the optimal placement and optimal weighting of the sensors.

Chapter 4

An eigen-ensemble-variational algorithm for identifying scalar sources from remote measurements in turbulent environments

4.1 Introduction

Sources of pollutants from either natural disasters or human activities can influence a large area in a short time and pose serious threats to public safety. Quickly localizing the source of such contaminants from information provided by remote sensors is of crucial importance. With high-fidelity simulation available for turbulent flows, using fully-resolved velocity fields for scalar source reconstruction becomes a new possibility. Algorithms for such source determination with some access to the velocity fields attracted broad attention recently. Our previous work focused on reconstructing the source as a general function (either temporal or spatial) while in many applications, the source could be characterized by a limited number of parameters, which is the goal of the search algorithm. The objective of current work is to propose an algorithm that determines the location and intensity of a steady scalar source in a turbulent environment with limited number of forward simulations. In most of the natural situations, turbulent dispersion quickly breaks the plume into smaller patches away from the source while molecular diffusion smears out the characteristics of the plume

structures, reducing our ability of tracing back from remote sensing. The problem becomes more difficult when the measurement data has noise. However, the difficulty of source localization with measurement error has never been quantified in turbulent environment. In current work we also quantify the effect of measurement error by the ratio between standard deviation of the reconstructed source parameters and that of the measurement error. Different source and sensor arrangements have been examined.

4.1.1 Methods for source reconstruction

Previous research regarding source identification has been summarized by Liu & Zhai [13]. Some of the work focused on reconstructing the source as a general spatial or temporal function and tried to invert the whole system. Other methods suppose the source is of a known shape and tried to find its parameters. While we are particularly inspired by the latter choice, we review the two choices separately and compare them. For reconstructing the source as a general function, it is inevitable to invert the whole input-output system. [14] first formulated the source-tracking problem in two dimensional steady groundwater system under a linear optimization framework. Using separate forward simulations for impulses at different potential source locations, a unit impulse-response matrix (the "concentration response matrix") can be built with each row representing measurements from a unit release from each potential source location. Linear programming and multiple regression was then used to solve the source distribution as a function of space. However, this method is not feasible in unsteady turbulent environment unless tremendous efforts has been made for limiting the potential locations of the source. While directly reconstructing the impulse-response matrix within a large search area become impossible in turbulent environment. With fully resolved velocity fields available, the adjoint operator can be used to trace back to potential source locations from sensor measurements. A recent work by [5] devel-

oped an iterative method using both forward and adjoint simulations to recover the release history of a source at a unknown location based on sensor measurements of scalar concentration in a turbulent channel flow ($Re_\tau = 150, Sc = 1$). Huang *et al.* [24] introduced the method of conjugate gradient to estimation on the space and time-dependent scalar source function. A similar approach, formed in an adjoint-looping manner was examine in spatial reconstruction of a localized scalar source in turbulent channel flow (cite myself). However, reconstructing the source as a general function requires inverting the whole system. In turbulent environment such system could be ill-conditioned with a large condition number (cite our optimal sensor paper) and thus inverting becomes very difficult. Moreover, Oftentimes the shape of the source is assumed to be know and the location and intensity are the primary focus. Therefore, some research focused on reconstructing the source parameters with a known shape. [15] determined the source parameters in one-dimensional uniform steady flow using Non-linear least squares method with Newton-Raphson algorithm. They build the impulse-response directly from analytical solution of the scalar fields. Similar scenarios has been investigated by [73] using the Tihkonov regularization. Keats *et al.* [4] constructed the impulse-response matrix explicitly using adjoint simulations in a steady-flow scenario and used the full matrix to find the source location. However, in a turbulent environment, building the impulse-response matrix requires tremendous efforts and therefore is not always an option. In the currently work we show that it suffices to run a limited number of forward simulations using selected ensemble members as scalar sources. Comparison between the true measurement from the source and those from a limited number of ensemble members provide enough information to infer the source with low requirement of computational resources.

4.1.2 Uncertainty quantification

In reality, the observation data will inevitably be influenced by noise. A system with diffusion is difficulty to invert because a small noise in the ending state, or the output will be amplified and influence our estimate of the initial state, or the input. Therefore, for diffusive systems, the difficulty of inferring the initial state can be quantified by the ratio between the error in the reconstruction of input and that of the observation. However, such work has never been done in turbulent environment regarding scalar source reconstruction. [4] took into account Gaussian noise in the measurement. After they built the impulse-response matrix, PDF of the predicted source parameter was found by repeated experiments. (Davide et al. 2017) examined the effect of Gaussian noise in the measurement data by comparing the reconstruction results using the measurement data with and without noise. In this case performing multiple numerical experiment with different samples of measurement noise is too costly and the effect was shown qualitatively. In addition to developing an algorithm to find scalar source parameters in turbulent environment, the objective of current work also includes quantifying the effect of measurement error especially in localization of the source. As a first step, we focus on a simply problem of reconstructing the intensity and x-location of a source in the center of a turbulent channel flow. Since the algorithm relies on accurate prediction of the eigen sources of the system, we show different ways to estimate eigen sources. These methods, combined with the algorithm are examined. Then we discuss the effect of measurement noise. This effect can be quantified by doing repeated reconstruction or analytically solved and related to scalar field statistics. Then we arrange different source and sensor placements and compare the difficulty of the reconstruction for both one-dimensional reconstruction (intensity and x-location) and three-dimensional reconstruction (intensity and all x, y, z locations). The structure of this paper is as follows: We start by showing the derivation of the impulse-response matrix together with its properties

in section 1.3. In section 2 we will show the ensemble-based method to reconstruct the source parameters. Three ways of estimating the eigen sources of the system has been proposed and examined. In section 3 we will test the effect of measurement noise. We will analytically solve for the standard deviation of the reconstruction of source parameters. The results are then validated by repeated experiments using different samples of measurement error. Both one-dimensional and three-dimensional reconstruction has been investigated. Different source and sensor positioning is compared. Our method can be easily applied to reconstructing multiple sources simultaneously. Section 4 shows the results for multiple sources.

4.1.3 Impulse-Response matrix

We consider the same problem setup used in the previous chapter. When the velocity fields are known, the measurement data for a given sensor is linearly dependent on the source distribution $\phi(\mathbf{x})$. From the governing equation:

$$\mathbf{L}c = \phi(\mathbf{x}), \tag{4.1}$$

we have,

$$c = \mathbf{L}^{-1}\phi(\mathbf{x}). \tag{4.2}$$

The measurement data for a certain sensor placement $\mathbf{x}_j^m$ can be written as

$$M(t) = \int_V \delta(\mathbf{x} - \mathbf{x}^m)\, c\, dV = \delta^T(\mathbf{x} - \mathbf{x}^m)\mathbf{L}^{-1}\phi(\mathbf{x}). \tag{4.3}$$

Here $\delta^T(\mathbf{x} - \mathbf{x}^m) = \left[\delta(\mathbf{x} - \mathbf{x}_1^m), \delta(\mathbf{x} - \mathbf{x}_1^m), \ldots, \delta(\mathbf{x} - \mathbf{x}_N^m)\right]^T$ represents vertical concatenation of spatial δ-functions as horizontal vectors. If we write $\phi(\mathbf{x})$ in terms of different δ-functions,

$$\phi(\mathbf{x}) = \sum_k \delta(\mathbf{x} - \mathbf{x}_k)\phi(\mathbf{x}_k). \tag{4.4}$$

The measurement data can be reformulated as a superposition of measurements from different point sources,

$$\begin{aligned} M(t) &= \delta^T(\mathbf{x}-\mathbf{x}^m)\mathbf{L}^{-1}\phi(\mathbf{x}). \\ &= \delta^T(\mathbf{x}-\mathbf{x}^m)\mathbf{L}^{-1}\sum_k \delta(\mathbf{x}-\mathbf{x}_k)\phi(\mathbf{x}_k) \\ &= \sum_k \left(\delta^T(\mathbf{x}-\mathbf{x}^m)\mathbf{L}^{-1}\delta(\mathbf{x}-\mathbf{x}_k)\right)\phi(\mathbf{x}_k). \end{aligned} \tag{4.5}$$

If we write $\delta^T(\mathbf{x}-\mathbf{x}^m)\mathbf{L}^{-1}\delta(\mathbf{x}-\mathbf{x}_k)$ as $c(\mathbf{x}^m,t;\mathbf{x}_k)$, which represents the measurement sequence from a point source at $\mathbf{x}_k$, then

$$M(t) = \sum_k c(\mathbf{x}^m,t;\mathbf{x}_k)\phi(\mathbf{x}_k). \tag{4.6}$$

If we write matrix $\mathbf{A}$ as $A_{lk} = c(\mathbf{x}^m,t_l;\mathbf{x}_k)$, then the source-sensor response system can be simple written as,

$$M(t) = \mathbf{A}\phi(\mathbf{x}). \tag{4.7}$$

It is worth noticing that the number of rows of $\mathbf{A}$ depends on the time horizon we are working on, if we update the measurement M by adding more recent data and extend the time horizon, the number of rows in matrix $\mathbf{A}$ will increase while the number of columns unchanged (since the number of grid points in the search domain does not change). Therefore, the size of $\mathbf{A}^T\mathbf{A}$ remains the same with each of its element, $(A^TA)_{lk} = \sum_j A_{jl}A_{jk} = \sum_{j=1}^{N_T} c(\mathbf{x}^m,t_j;\mathbf{x}_l)c(\mathbf{x}^m,t_j;\mathbf{x}_k) \to N_t\ \overline{c(\mathbf{x}^m,t;\mathbf{x}_l)c(\mathbf{x}^m,t;\mathbf{x}_l)}^{\langle t\rangle}$ converging to the correlation of scalar fields from different source locations. It can be easily proven that if the length of the time horizon, or the number of time steps N_T for a fixed step size, is large enough, the eigen vectors of matrix $\mathbf{A}^T\mathbf{A}$ will converge to the eigen vectors of matrix $\mathcal{C}_{lk} = \overline{c(\mathbf{x}^m,t;\mathbf{x}_l)c(\mathbf{x}^m,t;\mathbf{x}_l)}^{\langle t\rangle}$ since their only difference is a constant N_T.

4.2 POD-based ensemble method

We select a series of suitable ensemble members, denoted as $\phi^{(i)}, \quad i = 1,2,\ldots,N_{ens}$ to form a matrix $\mathbf{E} = \left(\phi^{(1)},\phi^{(2)},\ldots,\phi^{(N_{ens})}\right)$. Without loss of generality, we can assume

the ensemble members $\phi^{(i)}$ form a set of orthogonal basis,

$$\phi^{(i),T}\phi^{(j)} = \delta_{ij}, \quad i = 1, 2, \ldots, N_{ens},\ j = 1, 2, \ldots, N_{ens}. \tag{4.8}$$

Using the ensemble as a group of scalar sources, the corresponding measurement can be collected to form the observation matrix $\mathbf{H}$. According to our notation in §2,

$$\mathbf{O} = \mathbf{AE} = \left[\mathbf{A}\phi^{(1)}, \mathbf{A}\phi^{(2)}, \ldots, \mathbf{A}\phi^{(N_{ens})}\right] = \left[M_1, M_2, \ldots, M_{N_{ens}}\right] \tag{4.9}$$

When a measurement signal from the true source, $M = \mathbf{A}\phi$ is available, the ultimate goal is to infer the source location and intensity through comparison between M and $M_{(i)}$ from the ensemble members. This procedure is summarized in figure 4-1. If the shape of ϕ is not known and is regarded as a general distribution, normally we can assume ϕ is a linear superposition of the ensemble members, thusly $\phi = \mathbf{E}\boldsymbol{\omega}$ and we solve for $\boldsymbol{\omega}$, the vector of weights for all the ensemble members. However, when the shape of ϕ is known, as in the current study, the true source ϕ cannot be assumed as linear superposition of the ensemble members. In this case simply inverting the system formed by the ensemble does not help to find the source parameters. Nevertheless, if the ensemble members $\phi^{(i)}$ satisfy certain condition, it is possible to find corresponding constants λ_i such that we have the following linear relation,

$$\lambda_i \phi^T \phi^{(i)} = M^T M_i, \quad i = 1, 2, \ldots, N_{ens}, \tag{4.10}$$

to hold for any arbitrary ϕ. It is therefore possible to infer the source parameters since $\phi^{(i)}, M_i, M$ and λ_i are known in the above equation.

In fact, equation 4.10 yields that

$$\lambda_i \phi^T \phi^{(i)} = (\mathbf{A}\phi)^T \left(\mathbf{A}\phi^{(i)}\right) = \phi^T \left(\mathbf{A}^T\mathbf{A}\right)\phi^{(i)} \tag{4.11}$$

holds for arbitrary ϕ, therefore we have

$$\lambda_i \phi^{(i)} = \left(\mathbf{A}^T\mathbf{A}\right)\phi^{(i)}. \tag{4.12}$$

$\phi^{(i)}$ has to be the eigen vectors of $\mathbf{A}^T\mathbf{A}$ and λ_i the corresponding eigen values. Since $\phi^{(i)}$ form the eigen space the true source ϕ is projected onto, we can call $\phi^{(i)}$ "Eigen Sources". Therefore, the key for using equation 4.10 to infer the source is the ability to approximate the eigen value and eigen sources accurately. Equation 4.10 can also be written compactly as,

$$\mathbf{\Lambda E}\phi\left(I^s, \mathbf{x}^s\right) = \mathbf{O}^T M. \tag{4.13}$$

4.2.1 Different methods to approximate the eigen sources

If we have no access to the eigen sources of the system and we have to use a general ensemble $\mathbf{E}_0$, we can include a POD procedure to estimate the eigen sources from the ensemble we selected. The process can be summarized as follows.

1. Start from a general orthonormal ensemble members $e_0^{(i)}$ forming a matrix $\mathbf{E}_0 = \left[e_0^{(1)}, e_0^{(2)}, \ldots, e_0^{(N_{ens})}\right]$ and use them as sources to obtain the observation matrix $\mathbf{O}_0 = \mathbf{A}\mathbf{E}_0$.

2. Perform an eigen decomposition of matrix $\mathbf{O}_0^T\mathbf{O}_0$, solving

$$\mathbf{O}_0^T\mathbf{O}_0 q^{(i)} = \lambda_i q^{(i)}. \tag{4.14}$$

   If we denote $\mathbf{Q} = [q^{(1)}, q^{(2)}, \ldots, q^{(N_{ens})}]$. $\mathbf{Q}$ is a unitary matrix we can use to adjust our ensemble as follows,

$$\mathbf{E} = \mathbf{E}_0\mathbf{Q}, \quad \mathbf{O} = \mathbf{O}_0\mathbf{Q}. \tag{4.15}$$

   Notice the new ensemble $\mathbf{E} = [\phi^{(1)}, \phi^{(2)}, \ldots, \phi^{(N_{ens})}]$ remain orthonormal and the their corresponding measurements are also orthonormal since

$$\mathbf{O}^T\mathbf{O} = \mathbf{Q}^T\mathbf{O}_0^T\mathbf{O}_0\mathbf{Q} = \mathbf{I}. \tag{4.16}$$

   Performing this eigen decomposition is equivalent as a POD procedure for the measurement data. Moreover, we are actually performing a subspace iteration

to update our estimate of the eigen vectors from $\mathbf{E}_0$ to $\mathbf{E}$. Therefore using $\mathbf{E}$ instead of $\mathbf{E}_0$ yields more accurate results.

3. Notice that it is not necessary to rerun the forward calculation using $\mathbf{E}$ since the results for $\mathbf{E}$ can be obtained by a known linear transformation $\mathbf{Q}$ from the results of $\mathbf{E}_0$. The eigen values of $\mathbf{O}_0^T\mathbf{O}_0$ can be used as λ_i. Then we can use $\mathbf{E}$ and λ_i to infer the source parameter.

From previous analysis in section 2.2 we know the eigen vectors of matrix $\mathbf{A}^T\mathbf{A}$ will converge to the eigen vectors of matrix $\mathcal{C}_{lk} = \overline{c(\mathbf{x}^m, t; \mathbf{x}_l)c(\mathbf{x}^m, t; \mathbf{x}_l)}^{\langle t \rangle}$ since their only difference is a constant N_T. As a result, it is possible to approximate the eigen sources for the new time horizon $0 < t < T$ using converged eigen sources obtained from historical data (for example, from time horizon $-\mathcal{T}_h < t < 0$ where $\mathcal{T}_h$ is large enough). Therefore, if we have historical data and access to some old eigen sources, our second option to estimate the eigen sources can be described as follows,

1. Obtain converged eigen sources $\phi_0^{(i)}$ from historical data in time horizon $\mathcal{T}_h < t < 0$. This can be done either by running forward simulations from sources located at every grid points in the search domain, forming matrix $\mathbf{A}$ explicitly, or by running forward and adjoint simulations iteratively and perform an Arnoldi procedure. Either way the velocity fields are needed.

2. Use the converged eigen sources as ensemble members, $\phi^{(i)} = \phi_0^{(i)}$. Collect measurement data as a function of time for each ensemble member. The up-to-date eigen values can be estimated by,

$$\lambda_i \approx \frac{||\mathbf{A}\phi^{(i)}||^2}{||\phi^{(i)}||^2} = ||M_i||^2. \tag{4.17}$$

3. use $\phi^{(i)}$ and λ_i to infer the source parameters whenever we have M from the true source.

However, the above procedure requires huge efforts for obtaining the converged eigen sources. The following second option allows us to start with any general ensemble member and update the ensemble based on the measurement data. To further increase the accuracy of estimating the eigen sources $\phi^{(i)}$, instead of using a general ensemble combined with POD analysis, we can start from the converged eigen sources and perform the POD process. Which results in the following third option:

1. Start from the converged eigen sources $\phi_0^{(i)}$ forming a matrix $\mathbf{\Phi}_0 = \left[\phi_0^{(1)}, \phi_0^{(2)}, \ldots, \phi_0^{(N_{ens})}\right]$ and use them as sources to obtain the measurement matrix $\mathbf{M}_0 = \mathbf{A}\mathbf{\Phi}_0$.

2. Perform an eigen decomposition of matrix $\mathbf{O}_0^T\mathbf{O}_0$, solving

$$\mathbf{O}_0^T\mathbf{O}_0 q^{(i)} = \lambda_i q^{(i)}. \tag{4.18}$$

   If we denote $\mathbf{Q} = [q^{(1)}, q^{(2)}, \ldots, q^{(N_{ens})}]$. $\mathbf{Q}$ is a unitary matrix we can use to adjust our ensemble as follows,

$$\mathbf{E} = \mathbf{\Phi}_0\mathbf{Q}, \quad \mathbf{O} = \mathbf{O}_0\mathbf{Q}. \tag{4.19}$$

   Notice the new ensemble $\mathbf{E} = [\phi^{(1)}, \phi^{(2)}, \ldots, \phi^{(N_{ens})}]$ remain orthonormal and the their corresponding measurements are also orthonormal since

$$\mathbf{O}^T\mathbf{O} = \mathbf{Q}^T\mathbf{O}_0^T\mathbf{O}_0\mathbf{Q} = \mathbf{I}. \tag{4.20}$$

3. The eigen values of $\mathbf{O}_0^T\mathbf{O}_0$ can be used as λ_i. Then we use $\mathbf{E}$ and λ_i to infer the source parameter.

4.2.2 Constrained optimization

When the ensemble members $\phi^{(i)}$, responses M_i and coefficients λ_i are obtained, we select the source to satisfy Equations. 4.10 the best. The solution is confined as a δ-function in space for a concentrated source:

$$\phi(\mathbf{x}) = I^s\delta(\mathbf{x} - \mathbf{x}^s), \tag{4.21}$$

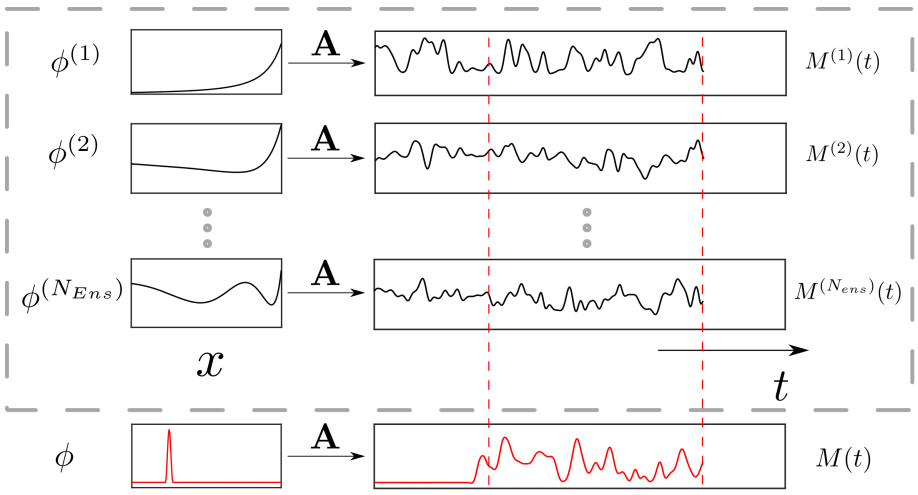

Figure 4-1. Schematic of the ensemble monitoring process

where I^s and $\mathbf{x}^s$ are the intensity and location of the source, respectively. In numerical simulation, the spatial δ-function is approximated by a three-dimensional cut-off cosine function,

$$\delta(\mathbf{x}-\mathbf{x}^s) \to \xi\left[\cos\left(\frac{\pi|\mathbf{x}-\mathbf{x}^s|}{r_0}\right)+1\right]\Big[\,\mathrm{sign}(r_0-|\mathbf{x}-\mathbf{x}^s|)+1\Big]. \tag{4.22}$$

where r_0 is the size of the source and ξ is a coefficient to make sure the spatial integration of the RHS is 1. For a 1-D δ-function,

$$\xi = \frac{1}{4r_0}, \tag{4.23}$$

and for a 3-D δ-function,

$$\xi = \frac{3}{2\,(\pi - 6/\pi)\,r_0^3}. \tag{4.24}$$

Therefore, the source can be parameterized by the parameter I^s and $\mathbf{x}^s$. We can define our cost function to be the accumulated difference between LHS and RHS of Equation 4.10,

$$J(I^s,\mathbf{x}^s) = \sum_{i=1}^{N_{ens}} \|\lambda_i \boldsymbol{\phi}^{(i),T}\boldsymbol{\phi}(I^s,\mathbf{x}^s) - \mathbf{M}_i^T\mathbf{M}\|^2, \tag{4.25}$$

or simply,

$$J(I^s,\mathbf{x}^s) = \|\Lambda\mathbf{E}^T\phi(I^s,\mathbf{x}^s) - \mathbf{O}^T M\|^2, \tag{4.26}$$

The set of parameters $I^s, \mathbf{x}^s$ is chosen such that the cost function is minimized. Therefore, we formulate the source-finding problem into a low degree-of-freedom nonlinear optimization problem, which can be easily performed by inner-point-Newton-Raphson iterations.

4.2.3 One-dimensional reconstruction

Now we compare the three options of estimating eigen sources in section. 3.1. For simplicity, we focus on a one-dimensional reconstruction problem. In this case only the intensity I^s and x^s of the source is unknown. For the first option to use converged eigen sources, we used the time horizon $-\mathcal{T}_h < t < 0$, where $\mathcal{T}_h U/h = 50$ to construct the impulse-response matrix $\mathbf{A}_0$ explicit by running forward simulations from sources located at every different grid points in the search domain. From matrix $\mathbf{A}_0$ we obtain the converged leading eigen sources $v_i, i = 1, 2, \ldots, N_{ens}$. We then use $\phi^{(i)} = v_i$ to infer the source parameters. The results for reconstructing sources at different locations using different number of ensemble members in the time horizon $0 < t < \mathbf{T}$ are plotted in figure 4-3. The accuracy for the prediction relies on the different between the true eigen sources for time horizon $0 < t < \mathcal{T}$ and those for $-\mathcal{T}_h < t < 0$. While this is no big different if we use slightly more ensemble members, when $\mathcal{T}$ become larger, the eigen sources become more converged and thusly our prediction is more accurate.

Instead of the converged eigen sources, we can start from general orthonormal ensemble members. Here we use ortho-normalized Gaussians distributions equally cover the search domain. The original gaussian can be expressed as,

$$e_0^{(i)} = \mathcal{N}(i\frac{L}{N_{ens}+1}, \frac{2L}{N_{ens}}), \tag{4.27}$$

where L is the length of the search domain. Then these Gaussians are ortho-normalized to obtain an orthogonal basis $e^{(i)}$, as plotted in figure 4-2 on the right-hand side. Using these Gaussians with a POD procedure, reconstruction of the source parameters is shown in figure 4-3a. While we have more accurate predictions when we use more en-

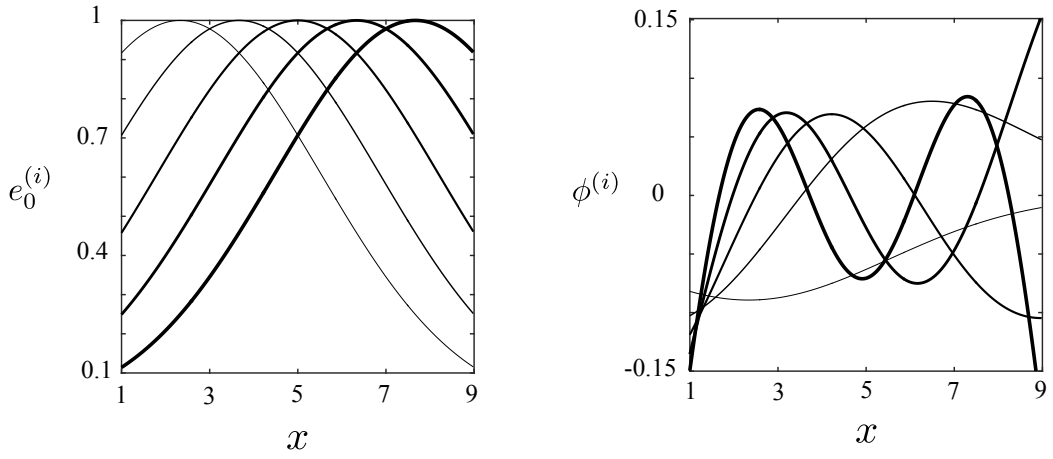

Figure 4-2. One-dimensional Gaussian distributions to cover the search domain and ortho-normalized Gaussians as ensemble members $\phi^{(i)}$.

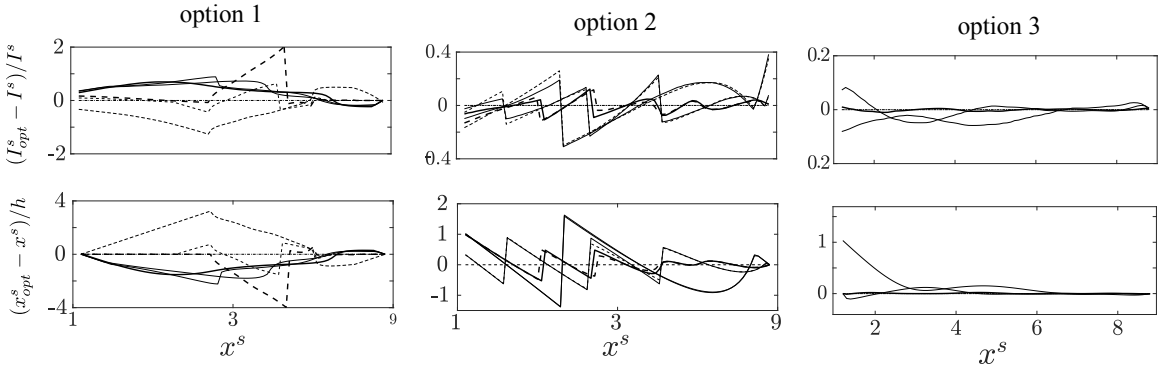

Figure 4-3. Reconstructing the source at different locations using ensemble members from normalized Gaussians. Thicker lines represents increasing number of ensemble members (N_{ens} = $\{3, 5, 7\}$). Dashed lines represent the true parameters of the source. Left and right figures use different time horizons $\mathcal{T}$ = 10 and $\mathcal{T}$ = 20, respectively.

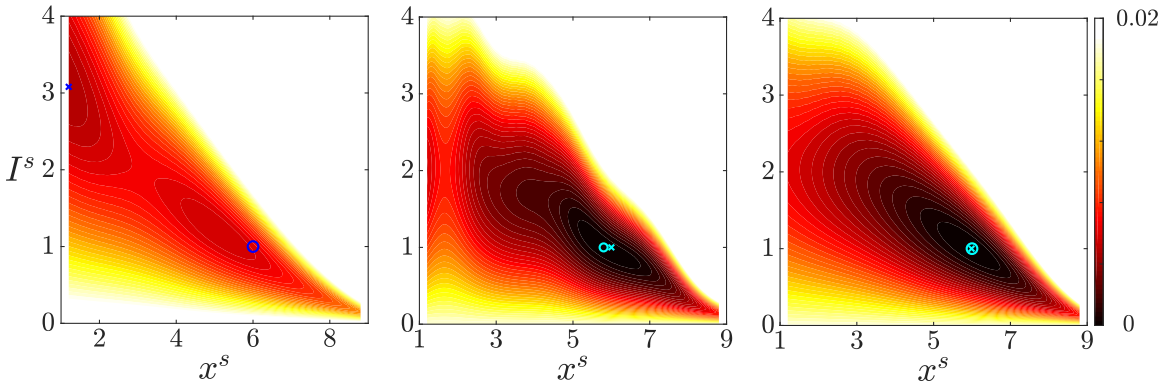

Figure 4-4. Contour of cost function J for different source parameters using different ensembles. From left to right we use ortho-normalized Gaussians, historical eigen sources from $-50 < t < 0$ and POD-processed hostorical eigen sources.

semble members, the accuracy of the reconstruction does not shown clear dependency on the time horizon. It is worth noticing that the curves in figure 4-3b are stairway-shaped and yield better prediction at the location where one of the Gaussian ensemble member is centered. In this case, the quality of the prediction is influenced mainly by the number and shape of the ensemble members. By combining the converged eigen sources with a POD procedure, we can greatly improve the prediction in figure 4-3b and obtain the results in figure 4-3c. When we use more than 5 ensemble members, the prediction of the source parameters is nearly the same as the true parameters.

4.3 Effect of measurement noise

We have demonstrated that the systematic error of the reconstruction comes only from the discrepancy between our ensemble members and the eigen sources of the system. From now on, we suppose the ensemble members $\phi^{(i)}$ we use are the true eigen source v_i. We denote $\mathbf{E} = \mathbf{\Phi}$ and $\mathbf{O} = \mathbf{U}$ where $\mathbf{\Phi}$ is the subspace formed by leading eigen sources of $\mathbf{A}$ and $\mathbf{U}$ the space of the corresponding eigen measurements. After doing this, we assume there is no systematic error and examine the effect of measurement noise. As a result, we should add noise to equation 4.31, which then

becomes

$$\mathbf{\Lambda\Phi}^T\phi = \mathbf{U}^T\left(M + \epsilon_M\right). \tag{4.28}$$

The most efficient way to perturb the equation would be adding a noise directly to the coefficients of the eigen-measurements. We also assume that the perturbation is proportional to the true intensity of the source, which means

$$\epsilon_M = I^s\mathbf{Ob}, \tag{4.29}$$

where $\mathbf{b}$ is a q-dimensional vector of Guassian noise with the covariance matrix $\mathbf{B}$. This particular form of measurement noise makes equation (3.6) a simpler form,

$$\mathbf{\Lambda E}^T\phi = \mathbf{O}^T M + I^s\mathbf{b}, \quad \mathbf{b} \sim \mathcal{N}_q(0, \mathbf{B}). \tag{4.30}$$

One way to solve this noise system is to sample different $\mathbf{b}$ and repeat the optimization process, from which we can obtain a cloud of the source parameters and thus get their probability distribution function.

We can also use perturbation analysis to obtain the pdf of source parameters through the eigenvalues and eigen-sources of the system.

4.3.1 Perturbation analysis

The true source ϕ_0 would satisfy the equation

$$\mathbf{\Lambda\Phi}^T\phi_0 = \mathbf{U}^T M. \tag{4.31}$$

subtract equation 4.31 from 4.30 we have,

$$\mathbf{\Lambda\Phi}^T\Delta\phi = I^s\mathbf{b}, \quad \mathbf{b} \sim \mathcal{N}_q(0, \mathbf{B}), \tag{4.32}$$

where

$$\begin{aligned}
\Delta\phi &= dI^s\delta(\mathbf{x} - \mathbf{x}^s) + I^s\frac{\partial\delta(\mathbf{x} - \mathbf{x}^s)}{\partial\mathbf{x}^s}\Delta\mathbf{x}^s \\
&= \begin{bmatrix}\delta(\mathbf{x} - \mathbf{x}^s) & I^s\dfrac{\partial\delta(\mathbf{x} - \mathbf{x}^s)}{\partial\mathbf{x}^s}\end{bmatrix}\begin{bmatrix}dI^s \\ \\ d\mathbf{x}^s\end{bmatrix} \\
&= \begin{bmatrix}\delta(\mathbf{x} - \mathbf{x}^s) & I^s\dfrac{\partial\delta(\mathbf{x} - \mathbf{x}^s)}{\partial\mathbf{x}^s}\end{bmatrix}\begin{bmatrix}dI^s \\ \\ d\mathbf{x}^s\end{bmatrix}.
\end{aligned} \tag{4.33}$$

Therefore

$$I^s \mathbf{\Lambda \Phi}^T \begin{bmatrix} \delta(\mathbf{x}-\mathbf{x}^s) & \dfrac{\partial \delta(\mathbf{x}-\mathbf{x}^s)}{\partial \mathbf{x}^s} \end{bmatrix} \begin{bmatrix} dI^s/I^s \\ d\mathbf{x}^s \end{bmatrix} = I^s \mathbf{b}, \tag{4.34}$$

and

$$\underbrace{\mathbf{\Lambda \Phi}^T \begin{bmatrix} \delta(\mathbf{x}-\mathbf{x}^s) & \dfrac{\partial \delta(\mathbf{x}-\mathbf{x}^s)}{\partial \mathbf{x}^s} \end{bmatrix}}_{\mathbf{K}} \begin{bmatrix} dI^s/I^s \\ d\mathbf{x}^s \end{bmatrix} = \mathbf{b} \tag{4.35}$$

Matrix $\mathbf{K} = \mathbf{K}(\mathbf{x}^s)$ is a function of the true source location. If we regard every row of $\mathbf{\Phi}^T$ as an eigen-source distribution $\phi_i^T(\mathbf{x})$, the matrix $\mathbf{K}$ can then be written as,

$$\mathbf{K} = \mathbf{\Lambda} \begin{bmatrix} \mathbf{\Phi}^T\Big|_{\mathbf{x}^s} & \nabla \mathbf{\Phi}^T\Big|_{\mathbf{x}^s} \end{bmatrix} \tag{4.36}$$

The left part of $\mathbf{K}$ represents sensitivity to a change in the source intensity while the right part represents sensitivity to a location shift. If we assume $\begin{bmatrix} dI^s/I^s \\ d\mathbf{x}^s \end{bmatrix} \sim \mathcal{N}(\mathbf{0}, \mathbf{G})$ also follows Gaussian distribution with covariance matrix $\mathbf{G}$, from (3.13) we know that

$$\mathbf{K G K}^T = \mathbf{B}. \tag{4.37}$$

We can then solve for $\mathbf{G}$ by inverting the system,

$$\mathbf{G} = \left(\mathbf{K}^T\mathbf{K}\right)^{-1}\mathbf{K}^T\mathbf{K G K}^T\mathbf{K}\left(\mathbf{K}^T\mathbf{K}\right)^{-1} = \left(\mathbf{K}^T\mathbf{K}\right)^{-1}\mathbf{K}^T\mathbf{B K}\left(\mathbf{K}^T\mathbf{K}\right)^{-1}. \tag{4.38}$$

Especially when $\mathbf{B} = s_0^2\mathbf{I}$, we have $\mathbf{G} = s_0^2\left(\mathbf{K}^T\mathbf{K}\right)^{-1}$. A sample PDF of the reconstruction is shown in figure 4-7, the cloud from repeated experiments and the PDF from theoretical estimation are compared. Matrix $\mathbf{G}$ is a function of the source location. It contains the standard deviation of the sources parameters as diagonal elements, $\sqrt{G_{11}} = s_I$ is the standard deviation of the intensity uncertainty $\dfrac{\Delta I^s}{I^s}$, $\sqrt{G_{22}} = s_x$, $\sqrt{G_{33}} = s_y$, $\sqrt{G_{44}} = s_z$ are the standard deviations of the location uncertainty $\Delta\mathbf{x}^s$. Since these quantities are proportional to the standard deviation of the measurement, namely s_0, it become necessary to look at $\dfrac{s_I}{s_0}$, $\dfrac{s_x}{s_0}$, $\dfrac{s_y}{s_0}$, $\dfrac{s_z}{s_0}$ as measures of the difficulty for source identification.

4.3.2 Covariance matrix

It can be shown that if we use more and more ensemble members (or eigen sources of the system), the standard deviation of the source parameters will converge, as can be seen in figure 4-8 and 4-9. If we have a reaonable representation of the system by using enough eigen sources, we assume that $\mathbf{\Phi} \rightarrow \mathbf{\Phi}_F$, where $\mathbf{\Phi}_F$ contains all the eigen sources of the system. For example in the one-dimensional reconstruction case, from equation 4.36, matrix $\mathbf{K}^T\mathbf{K}$ can be approximated by,

$$\mathbf{K}^T\mathbf{K} \approx \frac{(I^s)^2}{\|M\|^2} \lim_{\Delta x \to 0} \begin{bmatrix} \mathbf{\Phi}_F\Big|_{\mathbf{x}^s} \mathbf{\Lambda}_F^2 \mathbf{\Phi}_F^T\Big|_{\mathbf{x}^s} & \mathbf{\Phi}_F\Big|_{\mathbf{x}^s} \mathbf{\Lambda}_F^2 \dfrac{\mathbf{\Phi}_F^T\Big|_{\mathbf{x}^s+\Delta x} - \mathbf{\Phi}_F^T\Big|_{\mathbf{x}^s}}{\Delta x} \\ \dfrac{\mathbf{\Phi}_F\Big|_{\mathbf{x}^s+\Delta x} - \mathbf{\Phi}_F\Big|_{\mathbf{x}^s}}{\Delta x} \mathbf{\Lambda}_F^2 \mathbf{\Phi}_F^T\Big|_{\mathbf{x}^s} & \dfrac{\mathbf{\Phi}_F\Big|_{\mathbf{x}^s+\Delta x} - \mathbf{\Phi}_F\Big|_{\mathbf{x}^s}}{\Delta x} \mathbf{\Lambda}_F^2 \dfrac{\mathbf{\Phi}_F^T\Big|_{\mathbf{x}^s+\Delta x} - \mathbf{\Phi}_F^T\Big|_{\mathbf{x}^s}}{\Delta x} \end{bmatrix} \tag{4.39}$$

Notice that $\mathbf{\Phi}_F\mathbf{\Lambda}_F^2\mathbf{\Phi}_F^T = \mathbf{A}^T\mathbf{A} = \mathbf{H} = N_T\overline{c(x^m;x_i)c(x^m;x_j)}$, different element of the matrix can be written in terms of scalar statistic, $H_{ij} = H_{ji} = N_T\overline{c(x^m;x_i)c(x^m;x_j)}$. For simplicity we can write,

$$\mathbf{\Phi}_F\Big|_{\mathbf{x}^s} \mathbf{\Lambda}_F^2 \mathbf{\Phi}_F^T\Big|_{\mathbf{x}^s} = N_T\overline{c(x^s)^2}, \quad \mathbf{\Phi}_F\Big|_{\mathbf{x}^s+\Delta x} \mathbf{\Lambda}_F^2 \mathbf{\Phi}_F^T\Big|_{\mathbf{x}^s+\Delta x} = N_T\overline{c(x^s+\Delta x)^2}. \tag{4.40}$$

Similarly,

$$\mathbf{\Phi}_F\Big|_{\mathbf{x}^s} \mathbf{\Lambda}_F^2 \mathbf{\Phi}_F^T\Big|_{\mathbf{x}^s+\Delta x} = N_T\overline{c(x^s)c(x^s+\Delta x)}. \tag{4.41}$$

Replacing $\|M\|_2$ with $I^s c(x^s)$, we have,

$$\mathbf{K}^T\mathbf{K} \approx \frac{N_T}{\overline{c(x^s)^2}} \lim_{\Delta x \to 0} \begin{bmatrix} \overline{c(x^s)^2} & \dfrac{\overline{c(x^s)c(x^s+\Delta x)} - \overline{c(x^s)^2}}{\Delta x} \\ \dfrac{\overline{c(x^s)c(x^s+\Delta x)} - \overline{c(x^s)^2}}{\Delta x} & \dfrac{\overline{c^2(x^s)} + \overline{c^2(x^s+\Delta x)} - 2\overline{c(x^s)c(x^s+\Delta x)}}{\Delta x^2} \end{bmatrix} \tag{4.42}$$

We define the shifting-source correlation coefficient as in chapter 2,

$$R(\Delta x) = \frac{\overline{c(x^s)c(x^s+\Delta x)}}{c_{rms}(x^s)c_{rms}(x^s+\Delta x)}, \tag{4.43}$$

and rewrite the expression as,

$$\left(\mathbf{K}^T\mathbf{K}\right)^{-1} \approx \frac{1}{N_T}\lim_{\Delta x\to 0}\begin{bmatrix} \frac{1+\frac{c_{rms}^2(x^s)}{c_{rms}^2(x^s+\Delta x)}-2\frac{c_{rms}(x^s)}{c_{rms}(x^s+\Delta x)}R}{1-R^2} & \frac{\frac{c_{rms}^2(x^s)}{c_{rms}^2(x^s+\Delta x)}-\frac{c_{rms}(x^s)}{c_{rms}(x^s+\Delta x)}R}{1-R^2}\Delta x \\ \frac{\frac{c_{rms}^2(x^s)}{c_{rms}^2(x^s+\Delta x)}-\frac{c_{rms}(x^s)}{c_{rms}(x^s+\Delta x)}R}{1-R^2}\Delta x & \frac{c_{rms}^2(x^s)}{c_{rms}^2(x^s+\Delta x)}\frac{\Delta x^2}{1-R^2} \end{bmatrix} \tag{4.44}$$

recognizing $\lim_{\Delta x\to 0}\frac{c_{rms}^2(x^s)}{c_{rms}^2(x^s+\Delta x)} = 1$, we have,

$$\sqrt{N_T}\frac{I^s}{s_0} = \lim_{\Delta x\to 0}\sqrt{\frac{1+\frac{c_{rms}^2(x^s)}{c_{rms}^2(x^s+\Delta x)}-2\frac{c_{rms}(x^s)}{c_{rms}(x^s+\Delta x)}R}{1-R^2}}, \quad \sqrt{N_T}\frac{s_{x^s}}{s_0} = \lim_{\Delta x\to 0}\frac{\Delta x}{\sqrt{1-R^2}} \tag{4.45}$$

From the previous derivation we can easily conclude that the eigenvalues $\mathbf{\Lambda}$ scale with $\sqrt{N_T}/$ Therefore, according to equation 4.36, matrix $\mathbf{K}$ scales with $\sqrt{N_T}$ and matrix $\mathbf{G}$ scales with N_T^{-1}. As a result, the standard deviation of the predicted parameters scale with $N_T^{-1/2}$. The N_T-dependency is verified in figure 4-6 using different N_T. Notice that $\lim_{\Delta x\to 0}\frac{\Delta x}{\sqrt{1-R^2}}$ can be regarded as a length scale from the shifting-source correlation coefficient.

$$\lambda_R = \lim_{\Delta x\to 0}\frac{\Delta x}{\sqrt{1-R^2}} \tag{4.46}$$

Notice that all these scalar statistics can be obtains by running two forward simulations from sources located at x^s and $x^s+\Delta x$ simultaneously, using the same velocity fields. We can collect these statistics and form matrix $\mathbf{K}$ at every possible sensor location, estimating the difficulty for different sensors to locate the source. The converged statistics are shown in figure 4-8 and 4-9 as dashed lines. If the y and z locations of the sources also need to be determined, we have to analyze matrix $\mathbf{K}$ as

$$\mathbf{K} = \mathbf{\Lambda}\left[\mathbf{\Phi}^T\Big|_{\mathbf{x}^s} \quad \frac{\partial\mathbf{\Phi}^T}{\partial x^s}\Big|_{\mathbf{x}^s} \quad \frac{\partial\mathbf{\Phi}^T}{\partial y^s}\Big|_{\mathbf{x}^s} \quad \frac{\partial\mathbf{\Phi}^T}{\partial z^s}\Big|_{\mathbf{x}^s}.\right] \tag{4.47}$$

Following a similar procedure, we can relate the matrix $\mathbf{K}^T\mathbf{K}$ with scalar statistics as follows,

$$\left(\mathbf{K}^T\mathbf{K}\right)_{11} = 1 \tag{4.48}$$

$$\left(\mathbf{K}^T\mathbf{K}\right)_{12} = \frac{\overline{c(\mathbf{x}^s)c(\mathbf{x}^s+\Delta x)} - \overline{c(\mathbf{x}^s)^2}}{\Delta x \overline{c(\mathbf{x}^s)^2}} \tag{4.49}$$

$$\left(\mathbf{K}^T\mathbf{K}\right)_{13} = \frac{\overline{c(\mathbf{x}^s)c(x^s+\Delta y)} - \overline{c(\mathbf{x}^s)^2}}{\Delta y\ \overline{c(\mathbf{x}^s)^2}} \tag{4.50}$$

$$\left(\mathbf{K}^T\mathbf{K}\right)_{14} = \frac{\overline{c(\mathbf{x}^s)c(\mathbf{x}^s+\Delta z)} - \overline{c(\mathbf{x}^s)^2}}{\Delta z\ \overline{c(\mathbf{x}^s)^2}} \tag{4.51}$$

$$\left(\mathbf{K}^T\mathbf{K}\right)_{22} = \frac{\overline{c^2(\mathbf{x}^s)} + \overline{c^2(\mathbf{x}^s+\Delta x)} - 2\overline{c(\mathbf{x}^s)c(\mathbf{x}^s+\Delta x)}}{\Delta x^2} \tag{4.52}$$

$$\left(\mathbf{K}^T\mathbf{K}\right)_{33} = \frac{\overline{c^2(\mathbf{x}^s)} + \overline{c^2(\mathbf{x}^s+\Delta y)} - 2\overline{c(\mathbf{x}^s)c(\mathbf{x}^s+\Delta y)}}{\Delta y^2} \tag{4.53}$$

$$\left(\mathbf{K}^T\mathbf{K}\right)_{44} = \frac{\overline{c^2(\mathbf{x}^s)} + \overline{c^2(\mathbf{x}^s+\Delta z)} - 2\overline{c(\mathbf{x}^s)c(\mathbf{x}^s+\Delta z)}}{\Delta z^2} \tag{4.54}$$

$$\left(\mathbf{K}^T\mathbf{K}\right)_{23} = \frac{\overline{c^2(\mathbf{x}^s)} + \overline{c(\mathbf{x}^s+\Delta x)c(\mathbf{x}^s+\Delta y)} - \overline{c(\mathbf{x}^s)c(\mathbf{x}^s+\Delta x)} - \overline{c(\mathbf{x}^s)c(\mathbf{x}^s+\Delta y)}}{\Delta x \Delta y} \tag{4.55}$$

$$\left(\mathbf{K}^T\mathbf{K}\right)_{24} = \frac{\overline{c^2(\mathbf{x}^s)} + \overline{c(\mathbf{x}^s+\Delta x)c(\mathbf{x}^s+\Delta z)} - \overline{c(\mathbf{x}^s)c(\mathbf{x}^s+\Delta x)} - \overline{c(\mathbf{x}^s)c(\mathbf{x}^s+\Delta z)}}{\Delta x \Delta z\ \overline{c^2(x^s)}} \tag{4.56}$$

$$\left(\mathbf{K}^T\mathbf{K}\right)_{34} = \frac{\overline{c^2(\mathbf{x}^s)} + \overline{c(\mathbf{x}^s+\Delta y)c(\mathbf{x}^s+\Delta z)} - \overline{c(\mathbf{x}^s)c(\mathbf{x}^s+\Delta y)} - \overline{c(\mathbf{x}^s)c(\mathbf{x}^s+\Delta z)}}{\Delta y \Delta z\ \overline{c^2(\mathbf{x}^s)}}. \tag{4.57}$$

In this case of three-dimensional reconstruction, the aforementioned statistics can be collected by running 4 scalar sources at (x^s, y^s, z^s), $(x^s+\Delta x, y^s, z^s)$, $(x^s, y^s+\Delta y, z^s)$ and $(x^s, y^s, z^s+\Delta z)$, respectively.

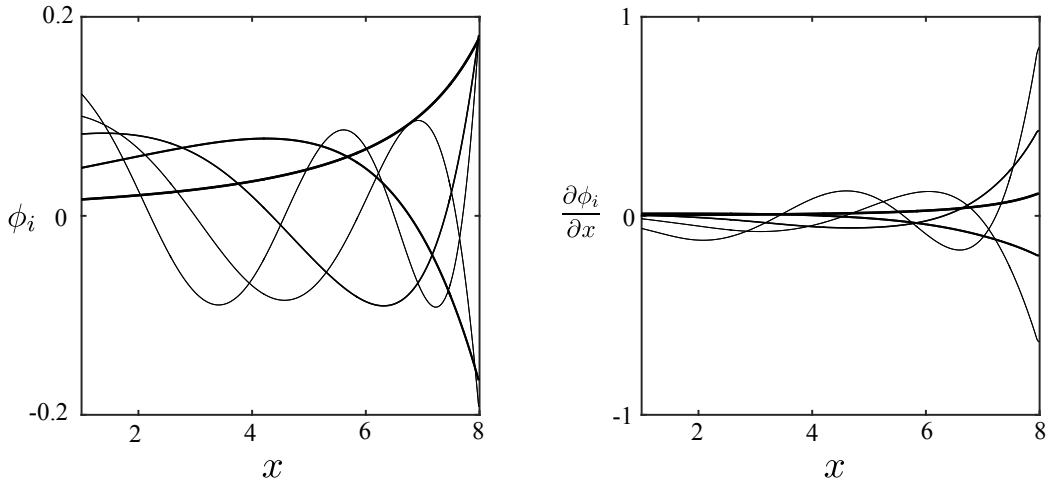

Figure 4-5. The leading 5 eigen sources (left) and their stream-wise gradient (right) for one-dimensional reconstruction in the channel center.

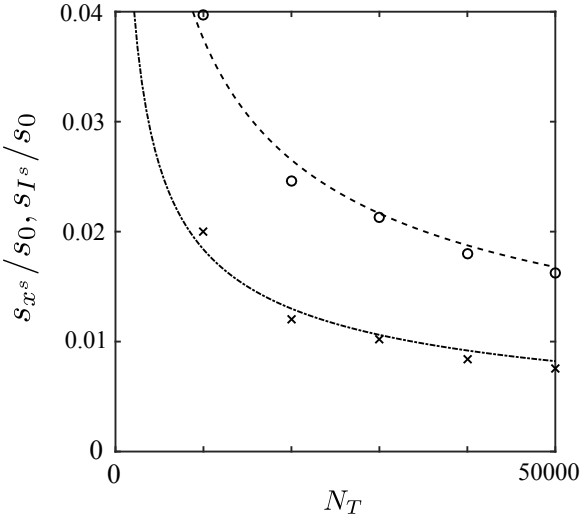

Figure 4-6. Validation of N_T-dependency of the standard deviation when trying to recover the source parameter with measurement noise. Dashed lines represent the $\sqrt{N_T}$ law.

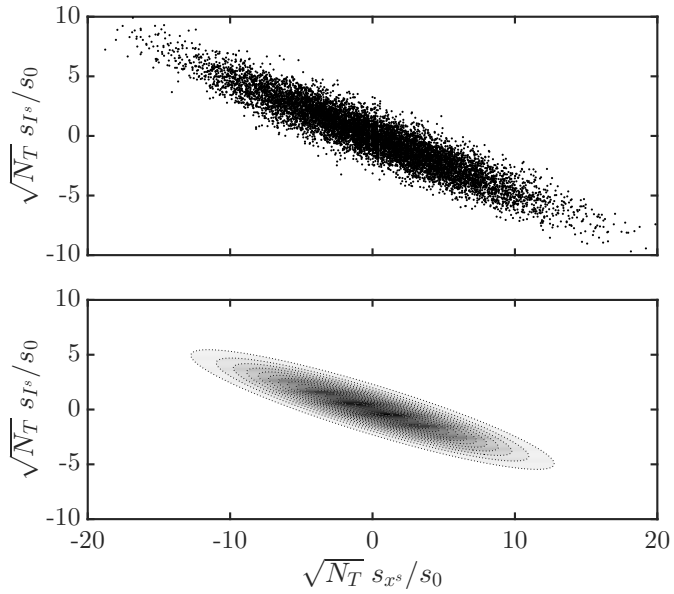

Figure 4-7. Top: the cloud of reconstructed source parameters with 20% measurement error using repeated experiments. Bottom: PDF of the source parameters predicted by theoretical analysis.

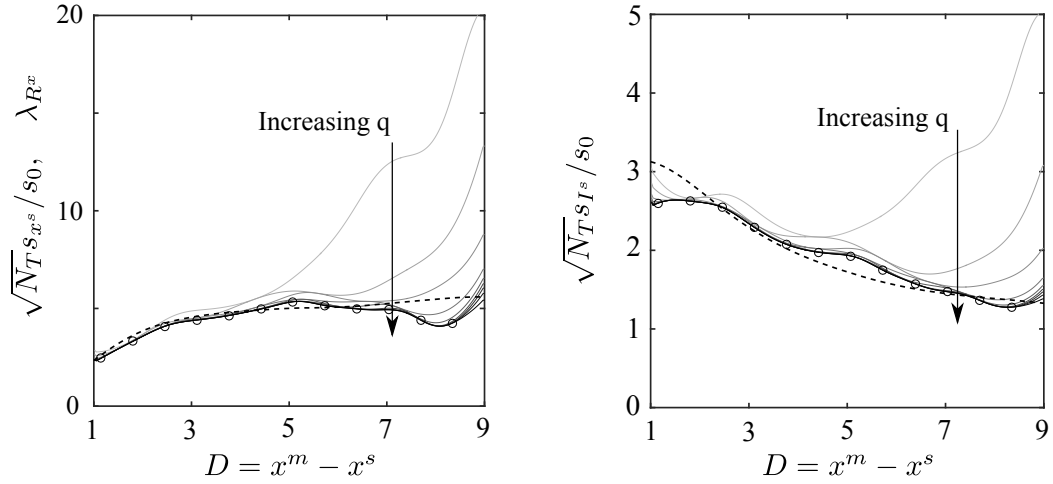

Figure 4-8. Standard deviation of Δx^s (left) and ΔI^s (right) when reconstructing the source parameters with measurement error. Thicker lines represents larger number of ensemble members N_{ens} from 3 to 11. Solid lines are estimated from calculating matrix $\mathbf{G}$ while circles are calculated by repeated experiment with measurement error with 11 ensemble members. Dashed lines represent converged statistics from a long forward simulation.

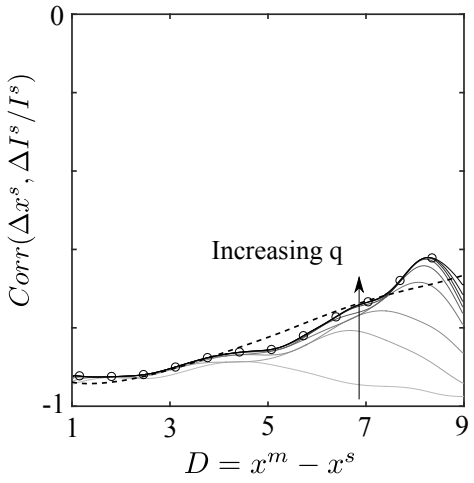

Figure 4-9. Correlation coefficient of Δx^s and ΔI^s when reconstructing the source parameters with measurement error. Thicker lines represents larger number of ensemble members N_{ens} from 3 to 11. Solid lines are estimated from calculating matrix $\mathbf{G}$ while circles are calculated by repeated experiment with measurement error with 11 ensemble members. Dashed lines represent converged statistics from a long forward simulation.

4.3.3 Different Sensor locations

By collecting the scalar statistics mentioned in the previous subsection, the difficulty at different sensor locations can be evaluated by simulating forward evolution of sources at a few different locations. In the previous chapter about optimal sensor placement, namely chapter 3, when the y and z location of the source is known and a one-dimensional search was to be conducted, the optimal sensor placement is not directly downstream of the source but rather on the edge of the plume. Now we have the tool of quantifying the difficulty of locating a source, the difficulty of the source inference of different positioning of the sensor can be evaluated. We will then evaluate this difficulty for both one-dimensional and three-dimensional reconstruction problems. Notice that essentially we only need matrix $\mathbf{G}$ at different sensor locations, and the matrix contains converged statistics that can be collected by running a few forward simulation, starting from source location $[x^s, y^s, z^s]$ and slightly shifted ones $[x^s + \Delta x^s, y^s, z^s], [x^s, y^s + \Delta y^s, z^s]$, and $[x^s, y^s, z^s + \Delta z^s]$.

4.3.3.1 One-dimensional reconstruction

When the y and z locations of the source is known, the goal becomes to identify x^s and I^s only. It has already been shown that the difficulty to locate the source in x direction is related to the length scalar λ_{R_x} defined from the shifting-source correlation coefficient in x direction. We show this statistics for different sensors on a cross-flow plane at a distance $D = 5$ from the true source. The results are plotted in figure 4-10. For a source in the channel center, a sensor on the edge is more sensitive to a change in the location of the source than a sensor directly downstream. For all other locations near the wall (log layer, buffer layer and sub layer), the sensor should be shifted towards the channel center in order to be more accurate to localize the source. Similar analysis can also be performed if only y or z location and intensity is unknown, then we would look at the length scale λ_{R_y} or λ_{R_z} defined from the shifting-source correlation coefficient in y or z direction. Those results are shown in figure 4-10 on the middle and right columns. It is worth noticing that while the difficulty in reconstructing y and z directions are much smaller than that in the x direction, they are less sensitive to sensor locations than reconstructing in the x direction.

4.3.3.2 Three-dimensional reconstruction

Now we focus on reconstructing the source location in all three directions. Matrix $\mathbf{K}$ is built at every sensor locations on the cross-flow plane with converged scalar statistics. Now matrix $\mathbf{G} = s_0(\mathbf{K}^T\mathbf{K})^{-1}$ is a 4×4 matrix, representing the covariance matrix of the error in four parameters, $[I^s, x^s, y^s, z^s]$ of the source,

$$\begin{bmatrix} dI/I^s \\ \Delta x^s \\ \Delta y^s \\ \Delta z^s \end{bmatrix} \sim \mathcal{N}(\mathbf{0}, \mathbf{G}) \tag{4.58}$$

We can eliminate the first row and column of the covariance matrix and focus on the location uncertainties, suppose $\mathbf{G}_l = \mathbf{G}(2:4, 2:4)$, for every general direction $\mathbf{d}$, the difficulty for the sensor to reconstruction the source in that direction can be

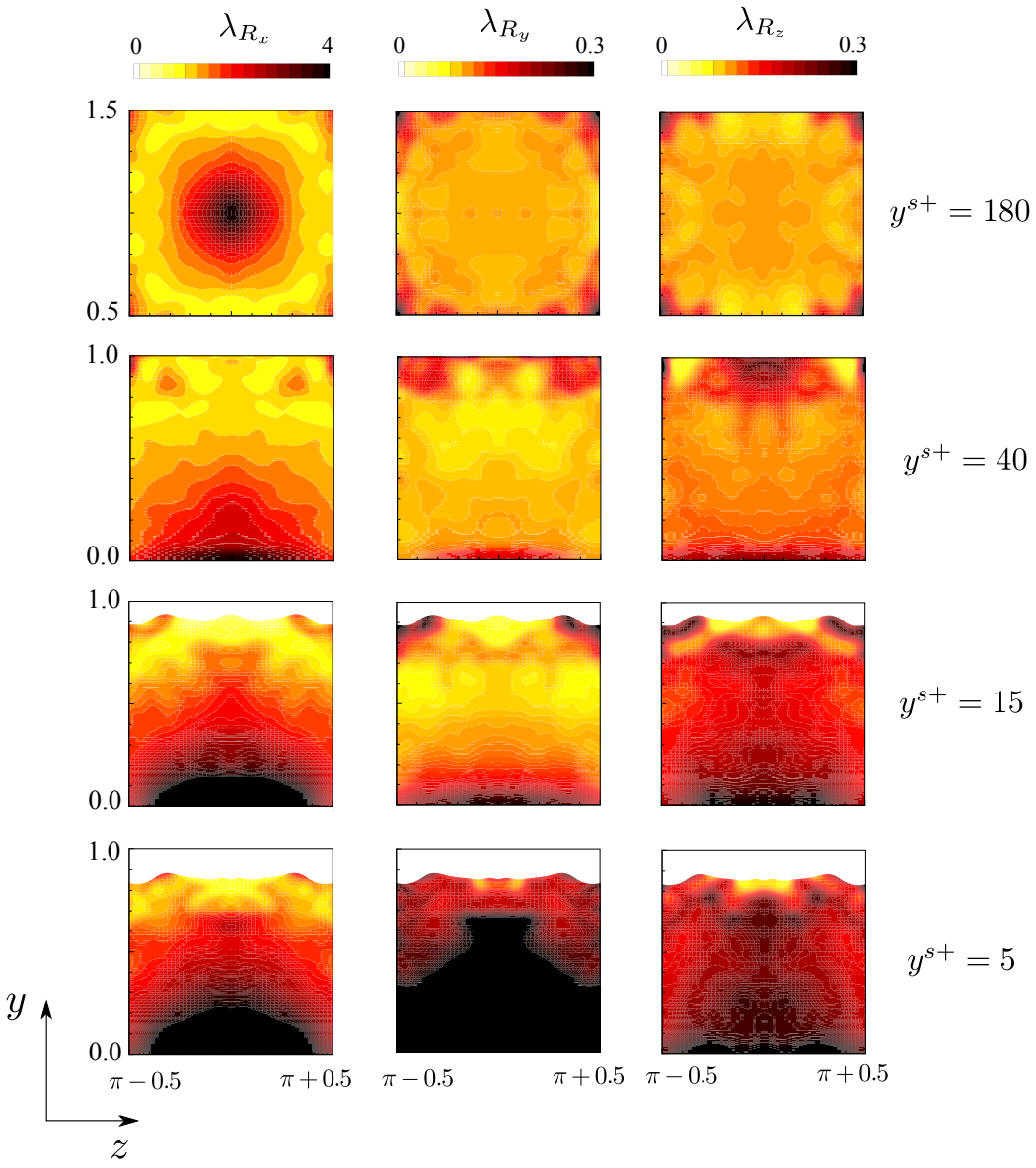

Figure 4-10. Length scale λ_{R_x} ,λ_{R_y} and λ_{R_z} for different sensors located at the cross-flow plane at a distance 5 from the source. For top to bottom the source is located at channel center ($y^{s+} = 180$), log layer ($y^{s+} = 40$), buffer layer ($y^{s+} = 15$) and sub layer ($y^{s+} = 5$).

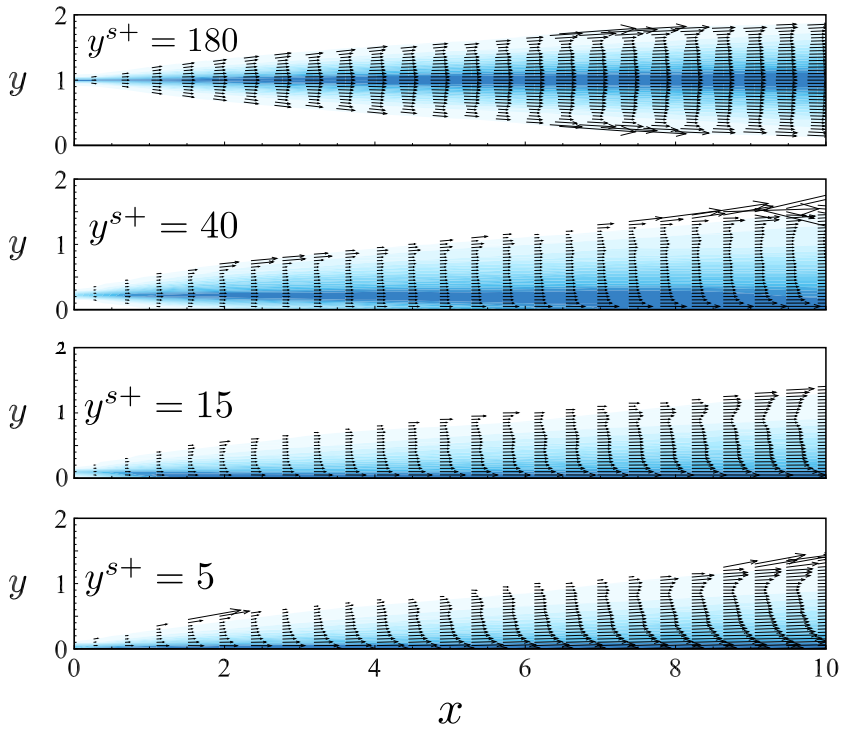

Figure 4-11. The most difficulty direction to reconstruct the source location $\mathbf{x}^s$ for different sensors. For top to bottom the source is located at channel center ($y^+ = 180$), log layer ($y^+ = 40$), buffer layer ($y^+ = 15$) and sub layer ($y^+ = 5$). The length of the vector is scale to be 5% of the largest eigen-value of local matrix $\mathbf{G}_l$. Contour plot shows the scalar field $c_{rms}/\max_{y,z} c_{rms}$

calculated as,

$$\Delta_d = \mathbf{d}^T \mathbf{G}_l \mathbf{d}. \tag{4.59}$$

The largest eigen vector and eigen value of matrix $\mathbf{G}_l$ represent the most difficulty direction to localize the source for a certain sensor and the corresponding standard deviation of the prediction in that direction. We plot this principle directions for different sensors and sources in figure 4-11. In all cases, regardless of the position of the source, the most difficulty direction to reconstruct is aligned with x-direction, which agrees with our findings in chapter 2. Nevertheless, a slight rotation of the principle directions can be observed on the edge of the plume, where reconstructing y location of the source becomes slightly more challenging than sensors directly downstream. Directly downstream of the source, the standard deviation for all sensors is

high. Meanwhile, outside the plume, the signal we receive become limited and thus standard deviation is also large. We also plotted the standard deviation of the source localization in x, y and z directions in figure 4-12.

It can be observed that this three-dimensional source localization are apparently harder in all directions than its corresponding one-dimensional problem, as shown previously in figure 4-10. This is within expectation because more parameters need to be determined in the three-dimensional search, which creates more inaccuracy when measurements are noisy. In the channel center it can be observed that if we want accurate prediction of y location of the source, it is better to align the sensor with the source to the same y location. The same trend can be identified in z direction. For x direction, it is better to put the sensor off the center. The results also implies that using sensors near the wall yields much worse results because signals are blurred by viscous effect and it become impossible to locate the source. Another important observation is that determining the determining the y-location of a source become more and more difficulty once the source is inside the viscous sublayer.

4.4 Multiple sources

We can now apply the method to multiple-source scenarios, as a simple example, we assume there are two sources and their x locations and intensity are unknown. Therefore we update the cost function as,

$$J(x_1^s, I_1^s, x_2^s, I_2^s) = \sum_i ||M^T M_i - \lambda_i \phi^{(i),T} \left(I_1^s \delta(x - x_1^s) + I_2^s \delta \left(x - x_2^s \right) \right) ||^2 \tag{4.60}$$

Notice there are four parameters to determine, namely $[I_1, I_2, x_1^s, x_2^s]$. We minimize this cost function with 7 leading eigen sources as ensemble members $\phi^{(i)}$. First a simple case was considered where the two sources are separated far away from each other ($I_1^s = 1, I_2^s = 1, x_1^s = 1.5, x_2^s = 8.5$). With 20% measurement error, the cloud of the source parameters are plotted in figure 4-13. The prediction for the location of the

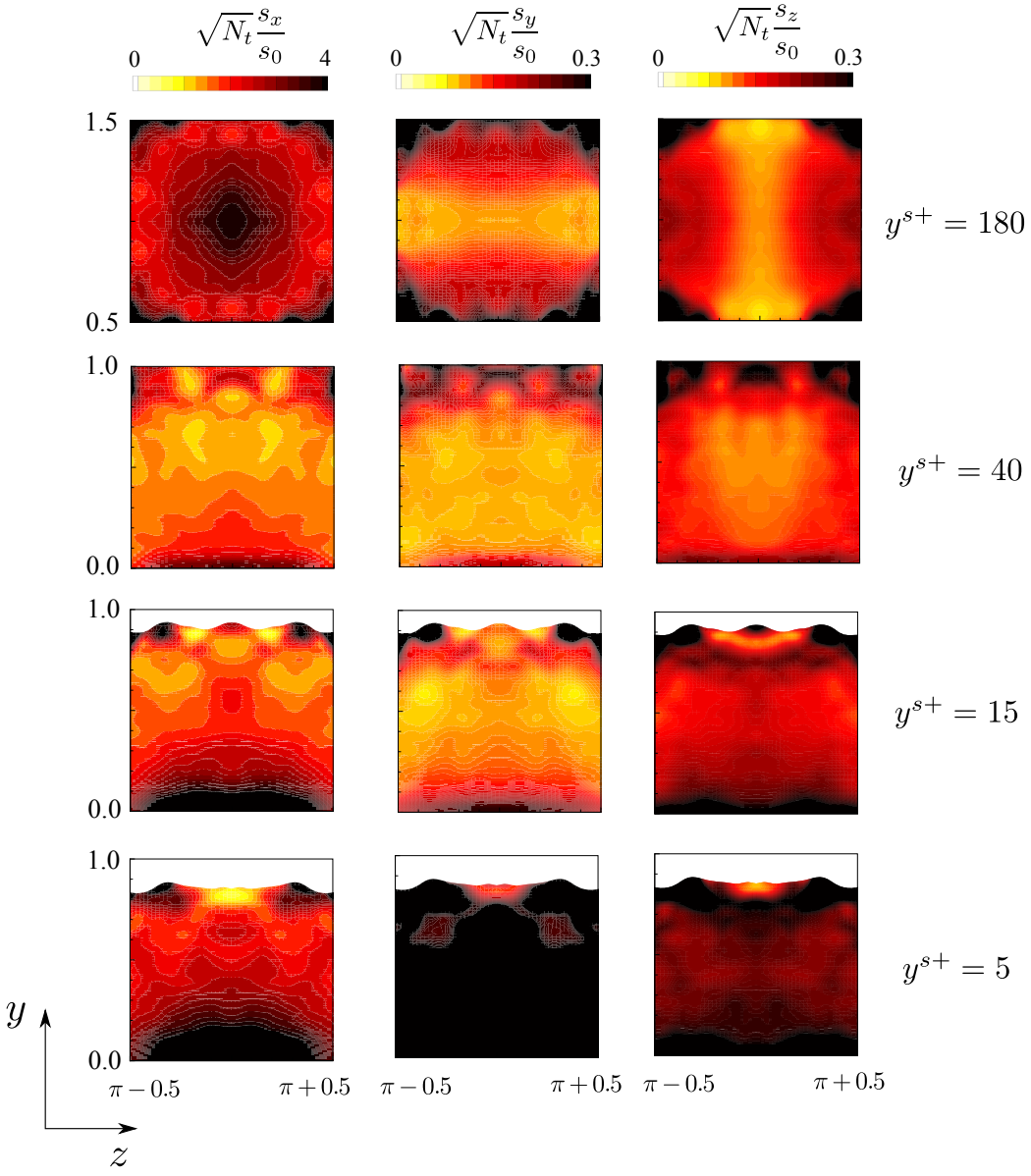

Figure 4-12. Standard deviation $\sqrt{N_T}\frac{s_x}{s_0}$,$\sqrt{N_T}\frac{s_y}{s_0}$ and $\sqrt{N_T}\frac{s_z}{s_0}$ for different sensors located at the cross-flow plane at a distance $D = 5$ from the source. For top to bottom, the source is located at channel center ($y^{s+} = 180$), log layer ($y^{s+} = 40$), buffer layer ($y^{s+} = 15$) and sub layer ($y^{s+} = 5$).

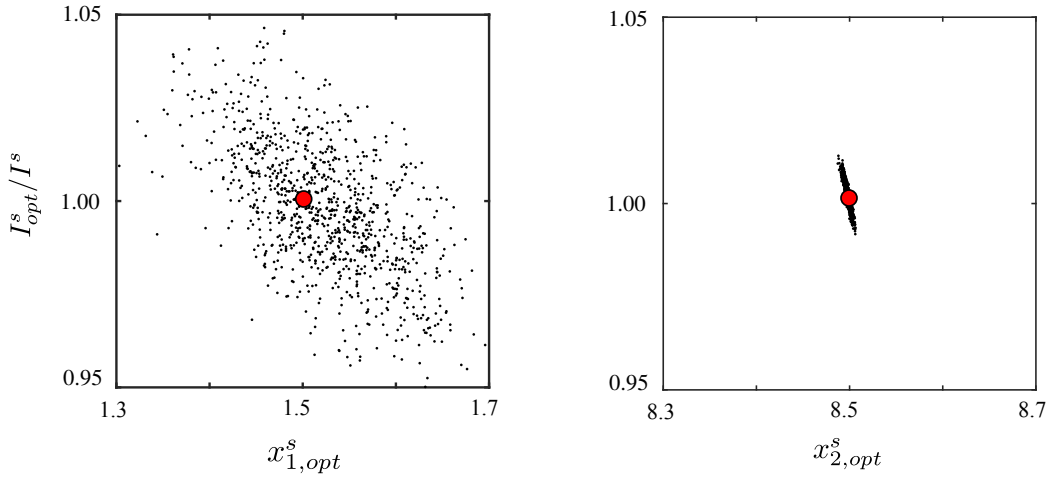

Figure 4-13. Sample Reconstruction of two source separated far away. The measurement data has 20% error. The true parameters are marked by the red dots.

source near the sensor ($x^m = 10$) has much better accuracy than that of the source far away. On the other hand, if the two sources are nearby ($I^s_1 = 1, I^s_2 = 1, x^s_1 = 4.5, x^s_2 = 5$), with 20% measurement error, the cloud of the reconstruction in figure 4-14 shows that it is very inaccurate to locate each of them. To further quantify the influence of two-source positioning onto the difficulty of the reconstruction, we can construct matrix $\mathbf{K}$ as follows,

$$\mathbf{K} = \frac{1}{\|M_1 + M_2\|}\mathbf{\Lambda}\left[I^s_1\mathbf{\Phi}^T\Big|_{\mathbf{x}^s_1} \quad I^s_1\frac{\partial\mathbf{\Phi}^T}{\partial x}\Big|_{\mathbf{x}^s_1} \quad I^s_2\mathbf{\Phi}^T\Big|_{\mathbf{x}^s_2} \quad I^s_2\frac{\partial\mathbf{\Phi}^T}{\partial x}\Big|_{\mathbf{x}^s_2}\right] \tag{4.61}$$

Then the standard deviation can be obtained for different source positioning. The results are plotted in figure 4-15. The contour plot of prediction error for x^s_1 and x^s_2 are shown as a function of different pairs of $[x^s_1, x^s_2]$. We can again verify that when two sources are nearby, it is very difficult to find each one of them. If they are far apart, the one near the sensor is going to be much easier to reconstruct then the one farther away.

4.5 Conclusion

An algorithm is proposed to quickly evaluate the location and intensity of a passive scalar source. The passive scalar source is localized and parameterized by its location

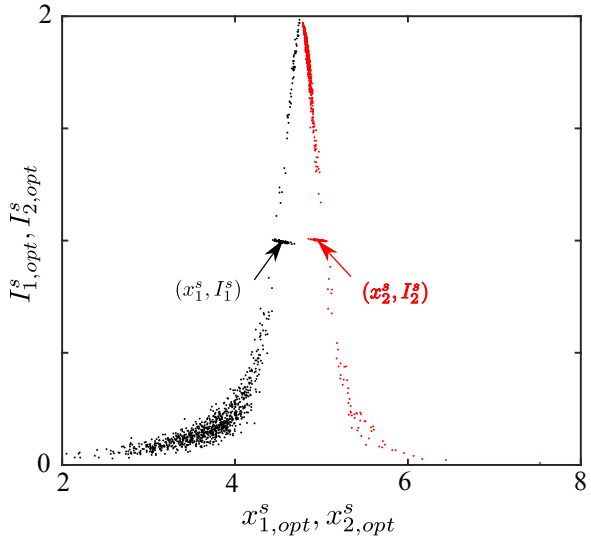

Figure 4-14. Sample Reconstruction of two source near each other. The measurement data has 20% error. The true parameters of the sources are marked by arrows.

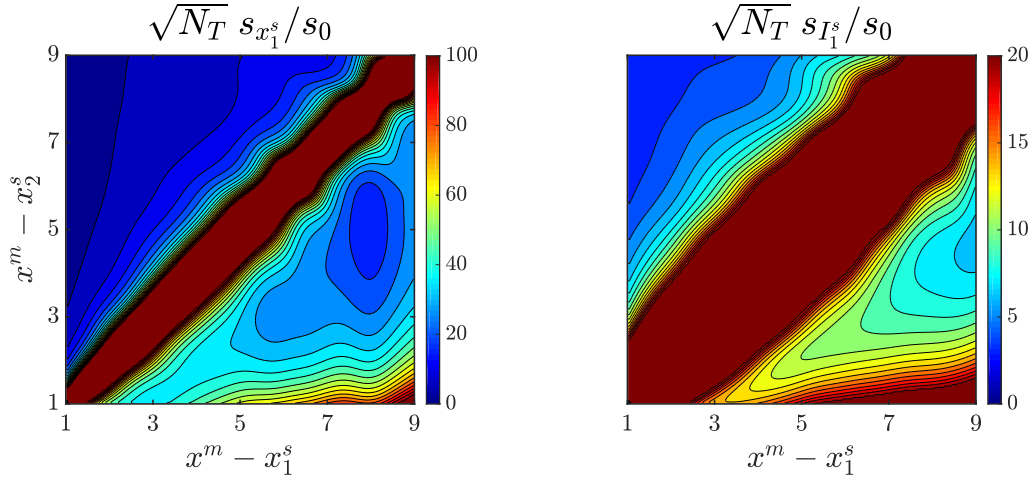

Figure 4-15. Standard deviation of $x^s_{1,opt}$ (left) and $I^s_{1,opt}$ (right) for reconstructing two sources located at x^s_1 and x^s_2 with the same intensity with measurement error.

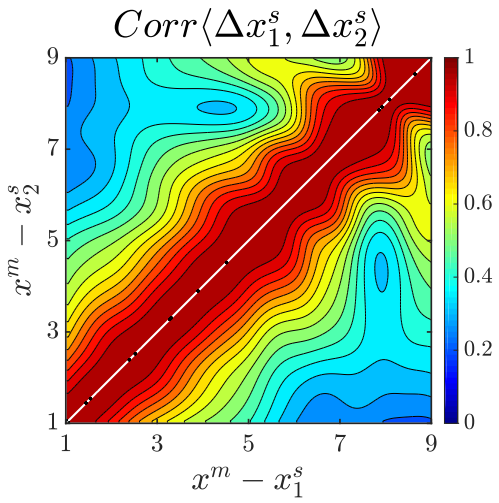

Figure 4-16. Correlation coefficient of Δx_1^s and Δx_2^s for reconstructing two sources located at x_1^s and x_2^s with the same intensity with measurement error.

and intensity. The algorithm utilized a proportionality relation when we project the true source onto eigen-sources and the measurement onto eigen-measurements. The projection of the true source onto the the eigen-sources and the projection of the measurement onto eigen-measurement are related by a proportionality given by the corresponding eigenvalue. The source parameters was selected by trying to match this proportionality. The biggest challenge for the proposed algorithm is to obtain an accurate prediction of the eigen-sources. To obtain the spectral information of the system, we perform forward simulations from an ensemble of trial-sources. Three options of trial-sources have been used and assessed: evenly distributed Gaussian profiles, eigen-source computed from historical data and historical eigen-source with a POD projection.

The POD procedure adopted to orthonormalize the resulting measurements from the trial sources can obtain more accurate estimation of eigen-sources and thusly yields the best results. By using a small number of trial sources, the location and intensity of the true source can be reconstructed. This method is also shown to retain high accuracy with noisy measurements if reasonable estimation of eigen-sources can be obtianed. Uncertainty quantification is done by putting white noise into the mea-

surements and evaluate the errors in the reconstructed source parameters. As more eigen sources are used in the process, the ratio of standard deviation of the reconstructed parameters over that in the measurements converges, revealing the fundamental difficulty of localizing the source. We tested sources located at different heights, namely $y^+ = \{180, 50, 15, 5\}$ and the sensor is directly downstream of the source. As the sensor moves away from the source, the location prediction is deteriorated while the intensity prediction is more accurate. By using a reasonable size of ensemble of trial sources, we can assume we have accurate representation of the "eigen-sources". This approximation of eigen-sources is especially effective in a diffusive system where the eigenvalue spectrum decays quickly and a few leading eigenvectors can delineate the behavior of the system accurately. A further perturbation analysis is conducted once we have measurement noise following a standard Gaussian distribution. The covariance matrix of the errors in the predicted source parameters can be evaluated. Mathematically this covariance matrix $\mathbf{G}$ is related to scalar field statistics that can be collected by running just a few forward simulations. Furthermore, we relate the fundamental difficulty of the one-dimensional source localization with a length scale encoded in the shifting-source correlation coefficient introduced earlier in this thesis. Finally, this eigen-ensemble-variational algorithm can be easily adopted to localize multiple sources simultaneously which yields great application values for pollution monitoring. However, a main drawback of the perturbation analysis is the assumption of perfect eigen-sources. Suggested future work includes the quantitative effect of imperfect eigen-sources onto the prediction error.

Chapter 5

Discussion and Conclusion

Olfactory search in turbulent environments is a difficult problem and several factors contribute together to this difficulty. The main reason is the combined effect of diffusion and turbulent dispersion, which is especially true in the setup to reconstruct a passive scalar source. We implemented the adjoint-variational approach to estimating the spatial distribution of the source from remote measurements. The problem is formulated as a constrained optimization, where we attempt to identify the source distribution whose nonlinear Navier-Stokes evolution leads to all the available measurements. Discrepancies between the model observations and the measurements define the cost function that we aim to minimize, and which features in the source term to the adjoint equations that are marched back in time. The outcome of one forward-adjoint loop is the gradient of the cost function, that we minimize using a gradient descent method. Throughout, we adopted a discrete adjoint in order to ensure that the forward-adjoint duality relation and the gradient of the cost function are computed to machine precision. Turbulent dispersion introduces strong non-linearity and breaks information into chaotic patterns while diffusion further smears out the ability to differentiate different values of the unknown state vector. In the channel center, the high correlation of scalar fields from different locations of source hinders the ability for our search algorithm to locate the true source. Near the viscous layer, the enhanced effect of diffusion blurs the signal, and reconstruction become very dif-

ficult. The quality of source localization is the best in the log layer, where the ratio of turbulent dispersion term and molecular diffusion term is the largest.

The ill-posedness of the problem is demonstrated by a quickly decaying eigenvalue spectrum of the Hessian matrix, by improving the spectrum, we successfully improved the quality of reconstruction with the same level of cost function drop. In order to minimize the condition number of the Hessian and search for the optimal sensor placement, we developed an iterative algorithm that tracks the principal eigenvectors of the Hessian. In the simplest scenario of a one-dimensional search with one sensor, the optimals sensor is found to be at the edge of the plume from the nearest source location. This is due to the fact that signals from different source locations are more de-correlated at the edge of the plume. Optimal sensor placement for a three-dimensional search shows that the algorithm is capable of separating initially clustered sensors. The eigenvectors of the Hessian for the optimal sensor is found to be more evenly distributed in space than the original placement. However, this indicates that the optimal placement is search-domain-dependent. It is not necessarily optimal for every possible source location in the search domain, but is the best option if the source could be anywhere inside the search domain.

To quantify the fundamental difficulty of identifying the source location and intensity, the source is parameterized by its location and intensity, source localization can be regarded as a low-dimensional optimization problem. The projection of the true source onto the the eigen-sources and the projection of the measurement onto eigen-measurement are related by a proportionality given by the corresponding eigenvalue. The source parameters was selected by trying to match this proportionality. In order to obtain an accurate prediction of the eigen-source and eigen-measurements, a series of forward simulations were performed with an ensemble of trial sources. In addition, a POD procedure is adopted to orthonormalize the resulting measurements from the trial sources and a more accurate estimation of eigen-sources can be

achieved. By using a small number of trial sources, the location and intensity of the true source can be reconstructed. This method is also shown to retain high accuracy with noisy measurements if reasonable estimation of eigen-sources can be obtained. Uncertainty quantification is done by putting white noise into the measurements and evaluate the errors in the reconstructed source parameters. The covariance matrix of the predicted source parameters are derived explicitly, which is then related to statistics of forward scalar fields. The fundamental difficulty of source localization in the vicinity of the true source is related to a length-scale defined by the shifting-source correlation coefficient. We further evaluated the covariance matrix by collecting the required statistics for different sensor locations. The difficulty of source identification was then calculated for different source and sensor arrangements. Furthermore, this eigen-ensemble-variational algorithm we developed can be easily adopted to locate multiple sources simultaneously and therefore yields great application values.

In summary, the current study provides efficient strategies to identify the spatial information of a scalar source release. We developed algorithms to reconstruct the spatial distribution of the source, optimize the sensor network as well as quickly identify the source location and intensity. The resulting data here not only provide physical interpretation of the feasibility as well as limitation in scalar-source identification in turbulent environments, but also established an important benchmark for future research on olfactory search in fully-developed turbulent scenarios.

Following the study provided in this thesis, future directions of study could be suggested as follows. Firstly, this work focus on the scenario where the scalar field is passive. In reality, both the atmosphere and the ocean, where most of the scalar source search is most valuable, are both subject to the effect of density or temperature stratification. Therefore, source identification in a stratified, fully turbulent environment would be of great interest. Moreover, most of the work, especially in chapter 2 and chapter 3, assumes detailed knowledge of the flow field, which is too expensive to

obtain in reality. Therefore, reconstructing the velocity fields from sensor signals of the scalar would also be a direction to further enhance the feasibility of our algorithm to real-world problems. In chapter 4 we developed an algorithm that only requires some historical data of the flow field and forward simulations (or experiments) in am expanding time horizon. The perturbation analysis presented in chapter 4 has the assumption of perfect eigen-sources. For real-world applications, one should also proceed by studying the quantitative effect of imperfect eigen-sources onto the prediction error, especially with minimum knowledge of the flow fields.

Appendices

Appendix

A.1 Discrete forward and adjoint equations

The variational algorithm that was developed in §2.2.2 relies on accurate solution of the forward and adjoint scalar fields. The discrete forms of these equations are derived in this appendix, and accuracy of the discrete forward-adjoint duality relation is verified to machine precision.

A.1.1 Discrete forward operator

Consider the forward advection-diffusion equation,

$$\frac{\partial c}{\partial t} + \mathbf{u}\cdot\nabla c = \frac{1}{Pe}\nabla^2 c + \phi. \tag{1}$$

with known velocity field $\mathbf{u}$. Integration over a finite volume V with surrounding surface S, and adopting Adams-Bashforth and Crank-Nicolson for temporal discretization of the advection and diffusion terms respectively, results in,

$$\begin{aligned}\underbrace{\frac{\delta c}{\Delta t} - \frac{1}{2VPe}\iint_S (\mathbf{n}\cdot\nabla\delta c)\,dS}_{\mathbf{D}\delta\mathbf{c}} \;=\; & -\frac{1}{2V}\left(3\underbrace{\left[\iint_S (\mathbf{u}\cdot\mathbf{n}c)\,dS\right]^n}_{\mathbf{F}^n\mathbf{c}^n} - \underbrace{\left[\iint_S (\mathbf{u}\cdot\mathbf{n}c)\,dS\right]^{n-1}}_{\mathbf{F}^{n-1}\mathbf{c}^{n-1}}\right) \\ & + \frac{1}{V}\underbrace{\left[\frac{1}{Pe}\iint_S (\mathbf{n}\cdot\nabla c)\,dS\right]^n}_{\mathbf{D}_{ex}\mathbf{c}^n} + \underbrace{\frac{1}{V}\left[\int_V \phi dV\right]^n}_{\phi^n}.\end{aligned} \tag{2}$$

Superscripts mark the index of the time step and $\delta c = c^{n+1} - c^n$. In each control volume, velocity components are staggered at cell faces and the scalar c is located at the cell centre. If we denote the east, west, south, north, back, front surfaces by their

initials, the integral terms associated with advection and diffusion can be expressed as:

$$\text{i:} \quad \iint_S (\mathbf{u}\cdot\mathbf{n}c)\,dS = u_e S_e c_e - u_w S_w c_w + u_n S_n c_n - u_s S_s c_s + u_b S_b c_b - u_f S_f c_f, \tag{3}$$

$$\text{ii:} \quad \frac{1}{Pe}\iint_S (\mathbf{n}\cdot\nabla c)\,dS \tag{4}$$
$$= \frac{1}{Pe}\left(S_e \left.\frac{\partial c}{\partial x}\right|_e - S_w \left.\frac{\partial c}{\partial x}\right|_w + S_n \left.\frac{\partial c}{\partial y}\right|_n - S_s \left.\frac{\partial c}{\partial y}\right|_s + S_b \left.\frac{\partial c}{\partial z}\right|_b - S_f \left.\frac{\partial c}{\partial z}\right|_f \right).$$

For succinctness, the fields c and δc are written as column vectors $\mathbf{c}$ and $\delta\mathbf{c}$, which enables a matrix representation of each term marked by an underbrace in equation (2). Matrix $\mathbf{D}$ contains the implicit diffusion term, while $\mathbf{F}$ and $\mathbf{D}_{ex}$ are the advection and explicit diffusion terms, respectively.

Numerical evaluation of the advection term $\mathbf{F}^n\mathbf{c}^n$ adopted an upwind scheme, where the scalar flux on one cell face (e.g. west) can be written as,

$$F_w c = \max\{S^x u, 0\} \times c^{w-} + min\{S^x u, 0\} \times c^{w+} = S^x\big(c^{w-}u^+ + c^{w+}u^-\big), \tag{5}$$

where the short-hand notations $u^+ = \max\{S^x u, 0\}$ and $u^- = \min\{S^x u, 0\}$ are the positive and negative parts of u velocity, respectively. A third-order upstream central scheme (HOUC3) algorithm is incorporated to interpolated the scalar concentration on the west and east faces using biased stencils,

$$\begin{aligned} c^{w-}_{(i,j,k)} &= \frac{-c_{(i-2,j,k)} + 5c_{(i-1,j,k)} + 2c_{(i,j,k)}}{6}, \quad & c^{w+}_{(i,j,k)} &= \frac{-c_{(i+1,j,k)} + 5c_{(i,j,k)} + 2c_{(i-1,j,k)}}{6}, \\ c^{e-}_{(i,j,k)} &= \frac{-c_{(i-1,j,k)} + 5c_{(i,j,k)} + 2c_{(i+1,j,k)}}{6}, \quad & c^{e+}_{(i,j,k)} &= \frac{-c_{(i+2,j,k)} + 5c_{(i+1,j,k)} + 2c_{(i,j,k)}}{6}. \end{aligned} \tag{6}$$

In cell (i,j,k), the scalar flux in x-direction, $(\mathbf{F}^x\mathbf{c})_{(i,j,k)}$ can be written as,

$$\begin{aligned} (\mathbf{F}^x\mathbf{c})_{(i,j,k)} &= F_w c + F_e c \\ &= S^x\left(c^{w-}_{(i,j,k)}u^+_{(i,j,k)} + c^{w+}_{(i,j,k)}u^-_{(i,j,k)} + c^{e-}_{(i,j,k)}u^+_{(i+1,j,k)} + c^{e+}_{(i,j,k)}u^-_{(i+1,j,k)}\right), \end{aligned} \tag{7}$$

and

$$\mathbf{F}^n = \mathbf{F}^x + \mathbf{F}^y + \mathbf{F}^z \tag{8}$$

contains evaluation of scalar flux in all three directions.

Solving the forward equation involves inverting the matrix $\mathbf{D}$, which contains the implicit diffusion term. The operator for implicit diffusion, $\mathbf{D}_{im}$ can be defined as,

$$-\frac{1}{V}\iint_S (\mathbf{n}\cdot\nabla\delta c)\,dS = \mathbf{V}^{-1}\mathbf{D}_{im}\delta\mathbf{c} = \mathbf{V}^{-1}\mathbf{D}_{im,x}\delta\mathbf{c} + \mathbf{V}^{-1}\mathbf{D}_{im,y}\delta\mathbf{c} + \mathbf{V}^{-1}\mathbf{D}_{im,z}\delta\mathbf{c}, \quad (9)$$

where $\mathbf{V}$ is the diagonal mass matrix whose entries are the volumes at each cell and $\mathbf{D}_{im,x} = -\iint_{S_e+S_w} (\mathbf{n}\cdot\nabla\delta c)\,dS$ is the diffusion term in x-direction, etc. One standard way of inverting $\mathbf{D} = \frac{1}{\Delta t}(\mathbf{I} + \frac{1}{2}\frac{\Delta t}{Pe}\mathbf{V}^{-1}\mathbf{D}_{im})$ is via the Alternating Direction Implicit (ADI) method. ADI approximates the original operator $\mathbf{D}$ by multiplication of implicit diffusion operators in three different dimensions, namely

$$\begin{aligned}\tilde{\mathbf{D}} &= \frac{1}{\Delta t}(\mathbf{I} + \frac{1}{2}\frac{\Delta t}{Pe}\mathbf{V}^{-1}\mathbf{D}_{im,x})(I + \frac{1}{2}\frac{\Delta t}{Pe}\mathbf{V}^{-1}\mathbf{D}_{im,y})(\mathbf{I} + \frac{1}{2}\frac{\Delta t}{Pe}\mathbf{V}^{-1}\mathbf{D}_{im,z}) \quad (10)\\ &= \frac{1}{\Delta t}\mathbf{D}_x\mathbf{D}_y\mathbf{D}_z.\end{aligned}$$

Each of these three operators yields a tri-diagonal system. Moreover, $\tilde{\mathbf{D}}^{-1} = \Delta t\mathbf{D}_z^{-1}\mathbf{D}_y^{-1}\mathbf{D}_x^{-1}$ represents solving three diagonal systems in the order (x, y, z).

By combining all the above terms, the discrete form of the forward scalar equation $\mathbf{L}c = \phi$ can be written as,

$$\mathbf{Lc} = \tilde{\mathbf{D}}\left(\mathbf{c}^{n+1} - \mathbf{c}^n\right) - \mathbf{V}^{-1}\left(\frac{3}{2}\mathbf{F}^n\mathbf{c}^n - \frac{1}{2}\mathbf{F}^{n-1}\mathbf{c}^{n-1} + \mathbf{D}_{ex}\mathbf{c}^n\right) = \boldsymbol{\phi}^n. \quad (11)$$

A.1.2 Discrete adjoint operator

The derivation of the discrete adjoint operator starts from the discrete form of the Lagrangian identify,

$$\langle \mathbf{Lc}, \mathbf{c}^* \rangle = \langle \mathbf{c}, \mathbf{L}^*\mathbf{c}^* \rangle, \quad (12)$$

where $\langle \mathbf{f}, \mathbf{g} \rangle = \int_0^T \mathbf{f}^T\mathbf{Vg}\ dt$ is the definition of the dot product of column vectors $\mathbf{f}$ and $\mathbf{g}$. In the above expression, $\mathbf{L}$ and $\mathbf{L}^*$ are the discrete forward and adjoint operators, $\mathbf{c}$ and $\mathbf{c}^*$ are column vectors of the forward and adjoint fields, and $\mathbf{V}$ is the

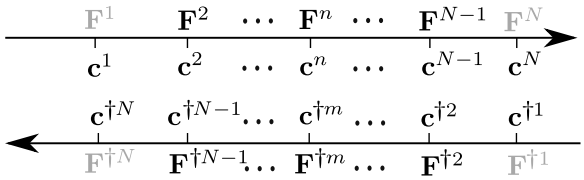

Figure A.1. Schematic for forward and adjoint time steps

diagonal matrix with the volume of the computational cells (i, j, k) as its elements. The relationship between $\mathbf{L}$ and $\mathbf{L}^*$ can be obtained from,

$$\langle \mathbf{Lc}, \mathbf{c}^* \rangle = \int_0^T \mathbf{c}^T \mathbf{L}^T \underbrace{\mathbf{V}\mathbf{c}^*}_{\mathbf{c}^\dagger} dt = \int_0^T \mathbf{c}^T \mathbf{V} \left(\mathbf{V}^{-1} \mathbf{L}^T \mathbf{V} \mathbf{c}^* \right) dt = \left\langle \mathbf{c}, \underbrace{\mathbf{V}^{-1} \mathbf{L}^T \mathbf{V}}_{\equiv \mathbf{L}^*} \mathbf{c}^* \right\rangle. \tag{13}$$

Also note that the above expression provides the governing equation for $\mathbf{c}^\dagger \equiv \mathbf{V}\mathbf{c}^*$ since the first equality can be written as,

$$\int_0^T \left(\mathbf{Lc}, \mathbf{c}^\dagger \right) dt = \int_0^T \left(\mathbf{c}, \mathbf{L}^T \mathbf{c}^\dagger \right) dt, \tag{14}$$

where $(\mathbf{f}, \mathbf{g}) = \mathbf{f}^T \mathbf{g}$ is the vector inner product. The expression (14) is the basis for the derivation of $\mathbf{L}^T$. The left-hand side is given by,

$$\int_0^T \left(\mathbf{Lc} \, , \, \mathbf{c}^\dagger \right) dt = \Delta t \sum_{n=1}^{N} \left(\tilde{\mathbf{D}} (\mathbf{c}^{n+1} - \mathbf{c}^n) - \mathbf{V}^{-1} \left(\frac{3}{2} \mathbf{F}^n \mathbf{c}^n - \frac{1}{2} \mathbf{F}^{n-1} \mathbf{c}^{n-1} + \mathbf{D}_{ex} \mathbf{c}^n \right), \; \mathbf{c}^{\dagger N+1-n} \right).$$

The summation over time index from 1 to N indicates the discrete integration in time. Note that the adjoint field $\mathbf{c}^\dagger$ is supposed to evolve backwards in time and an index $N + 1 - n$ is applied for the reverse time horizon. For simplicity, we denote this reverse time index $m = N + 1 - n$ and the reverse advection operator $\mathbf{F}^{\dagger m} = (\mathbf{F}^n)^T$. Figure A.1 shows the schematic for this change of index. The initial conditions are $\mathbf{c}^{n=1} = \mathbf{c}^{\dagger m=1} = \mathbf{0}$ for both the forward and adjoint simulations and, therefore, $\mathbf{F}^1 \mathbf{c}^1 = \mathbf{F}^{\dagger 1} \mathbf{c}^{\dagger 1} = \mathbf{0}$.

Equation (15) can be rewritten in the form of $\int_0^T (\mathbf{Lc}, \mathbf{c}^\dagger) \, dt = \int_0^T (\mathbf{c}, \mathbf{L^T} \mathbf{c}^\dagger) \, dt$, where the discrete form of $\mathbf{L}^T$ is the target of the derivation. The first right-hand side term of equation (15) can be reassembled as,

$$\Delta t \sum_{n=1}^{N} \left(\tilde{\mathbf{D}} \mathbf{c}^{n+1}, \; \mathbf{c}^{\dagger N+1-n} \right) = \Delta t \sum_{n=1}^{N} \left(\mathbf{c}^n, \; \tilde{\mathbf{D}}^T \mathbf{c}^{\dagger m+1} \right), \tag{15}$$

and the transpose of the advection term is,

$$\Delta t \sum_{n=1}^{N} \left(\mathbf{V}^{-1} \left(\frac{3}{2}\mathbf{F}^{n}\mathbf{c}^{n} \quad - \quad \frac{1}{2}\mathbf{F}^{n-1}\mathbf{c}^{n-1} \right),\ \mathbf{c}^{\dagger N+1-n} \right)$$
$$= \quad \Delta t \sum_{n=1}^{N} \left(\mathbf{c}^{n},\ \mathbf{F}^{\dagger m}\mathbf{V}^{-1} \left(\frac{3}{2}\mathbf{c}^{\dagger m} - \frac{1}{2}\mathbf{c}^{\dagger m-1} \right) \right). \tag{16}$$

Equation (15) is then re-written as,

$$\begin{aligned}
\int_0^T \left(\mathbf{L}\mathbf{c}, \mathbf{c}^{\dagger}\right) dt &= \Delta t \sum_{n=1}^{N} \left(\tilde{\mathbf{D}}(\mathbf{c}^{n+1} - \mathbf{c}^{n}) - \mathbf{V}^{-1} \left(\frac{3}{2}\mathbf{F}^{n}\mathbf{c}^{n} - \frac{1}{2}\mathbf{F}^{n-1}\mathbf{c}^{n-1} + \mathbf{D}_{ex}\mathbf{c}^{n} \right),\ \mathbf{c}^{\dagger N+1-n} \right) \\
&= \Delta t \sum_{n=1}^{N} \left(\mathbf{c}^{n},\ \underbrace{\tilde{\mathbf{D}}^{T}(\mathbf{c}^{\dagger m+1} - \mathbf{c}^{\dagger m}) - \left[\mathbf{F}^{\dagger m}\mathbf{V}^{-1} \left(\frac{3}{2}\mathbf{c}^{\dagger m} - \frac{1}{2}\mathbf{c}^{\dagger m-1} \right) + \mathbf{D}_{ex}^{T}\mathbf{V}^{-1}\mathbf{c}^{\dagger m} \right]}_{\mathbf{L}^{T}\mathbf{c}^{\dagger}} \right) \\
&= \int_0^T \left(\mathbf{c}, \mathbf{L}^{T}\mathbf{c}^{\dagger}\right) dt,
\end{aligned}$$

where $\mathbf{L}^{T}$ is the discrete adjoint operator and $\mathbf{F}^{\dagger m}$, $\tilde{\mathbf{D}}^{T}$ and $\mathbf{D}_{ex}^{T}$ are derived below.

A.1.2.1 Discrete adjoint for the advection operator

For demonstration of the derivation, it suffices to show the derivation of $\mathbf{F}^{\dagger m} = \left(\mathbf{F}^{n}\right)^{T}$ in x-direction. The scalar flux in x-direction, $\mathbf{F}^{x}\mathbf{c}$ was previously given by equation (7). In order to obtain the numerical transpose of $\mathbf{F}^{x}$, we evaluate $\left(\mathbf{F}^{x}\mathbf{c}\right)^{T}\tilde{\mathbf{c}}^{\dagger}$, where $\tilde{\mathbf{c}}^{\dagger}$ is a temporary state vector.

$$\begin{aligned}
\left(\mathbf{F}^{x}\mathbf{c}\right)^{T}\tilde{\mathbf{c}}^{\dagger} &= \sum_{i,j,k} S^{x} \left(c^{w-}_{(i,j,k)} u^{+}_{(i,j,k)} + c^{w+}_{(i,j,k)} u^{-}_{(i,j,k)} + c^{e-}_{(i,j,k)} u^{+}_{(i+1,j,k)} + c^{e+}_{(i,j,k)} u^{-}_{(i+1,j,k)} \right) \tilde{c}^{\dagger}_{(i,j,k)} \\
&= \sum_{i,j,k} \underbrace{S^{x} \left[\left(\tilde{c}^{\dagger}u^{+}\right)^{e+} + \left(\tilde{c}^{\dagger}u^{-}\right)^{e-} + \left(\tilde{c}^{\dagger}u^{+}\right)^{w+} + \left(\tilde{c}^{\dagger}u^{-}\right)^{w-} \right]}_{\left(\left(\mathbf{F}^{x}\right)^{T}\tilde{\mathbf{c}}^{\dagger}\right)_{(i,j,k)}} c_{(i,j,k)}. \\
&= \left[\left(\mathbf{F}^{x}\right)^{T}\tilde{\mathbf{c}}^{\dagger} \right]^{T} \mathbf{c}.
\end{aligned} \tag{17}$$

Moreover, the transpose to the upwind operator $\mathbf{F}^{n}$ is $\mathbf{F}^{\dagger m} = \left(\mathbf{F}^{x}\right)^{T} + \left(\mathbf{F}^{y}\right)^{T} + \left(\mathbf{F}^{z}\right)^{T}$.

A.1.2.2 Discrete adjoint operator for the diffusion term

For the implicit diffusion, detailed form of the matrix $\tilde{\mathbf{D}}$ was previously given by equation (10), which yields the transpose

$$\begin{aligned}\tilde{\mathbf{D}}^T &= \frac{1}{\Delta t}(I+\frac{1}{2}\frac{\Delta t}{Pe}\mathbf{D}_{im,z}^T\mathbf{V}^{-1})(I+\frac{1}{2}\frac{\Delta t}{Pe}\mathbf{D}_{im,y}^T\mathbf{V}^{-1})(\mathbf{I}+\frac{1}{2}\frac{\Delta t}{Pe}\mathbf{D}_{im,x}^T\mathbf{V}^{-1}) \\ &= \frac{1}{\Delta t}(I+\beta\mathbf{D}_{im,z}^T\mathbf{V}^{-1})(\mathbf{I}+\beta\mathbf{D}_{im,y}^T\mathbf{V}^{-1})(\mathbf{I}+\beta\mathbf{D}_{im,x}^T\mathbf{V}^{-1}).\end{aligned} \tag{18}$$

It can be demonstrated that the operator $\mathbf{D}_{im,x}$ is symmetric. The vector inner product of $\mathbf{D}_{im,x}\delta\mathbf{c}$ and a temporary state vector $\tilde{\mathbf{c}}^\dagger$ results in

$$\begin{aligned}&\left(\mathbf{D}_{im,x}\delta\mathbf{c}\right)^T\tilde{\mathbf{c}}^\dagger \\ =\ &\sum_{i,j,k}\left[-\frac{(S^x_{(j,k)})^2}{V_{(i-\frac{1}{2},j,k)}}\left(\delta c_{(i,j,k)}-\delta c_{(i-1,j,k)}\right)-\frac{(S^x_{(j,k)})^2}{V_{(i+\frac{1}{2},j,k)}}\left(\delta c_{(i,j,k)}-\delta c_{(i+1,j,k)}\right)\right]\tilde{c}^\dagger_{(i,j,k)} \\ =\ &\sum_{i,j,k}\left[-\frac{(S^x_{(j,k)})^2}{V_{(i-\frac{1}{2},j,k)}}\left(\tilde{c}^\dagger_{(i,j,k)}-\tilde{c}^\dagger_{(i-1,j,k)}\right)-\frac{(S^x_{(j,k)})^2}{V_{(i+\frac{1}{2},j,k)}}\left(\tilde{c}^\dagger_{(i,j,k)}-\tilde{c}^\dagger_{(i+1,j,k)}\right)\right]\delta c^\dagger_{(i,j,k)} \\ =\ &\left(\mathbf{D}_{im,x}\tilde{\mathbf{c}}^\dagger\right)^T\delta\mathbf{c}\end{aligned} \tag{19}$$

Therefore $\mathbf{D}_{im,x}^T = \mathbf{D}_{im,x}$. Note that for a Cartesian mesh, the cell face whose normal is in the x-direction, S^x, is independent of index i and can be written as $S^x_{(j,k)}$. Similarly $S^y_{(i,k)}$ and $S^z_{(i,j)}$ can be defined in the other two directions. Thusly this procedure can also be done for $\mathbf{D}_{im,y}$, $\mathbf{D}_{im,z}$ and $\mathbf{D}_{ex}$ to demonstrate that they are all symmetric matrices.

As a result, equation (18) becomes

$$\begin{aligned}\tilde{\mathbf{D}}^T &= \frac{1}{\Delta t}\left(I+\frac{1}{2}\frac{\Delta t}{Pe}\mathbf{D}_{im,z}\mathbf{V}^{-1}\right)\left(I+\frac{1}{2}\frac{\Delta t}{Pe}\mathbf{D}_{im,y}\mathbf{V}^{-1}\right)\left(I+\frac{1}{2}\frac{\Delta t}{Pe}\mathbf{D}_{im,x}\mathbf{V}^{-1}\right) \\ &= \frac{1}{\Delta t}\left(\mathbf{I}+\beta\mathbf{D}_{im,z}\mathbf{V}^{-1}\right)\left(I+\beta\mathbf{D}_{im,y}\mathbf{V}^{-1}\right)\left(I+\beta\mathbf{D}_{im,x}\mathbf{V}^{-1}\right) \\ &= \frac{1}{\Delta t}\mathbf{V}\mathbf{D}_z\mathbf{D}_y\mathbf{D}_x\mathbf{V}^{-1}.\end{aligned} \tag{20}$$

Equation (20) indicates an inverse order of three tri-diagonal solvers in the discrete adjoint, which is the only difference from the forward operator $\tilde{\mathbf{D}}$. The final form of

the discrete adjoint operator is then,

$$\mathbf{L}^T\mathbf{c}^\dagger = \frac{1}{\Delta t}\mathbf{V}\mathbf{D}_z\mathbf{D}_y\mathbf{D}_x\mathbf{V}^{-1}\left(\mathbf{c}^{\dagger m+1} - \mathbf{c}^{\dagger m}\right) - \mathbf{F}^{\dagger m}\mathbf{V}^{-1}\left(\frac{3}{2}\mathbf{c}^{\dagger m} - \frac{1}{2}\mathbf{c}^{\dagger m-1}\right) - \mathbf{D}_{ex}\mathbf{V}^{-1}\mathbf{c}^{\dagger m}. \quad (21)$$

In addition to the above derivation of the discrete adjoint operator, we also note that the source term of c^* and $c^\dagger$ are related. From the governing equation of the former,

$$\mathbf{V}^{-1}\mathbf{L}^T\mathbf{V}\mathbf{c}^* = \epsilon(t)\delta(\mathbf{x} - \mathbf{x}^m). \quad (22)$$

dot product with $\mathbf{V}$ yields,

$$\mathbf{L}^T\mathbf{c}^\dagger = \epsilon(t)\mathbf{e}(\mathbf{x}^m). \quad (23)$$

where $\mathbf{e}(\mathbf{x}^m)$ is a column vector with entries equal to unity for computational cells with coordinates $\mathbf{x}^m$ and zero elsewhere.

A.1.2.3 Validation of the discrete adjoint algorithm

Validation of the discrete adjoint implementation is performed by verifying the forward-adjoint duality relation,

$$c(\mathbf{x}^m, t^m) = c^*(\mathbf{x}^s, t^s), \quad (2.8)$$

where c and c^* are the impulse responses to point sources $\delta(\mathbf{x^s}, t^s)$ and $\delta(\mathbf{x^m}, t^m)$ in the forward and adjoint equations, respectively. The duality relation was verified for different pairs of $(\mathbf{x^s}, t^s)$ and $(\mathbf{x^m}, t^m)$, and the result are reported in figure A.2. The left panel shows the agreement of $c(\mathbf{x}^m, t^m)$ and $c^*(\mathbf{x}^s, t^s)$ at $y^+ = 15$ and four values of the source-sensor separations, $D = x^m - x^s = \{2, 4, 6, 8\}$. In the right panel, the error is quantified using the normalized root-mean-square difference between the forward and adjoint concentrations, $\left(c(\mathbf{x}^m, t^m) - c^*(\mathbf{x}^s, t^s)\right)_{rms} / c_{rms}(\mathbf{x}^m, t^m)$, from five independent verifications of the duality relation. The error is reported at four heights in the channel, $y^+ = \{5, 15, 40, 180\}$, and various values of D. The results demonstrate that the forward-adjoint duality relation is satisfied to within machine precision for all the considered source-sensor pairs.

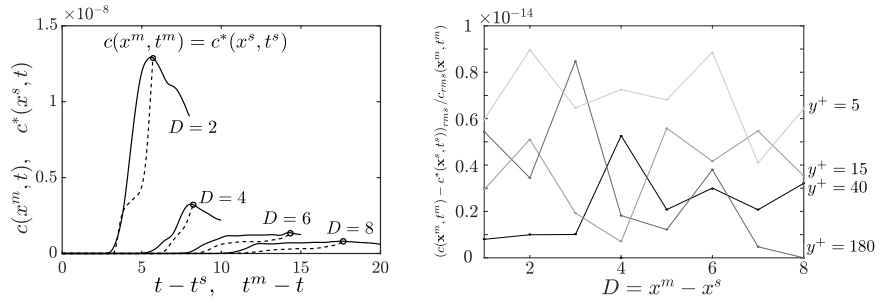

Figure A.2. Left: Comparison of the forward field $c(\mathbf{x}^m, t)$ from an impulse at $(\mathbf{x}^s, t^s)$ and adjoint field $c^*(\mathbf{x}^s, t)$ from an impulse at $(\mathbf{x}^m, t^m)$. The source-sensor pairs are located at $y^+ = 15$ and separated by streamwise distances $D = \{2, 4, 6, 8\}$. Right: Normalized root-mean-square error between $c(\mathbf{x}^m, t^m)$ and $c^*(\mathbf{x}^s, t^s)$ for source-sensor pairs at different wall-normal heights (light to dark $y^+ = \{5, 15, 40, 180\}$) and separations D.

B.2 Shifting source and sensor correlations coefficients

B.2.1 Adjoint algorithm for shifting-source correlation

In §2.4.2, the correlation coefficent in the measurements from two streamwise adjacent sources was defined as,

$$R^s_{MM}(\Delta x^s, \Delta t^m; D) = \frac{\frac{1}{T}\int_0^T c(\mathbf{x}^m, t; \mathbf{x}^s) c\left(\mathbf{x}^m, t + \Delta t^m; \mathbf{x}^s + \Delta x^s \mathbf{e}_x\right) dt}{c_{rms}(\mathbf{x}^m, t; \mathbf{x}^s)\, c_{rms}\left(\mathbf{x}^m, t + \Delta t^m; \mathbf{x}^s + \Delta x^s \mathbf{e}_x\right)}. \tag{24}$$

Evaluation of (24) requires multiple forward simulations are required, one for each new source position, which is computationally expensive. A new adjoint-based algorithm is derived in order to evaluate $R^s_{MM}(\Delta x^s)$ from a single forward-adjoint loop, when $\Delta t^m = 0$ which was shown to be valid for the present configuration.

The numerator can be expressed as,

$$\frac{1}{T}\int_t c(\mathbf{x}^m, t; \mathbf{x}^s)\, c(\mathbf{x}^m, t; \mathbf{x}^s + \Delta\mathbf{x}) dt = \frac{1}{T}\int_t \left(\int_\tau G^*(\mathbf{x}^s + \Delta\mathbf{x}, \tau; \mathbf{x}^m, t) d\tau \right) c(\mathbf{x}^m, t; \mathbf{x}^s) dt \tag{25}$$

where $G^* \equiv \mathbf{L}^{*-1}\delta(\mathbf{x} - \mathbf{x}^m)\delta(t - t^m)$ is the adjoint Greens function. In terms of the dot

product $\langle f, g \rangle \equiv \int_0^T \int_V f g dV dt$, the above expression becomes,

$$\frac{1}{T}\int_t c(\mathbf{x}^m, t; \mathbf{x}^s) c(\mathbf{x}^m, t; \mathbf{x}^s + \Delta\mathbf{x}) dt \tag{26}$$

$$= \frac{1}{T}\left\langle \int_\tau G^*(\mathbf{x}, \tau; \mathbf{x}^m, t) c(\mathbf{x}^m, t; \mathbf{x}^s) d\tau,\ \delta(\mathbf{x} - \mathbf{x}^s - \Delta\mathbf{x}) \right\rangle$$

$$= \frac{1}{T}\left\langle \int_\tau \mathbf{L}^{*-1}\left(\delta(\mathbf{x} - \mathbf{x}^m)\delta(t - \tau)\right) c(\mathbf{x}^m, t; \mathbf{x}^s) d\tau,\ \delta(\mathbf{x} - \mathbf{x}^s - \Delta\mathbf{x}) \right\rangle$$

$$= \frac{1}{T}\left\langle \mathbf{L}^{*-1}\left(\delta(\mathbf{x} - \mathbf{x}^m) c(\mathbf{x}^m, t; \mathbf{x}^s)\right),\ \delta(\mathbf{x} - \mathbf{x}^s - \Delta\mathbf{x}) \right\rangle \tag{27}$$

The correlation is therefore computed using the following procedure: (i) Perform a forward simulation using the source term $\delta(\mathbf{x} - \mathbf{x}^s)$ and evaluate the measurements at $\mathbf{x}^m$ to obtain $c(\mathbf{x}^m, t; \mathbf{x}^s)$. (ii) Perform an adjoint simulation using the source term $\delta(\mathbf{x} - \mathbf{x}^m) c(\mathbf{x}^m, t; \mathbf{x}^s)$ and evaluate the right hand side of (27), namely the integral of the adjoint field at $\mathbf{x}^s + \Delta\mathbf{x}$. Normalization of the result using the forward scalar variance yields the correlation coefficient.

B.2.2 Taylor's Hypothesis for scalar field

The correlation coefficients of measurements from two adjacent sensors $R^m_{MM}(\Delta x^m, \Delta t^m)$ (c.f. equation 2.25) can be related to that from two adjacent sources $R^s_{MM}(\Delta x^s, \Delta t^m)$ (c.f. equation 2.26), where the spatial displacements are assumed to be in the streamwise direction, $\Delta\mathbf{x} = \Delta x\ \mathbf{e}_x$. The connection between R^m_{MM} and R^s_{MM} relies on an assumption that Taylor's hypothesis is applicable to the velocity field,

$$\mathbf{u}\left(\mathbf{x}, t + \frac{\Delta x}{\mathcal{U}}\right) = \mathbf{u}\left(\mathbf{x} - \Delta\mathbf{x}, t\right), \tag{28}$$

where $\mathcal{U}$ is the streamwise advection velocity.

The scalar fields due to two sources shifted with respect to one another in the streamwise direction by $\Delta\mathbf{x} = \Delta x\ \mathbf{e}_x$ are governed by,

$$\frac{\partial c_1}{\partial t} + \mathbf{u}(\mathbf{x}, t) \cdot \nabla c_1 - \frac{1}{Pe}\nabla^2 c_1 = \delta(\mathbf{x} - \mathbf{x}^s), \tag{29}$$

$$\frac{\partial c_2}{\partial t} + \mathbf{u}(\mathbf{x}, t) \cdot \nabla c_2 - \frac{1}{Pe}\nabla^2 c_2 = \delta(\mathbf{x} - \mathbf{x}^s - \Delta\mathbf{x}). \tag{30}$$

The second equation is recast in terms of $\mathbf{x}' = \mathbf{x} - \Delta\mathbf{x}$ and $\nabla' = \nabla_{\mathbf{x}'}$, and after invoking Taylor's hypothesis,

$$\frac{\partial c_2(\mathbf{x}' + \Delta\mathbf{x}, t)}{\partial t} + \mathbf{u}(\mathbf{x}', t - \frac{\Delta x}{\mathcal{U}})\nabla' c_2(\mathbf{x}' + \Delta\mathbf{x}, t) - \frac{1}{Pe}\nabla'^2 c_2(\mathbf{x}' + \Delta\mathbf{x}, t) = \delta(\mathbf{x}' - \mathbf{x}^s). \quad (31)$$

Let $t' = t - \frac{\Delta x}{\mathcal{U}}$ and denote $c'(\mathbf{x}', t') \equiv c\left(\mathbf{x}' + \Delta\mathbf{x}, t' + \frac{\Delta x}{\mathcal{U}}\right)$, then

$$\frac{\partial c_2'(\mathbf{x}', t')}{\partial t'} + \mathbf{u}(\mathbf{x}', t')\nabla' c_2'(\mathbf{x}', t') - \frac{1}{Pe}\nabla'^2 c_2'(\mathbf{x}', t') = \delta(\mathbf{x}' - \mathbf{x}^s), \quad (32)$$

which is identical to the governing equation for a source at $\mathbf{x}^s$, and therefore $\mathbf{x}'$ can be replaced in by $\mathbf{x}$. As a result,

$$c_2'(\mathbf{x}, t) \equiv c_2\left(\mathbf{x} + \Delta\mathbf{x}, t + \frac{\Delta x}{\mathcal{U}}\right) = c_1(\mathbf{x}, t), \quad (33)$$

or equivalently,

$$c_2(\mathbf{x}^m, t) = c_1(\mathbf{x}^m - \Delta\mathbf{x}, t - \frac{\Delta x}{\mathcal{U}}). \quad (34)$$

The result of equation (34) indicates that the scalar plume starting from a different source location would still undergo the same flow structure in a frame shifted in space and time, which is a direct conclusion from Taylor's frozen eddy hypothesis.

The shifting-sensor correlation coefficient with the optimal time shift can be evaluated based on c_1 alone,

$$R^m_{MM}(-\Delta x, -\frac{\Delta x}{\mathcal{U}}) = \frac{\int_{t^m} c_1(\mathbf{x}^m, t^m) c_1(\mathbf{x}^m - \Delta\mathbf{x}, t^m - \frac{\Delta x}{\mathcal{U}}) dt^m}{\sqrt{\int_{t^m} c_1^2(\mathbf{x}^m, t^m) dt^m \int_{t^m} c_1^2(\mathbf{x}^m - \Delta\mathbf{x}, t^m - \frac{\Delta x}{\mathcal{U}}) dt^m}}. \quad (35)$$

Given that c_2 represents scalar plume from a source located at $\mathbf{x}^s + \Delta\mathbf{x}$, for arbitrary Δx, the shifting-source correlation can be written as,

$$R^s_{MM}(\Delta x, 0) = \frac{\int_{t^m} c_1(\mathbf{x}^m, t^m) c_2(\mathbf{x}^m, t^m) dt^m}{\sqrt{\int_{t^m} c_1^2(\mathbf{x}^m, t^m) dt^m \int_{t^m} c_2^2(\mathbf{x}^m, t^m) dt^m}}. \quad (36)$$

Comparing equations (35) and (36), and invoking the relation (34), yields

$$R^m_{MM}(-\Delta x, -\frac{\Delta x}{\mathcal{U}}) = R^s_{MM}(\Delta x, 0). \quad (37)$$

References

1. Jerrett, M. Atmospheric science: The death toll from air-pollution sources. *Nature* **525,** 330–331 (2015).
2. Nyberg, F. *et al.* Urban air pollution and lung cancer in Stockholm. *Epidemiology,* 487–495 (2000).
3. Lorenc, A. C. *Atmospheric data assimilation* (Meteorological Office, 1995).
4. Keats, A., Yee, E. & Lien, F.-S. Bayesian inference for source determination with applications to a complex urban environment. *Atmospheric environment* **41,** 465–479 (2007).
5. Cerizza, D., Sekiguchi, W., Tsukahara, T., Zaki, T. A. & Hasegawa, Y. Reconstruction of Scalar Source Intensity Based on Sensor Signal in Turbulent Channel Flow. *Flow, Turbulence and Combustion* **97,** 1211–1233 (2016).
6. Wang, Q., Hasegawa, Y. & Zaki, T. A. Spatial reconstruction of steady scalar sources from remote measurements in turbulent flow. *Journal of Fluid Mechanics* **870,** 316–352 (2019).
7. Wang, M., Wang, Q. & Zaki, T. A. Discrete adjoint of fractional-step incompressible Navier-Stokes solver in curvilinear coordinates and application to data assimilation. *Journal of Computational Physics* (2019).
8. Zhang, L. *et al.* An adjoint sensitivity analysis and 4D-Var data assimilation study of Texas air quality. *Atmospheric Environment* **42,** 5787–5804 (2008).
9. Bannister, R. A review of operational methods of variational and ensemble-variational data assimilation. *Quarterly Journal of the Royal Meteorological Society* **143,** 607–633 (2017).
10. Buehner, M., Morneau, J. & Charette, C. Four-dimensional ensemble-variational data assimilation for global deterministic weather prediction. *Nonlinear Processes in Geophysics* **20** (2013).
11. Mons, V., Wang, Q. & Zaki, T. A. Kriging-enhanced ensemble variational data assimilation for scalar-source identification in turbulent environments. *Journal of Computational Physics* **398,** 108856 (2019).
12. Kujawinski, E. B. *et al.* Fate of dispersants associated with the Deepwater Horizon oil spill. *Environmental science & technology* **45,** 1298–1306 (2011).
13. Liu, X. & Zhai, Z. Inverse modeling methods for indoor airborne pollutant tracking: literature review and fundamentals. *Indoor air* **17,** 419–438 (2007).

14. Gorelick, S. M., Evans, B. & Remson, I. Identifying sources of groundwater pollution: an optimization approach. *Water Resour. Res* **19,** 779–790 (1983).

15. Alapati, S., Kabala, Z., *et al.* Recovering the release history of a groundwater contaminant using a non-linear least-squares method. *Hydrological processes* **14,** 1003–1016 (2000).

16. Mahar, P. S. & Datta, B. Optimal monitoring network and ground-water-pollution source identification. *Journal of water resources planning and management* **123,** 199–207 (1997).

17. Mahar, P. S. & Datta, B. Identification of pollution sources in transient groundwater systems. *Water Resources Management* **14,** 209–227 (2000).

18. Mahar, P. S. & Datta, B. Optimal identification of ground-water pollution sources and parameter estimation. *Journal of Water Resources Planning and Management* **127,** 20–29 (2001).

19. Skaggs, T. H. & Kabala, Z. J. Recovering the History of a Groundwater Contaminant Plume: Method of Quasi-Reversibility. *Water Resources Research* **31,** 2669–2673 (1995).

20. Atmadja, J. & Bagtzoglou, A. C. Pollution source identification in heterogeneous porous media. *Water Resources Research* **37,** 2113–2125 (2001).

21. Woodbury, A. D. & Ulrych, T. J. Minimum relative entropy: Forward probabilistic modeling. *Water Resources Research* **29,** 2847–2860 (1993).

22. Woodbury, A., Render, F. & Ulrych, T. Practical probabilistic ground-water modeling. *Ground Water* **33,** 532 (1995).

23. Woodbury, A. D. A probabilistic fracture transport model: Application to contaminant transport in a fractured clay deposit. *Canadian geotechnical journal* **34,** 784–798 (1997).

24. Huang, C.-H., Li, J.-X. & Kim, S. An inverse problem in estimating the strength of contaminant source for groundwater systems. *Applied mathematical modelling* **32,** 417–431 (2008).

25. Mokhasi, P. & Rempfer, D. Optimized sensor placement for urban flow measurement. *Physics of fluids* **16,** 1758–1764 (2004).

26. Yildirim, B., Chryssostomidis, C. & Karniadakis, G. Efficient sensor placement for ocean measurements using low-dimensional concepts. *Ocean Modelling* **27,** 160–173 (2009).

27. Cohen, K., Siegel, S., Wetlesen, D., Cameron, J. & Sick, A. Effective sensor placements for the estimation of proper orthogonal decomposition mode coefficients in von Kármán vortex street. *Modal Analysis* **10,** 1857–1880 (2004).

28. Akhtar, I., Borggaard, J., Burns, J. A., Imtiaz, H. & Zietsman, L. Using functional gains for effective sensor location in flow control: a reduced-order modelling approach. *Journal of Fluid Mechanics* **781,** 622–656 (2015).

29. Mons, V., Chassaing, J.-C. & Sagaut, P. Optimal sensor placement for variational data assimilation of unsteady flows past a rotationally oscillating cylinder. *Journal of Fluid Mechanics* **823,** 230–277 (2017).

30. Kang, W. & Xu, L. Optimal placement of mobile sensors for data assimilations. *Tellus A: Dynamic Meteorology and Oceanography* **64,** 17133 (2012).

31. Najm, H. N. Uncertainty quantification and polynomial chaos techniques in computational fluid dynamics. *Annual review of fluid mechanics* **41,** 35–52 (2009).

32. Kalman, R. E. A new approach to linear filtering and prediction problems (1960).

33. Li, W. *et al.* A survey on multisensor fusion and consensus filtering for sensor networks. *Discrete Dynamics in Nature and Society* **2015** (2015).

34. Skaggs, T. H. & Kabala, Z. J. Recovering the release history of a groundwater contaminant. *Water Resources Research* **30,** 71–79 (1994).

35. Vergassola, M., Villermaux, E. & Shraiman, B. I. 'Infotaxis' as a strategy for searching without gradients. *Nature* **445,** 406–409 (2007).

36. Masson, J., Bechet, M. B. & Vergassola, M. Chasing information to search in random environments. *Journal of Physics A: Mathematical and Theoretical* **42,** 434009 (2009).

37. Hajieghrary, H., Tom, A. F., Hsieh, M. A., *et al. An information theoretic source seeking strategy for plume tracking in 3D turbulent fields* in *2015 IEEE International Symposium on Safety, Security, and Rescue Robotics (SSRR)* (2015), 1–8.

38. Brereton, C. A., Joynes, I. M., Campbell, L. J. & Johnson, M. R. Fugitive emission source characterization using a gradient-based optimization scheme and scalar transport adjoint. *Atmospheric Environment* **181,** 106–116 (2018).

39. Bieringer, P. E. *et al.* Automated source term and wind parameter estimation for atmospheric transport and dispersion applications. *Atmospheric Environment* **122,** 206–219 (2015).

40. Joynes, I. M. *Proof-of-concept inverse micro-scale dispersion modelling for fugitive emissions quantification in industrial facilities* PhD thesis (Carleton University, 2014).

41. Houweling, S., Kaminski, T., Dentener, F., Lelieveld, J. & Heimann, M. Inverse modeling of methane sources and sinks using the adjoint of a global transport model. *Journal of Geophysical Research: Atmospheres* **104,** 26137–26160 (1999).

42. Neupauer, R. M. & Wilson, J. L. Adjoint-derived location and travel time probabilities for a multidimensional groundwater system. *Water Resources Research* **37,** 1657–1668 (2001).

43. Pudykiewicz, J. A. Application of adjoint tracer transport equations for evaluating source parameters. *Atmospheric environment* **32,** 3039–3050 (1998).

44. Rosenfeld, M., Kawak, D. & Vinokur, M. A fractional step solution method for the unsteady incompressible Navier-Stokes equations in generalized curvilinear coordinate systems. *Journal of Computational Physics* **94,** 102–137 (1991).

45. Zaki, T. A. From streaks to spots and on to turbulence: exploring the dynamics of boundary layer transition. *Flow, turbulence and combustion* **91,** 451–473 (2013).

46. Nolan, K. P. & Zaki, T. A. Conditional sampling of transitional boundary layers in pressure gradients. *Journal of Fluid Mechanics* **728,** 306–339 (2013).

47. Lee, J., Jelly, T. & Zaki, T. A. Effect of Reynolds number on turbulent drag reduction by superhydrophobic surface textures. *Flow, Turbulence and Combustion* **95,** 277–300 (2015).

48. Lee, J., Sung, H. J. & Zaki, T. A. Signature of large-scale motions on turbulent/non-turbulent interface in boundary layers. *Journal of Fluid Mechanics* **819,** 165–187 (2017).

49. Kim, J., Moin, P. & Moser, R. Turbulence statistics in fully developed channel flow at low Reynolds number. *Journal of fluid mechanics* **177,** 133–166 (1987).

50. Jelly, T., Jung, S. & Zaki, T. Turbulence and skin friction modification in channel flow with streamwise-aligned superhydrophobic surface texture. *Physics of Fluids (1994-present)* **26,** 095102 (2014).

51. Colaço, M. J., Orlande, H. R. & Dulikravich, G. S. Inverse and optimization problems in heat transfer. *Journal of the Brazilian Society of Mechanical Sciences and Engineering* **28,** 1–24 (2006).

52. Zaki, T. A. & Saha, S. On shear sheltering and the structure of vortical modes in single- and two-fluid boundary layers. *Journal of Fluid Mechanics* **626,** 111–147 (2009).

53. Hasegawa, Y. & Kasagi, N. Low-pass filtering effects of viscous sublayer on high Schmidt number mass transfer close to a solid wall. *International Journal of Heat and Fluid Flow* **30,** 525–533 (2009).

54. Abe, H., Antonia, R. A. & Kawamura, H. Correlation between small-scale velocity and scalar fluctuations in a turbulent channel flow. *Journal of Fluid Mechanics* **627,** 1–32 (2009).

55. Quadrio, M. & Luchini, P. Integral space–time scales in turbulent wall flows. *Physics of fluids* **15,** 2219–2227 (2003).

56. Wang, Z.-s. *et al.* Potential source analysis for PM10 and PM2. 5 in autumn in a northern city in China. *Aerosol and Air Quality Research* **12,** 39–48 (2016).

57. Adler, J. Chemotaxis in bacteria. *Annual review of biochemistry* **44,** 341–356 (1975).

58. Kim, J. & Moin, P. in *Turbulent Shear Flows 6* 85–96 (Springer, 1989).

59. Burns, J. A. & King, B. B. *Optimal sensor location for robust control of distributed parameter systems* in *Decision and Control, 1994., Proceedings of the 33rd IEEE Conference on* **4** (1994), 3967–3972.

60. Balzano, L., Nowak, R. & Recht, B. *Online identification and tracking of subspaces from highly incomplete information* in *Communication, Control, and Computing (Allerton), 2010 48th Annual Allerton Conference on* (2010), 704–711.

61. Yang, B. Projection approximation subspace tracking. *IEEE Transactions on Signal processing* **43,** 95–107 (1995).

62. Strobach, P. Bi-iteration SVD subspace tracking algorithms. *IEEE Transactions on signal processing* **45,** 1222–1240 (1997).

63. Attallah, S. & Abed-Meraim, K. Fast algorithms for subspace tracking. *IEEE Signal Processing Letters* **8,** 203–206 (2001).

64. Badeau, R., David, B. & Richard, G. Fast approximated power iteration subspace tracking. *IEEE Transactions on Signal Processing* **53,** 2931–2941 (2005).

65. Comon, P. & Golub, G. H. Tracking a few extreme singular values and vectors in signal processing. *Proceedings of the IEEE* **78,** 1327–1343 (1990).

66. Hua, Y., Xiang, Y., Chen, T., Abed-Meraim, K. & Miao, Y. A new look at the power method for fast subspace tracking. *Digital Signal Processing* **9,** 297–314 (1999).

67. Sorensen, D. C. Implicitly restarted Arnoldi/Lanczos methods for large scale eigenvalue calculations, 119–165 (1997).

68. Van der Vorst, H. Subspace iteration for eigenproblems. *CWI Quarterly* **9,** 151–160 (1996).

69. Bewley, T. R., Moin, P. & Temam, R. DNS-based predictive control of turbulence: an optimal benchmark for feedback algorithms. *Journal of Fluid Mechanics* **447,** 179–225 (2001).

70. Bewley, T. R. & Protas, B. Skin friction and pressure: the "footprints" of turbulence. *Physica D: Nonlinear Phenomena* **196,** 28–44 (2004).

71. Kato, H., Yoshizawa, A., Ueno, G. & Obayashi, S. A data assimilation methodology for reconstructing turbulent flows around aircraft. *Journal of Computational Physics* **283,** 559–581 (2015).

72. Singh, A. P., Medida, S. & Duraisamy, K. Machine-learning-augmented predictive modeling of turbulent separated flows over airfoils. *AIAA Journal,* 2215–2227 (2017).

73. Skiba, Y. N. On a method of detecting the industrial plants which violate prescribed emission rates. *Ecological Modelling* **159,** 125–132 (2003).

Qi Wang

323 Latrobe Hall, 3400 N. Charles Street – Baltimore MD, 21218-2681
+1(305)394-1722 • qwang58@jhu.edu
pages.jh.edu/∼qwang58

Summary

My research exploits state-of-the-art mathematical and computational methods to address important aerodynamic challenges. High-performance simulation techniques are developed and adopted to predict and optimize complex aerodynamic flows, and to optimally place sensors and optimize the interpretation of their measurements. My past research helped to answer this question by exploiting the discrete adjoint operator in two different scenarios: passive scalar source reconstruction and localization from noisy sensor measurement and initial flow state reconstruction from wall friction measurements.

Education

Johns Hopkins University — **Baltimore, MD, United States**
PhD Candidate in Mechanical Engineering — *2014–2020*
Specializing in fluid mechanics

Beijing University — **Beijing, China**
Bachelor of Science in Theoretical & Applied Mechanics — *2010– 2014*
Minor degree in Mathematics

Honors and Awards

JHU Mech Eng Graduate Research Fellowship — **Johns Hopkins University**
AUG. 2014 – AUG. 2015

CUHK Research Internship Scholarship — **Chinese University of Hong Kong**
Financial Stipend awarded — *JUN. 2013 – AUG. 2013*

President — **Peking University, China**
Peking University Piano Association — *SEPT. 2012 – SEPT. 2013*

Third prize — **Peking University, China**
China Undergraduate Mathematical Contest in Modeling — *MAY. 2011*

Silver Medal — **Chong Qin, China**
The 25^{th} China Mathematics Olympiad — *APRIL. 2010*

Bronze Medal — **Hai Nan, China**
The 24^{th} China Mathematics Olympiad — *APRIL. 2009*

Gold Medal — **Washington, Seattle, USA**
Seattle International Piano Competition — *OCT. 2019*

Research Experience

Data assimilation and state estimation in turbulent flows — **Advisor: Tamer Zaki**
Fundamental limitations in initial-state estimation in wall turbulence — *2018 – 2020*

- Interpreted the Hessian matrix of the cost function mathematically as the ensemble average of cross-correlation of the adjoint fields.
- Developed code to compute the leading eigenvalues and eigenvectors of the Hessian matrix.
- Evaluated the sensitivity of wall measurements according to the leading eigenvectors of the Hessian matrix.

Olfactory search algorithms in turbulent environments **Advisor: Tamer Zaki**
Research Assistant, Johns Hopkins University *2015 – 2019*

- Investigated the behavior of forward and adjoint scalar field in turbulent environments.
- Developed codes with massively parallel adjoint optimization to identify source location and profile generating a scalar field in turbulent channel flow.
- Devised innovative algorithm that tracks leading subspace of source-response system and minimizes condition number to find optimal sensor placements.
- Performed uncertainty quantification of scalar source localization when measurements are subject to noise.

Wake-induced cross-flow instability on a swept airfoil **Advisor: Tamer Zaki**
Research Assistant, Johns Hopkins University *2014 – 2017*

- Designed simplified physical model using cylinder placed in front of airfoil to simulate leading-edge slat of modern airplanes.
- Constructed body-fitted mesh for leading edge and applied Immersed Boundary Method (IBM) for cylinder.
- Determined the physical mechanism of boundary layer transition by comparing with Linear Stability Theory (LST).

Numerical Study of Transonic Flow around a Supercritical Airfoil **Advisor: Zuoli Xiao**
Degree Thesis, Beijing University *APRIL. 2013 – JULY. 2014*

- Enhanced parallel-FORTRAN code for compressible flow with Smagorinsky, S-A and SST turbulence models to simulate high Reynolds and high Mach number flow around supercritical airfoil.
- Obtain body-fitted orthogonal mesh by solving elliptic equation.
- Conducted numerical simulations using DNS, RNS and LES to study shock-wave oscillation on the airfoil.
- Tested newly developed Constrained-LES in shock-wave oscillation scenario.

Numerical Simulation of Boat maneuvering **Instructor: Yunhui Liu**
Research internship, Automation Department, CUHK *JUNE. 2013 – AUG. 2013*

- Designed VOF model to simulate a boat on water surface.
- Obtained body-fitted 3D unstructured mesh using autoCAD and Gambit.
- Performed numerical simulations with Ansys Fluent to determined parameters in Fossen's boat dynamic model. Determined parameters agreed with experiments and were important references for future studies.

Teaching Experience

Teaching Assistant, Johns Hopkins University **Professor: Tamer Zaki**
Hydrodynamic Stability, Graduate class, evaluation score 4.72/5.00 *JAN. 2017 – MAY. 2017*

- Delivered lectures on spectral methods to computationally prepare students for stability analysis.
- Composed homework questions and created sample solutions.
- Graded the homework with comments and suggestions for students.
- Designed midterm exams and composed solutions.

Teaching Assistant, Johns Hopkins University **Professor: Tamer Zaki**
Numerical Methods, Graduate class, evaluation score 4.63/5.00 *SEPT. 2015 – JAN. 2016*

- Delivered complementary lectures based on problems in homework. Conducted weekly TA sections for grad students.
- Composed homework questions and created sample solutions.
- Graded the homework with comments and suggestions for students.
- Designed midterm exams and composed solutions.

Publications

- **Qi Wang**, Yosuke Hasegawa, and Tamer A. Zaki. "Spatial reconstruction of steady scalar sources from remote measurements in turbulent flow." Journal of Fluid Mechanics 870 (2019): 316-352.
  - Derived and implemented the discrete adjoint for three dimensional advection-diffusion equation for scalar transport.
  - Performed spatial source localization using forward-adjoint loops and evaluated quality of reconstruction for different source-sensor arrangements.
  - Quantified the effect of turbulent dispersion and molecular diffusion on adjoint algorithms to perform source reconstruction.
- Vincent Mons, **Qi Wang**, and Tamer A. Zaki. "Kriging-enhanced ensemble variational data assimilation for scalar-source identification in turbulent environments." Journal of Computational Physics 398 (2019): 108856.
  - Developed code to construct source-response system from ensemble of trial sources.
  - Determined the optimal sensor placement using condition number minimization framework.
- Mengze Wang, **Qi Wang**, and Tamer A. Zaki. "Discrete adjoint of fractional-step incompressible Navier-Stokes solver in curvilinear coordinates and application to data assimilation." Journal of Computational Physics 396 (2019): 427-450.
  - Derived and implemented conjugate-gradient based orthogonal projector to project adjoint fields onto solenoidal space while satisfying the Lagrangian identity to machine precision.
- **Qi Wang**, Vincent Mons, and Tamer A. Zaki. "Optimal sensor placement for spatial reconstruction of scalar sources in a turbulent channel flow." in review.
  - Derived the mathematical framework of condition number minimization and applied to optimal sensor placement problem.
  - Created algorithm to track the leading subspace of source-response system and iteratively optimize the sensors.
  - Demonstrated improvement of source identification using optimal sensors.
- **Qi Wang**, Mengze Wang, and Tamer A. Zaki. "Difficulty of state estimation from wall measurements in channel flow." In review.
  - Interpreted the Hessian matrix of the cost function mathematically as the ensemble average of cross-correlation of the adjoint fields.
  - Developed code to compute the leading eigenvalues and eigenvectors of the Hessian matrix.
  - Evaluated the sensitivity of wall measurements according to the leading eigenvectors of the Hessian matrix.
- **Qi Wang**, and Tamer A. Zaki. "An eigen-ensemble-variational algorithm for characterization of scalar sources in turbulent environment." In preparation.
  - Derived a framework to use spatially distributed trial sources to estimate eigen-sources of source-response system.
  - Optimized the source parameters by projecting the measurement onto eigen-measurements.
  - Quantified uncertainty in source prediction when measurements are noisy. Related uncertainty to scalar field properties.

Presentations

- Wang, Qi, and Tamer Zaki. "An eigen-ensemble-variational algorithm for identifying scalar sources from remote measurements in turbulent environments." Bulletin of the American Physical Society (2019).
- Wang, Qi, and Tamer Zaki. "Fundamental limitations in initial-state estimation using surface measurements in wall turbulence." Bulletin of the American Physical Society (2018).
- Mons, Vincent, Qi Wang, and Tamer Zaki. "Ensemble-based data assimilation and optimal sensor placement for scalar source reconstruction." APS Meeting Abstracts. 2017.
- Wang, Qi, et al. "Adjoint-optimization algorithm for spatial reconstruction of a scalar source." APS Division of Fluid Dynamics Meeting Abstracts. 2016.
- Wang, Qi, Mengze Wang, and Tamer A. Zaki. "Difficulty of State Estimation from Wall Measurements in Turbulent Channel Flow" November 2018, Graduate Seminar in the Department of Mechanical Engineering, Johns Hopkins University.
- Wang, Qi, and Tamer A. Zaki. "Direct Numerical Simulations of Wake-Induce Transition in Three-Dimensional Boundary Layer" December 2016, Graduate Seminar in the Department of Mechanical Engineering, Johns Hopkins University.
- Wang, Qi, Vincent Mons, and Tamer A. Zaki. "Data-Assimilation for Scalar-Source Reconstruction" April 2017, Graduate Seminar in the Department of Mechanical Engineering, Johns Hopkins University.
- Wang, Qi, Vincent Mons, and Tamer A. Zaki. "An Adjoint-Based Algorithm for Detection of Scalar Release" October 2015, Graduate Seminar in the Department of Mechanical Engineering, Johns Hopkins University.

International collaborations

Hasegawa Yosuke, Department of Mechanical and Biofunctional Systems, Tokyo University.

Professional Affiliations

member, American Physics Society

Grant Applications

- Enhanced-Fidelity Simulations and Interpretation of Measurements in Turbulent Flows.
- Data assimilation and state estimation in transitional and turbulent flows: Optimal sensing parameters & bounds on prediction accuracy